

## Dissertation

# FINITE-ELEMENTE-SIMULATION PIEZOELEKTRISCHER AKUSTISCHER OBERFLÄCHENWELLEN-SENSOREN

ausgeführt zum Zwecke der Erlangung des akademischen Grades  
eines Doktors der technischen Wissenschaften unter der Leitung von

Univ.Prof. Dipl.-Ing. Dr.techn. Manfred Kaltenbacher  
Institut für Mechanik und Mechatronik  
Abteilung für Messtechnik und Aktorik, E325/A4

eingereicht an der Technischen Universität Wien  
**Fakultät für Maschinenwesen und Betriebswissenschaften**

von

**Dipl.-Ing. Kirill Shaposhnikov**

Mat.Nr. 1426502

Waldgasse 17/11

1100 Wien

Wien, Dezember 2015

---



## Kurzfassung

Piezoelektrische akustische Oberflächenwellen-Sensoren (SAW-Sensoren) werden ausgiebig in der Industrie und im Alltag verwendet. Aufgrund ihrer Passivität, Zuverlässigkeit, Robustheit und Fernabfragbarkeit sind solche Sensoren für Telekommunikation, Bio- und Medizintechnologien, chemische Industrie, usw. attraktiv. Das Grundprinzip eines piezoelektrischen SAW-Sensors basiert auf der bidirektionalen Umwandlung von elektrischer und mechanischer Energie. Zuerst wird das elektrische Signal eines Sender-Interdigitalwandlers in eine mechanische Oberflächenwelle transformiert. Die Welle breitet sich auf der Oberfläche des Sensors aus und wird danach wieder in ein elektrisches Signal an einem Empfänger umgewandelt. Die SAW-Sensoren arbeiten im Hochfrequenzbereich und bestehen aus Hunderten von Elektroden. Damit ist hier erkennbar, dass die Verwendung mathematischer Modellierung zu Simulation und Design von SAW-Sensoren notwendig ist. Diese Dissertation konzentriert sich auf die Entwicklung eines mathematischen und numerischen Finite-Elemente-Modells für piezoelektrische SAW-Sensoren. Die gewünschten Parameter, die weiter zu Design und Optimierung des Sensors benutzt werden können, kann man mit Hilfe des entwickelten Modells bestimmen. Diese berücksichtigt auch die Auswirkungen der Temperatur und der Vorspannung auf die Ausbreitung der Wellen.

Das Modell, das in dieser Dissertation entwickelt wird, setzt voraus, dass die Struktur des Sensors periodisch ist. Die Voraussetzung wird in der Mehrheit mathematischer Modelle piezoelektrischer SAW-Sensoren verwendet und macht es möglich, eine Einzelzelle mit periodischen Randbedingungen statt der ganzen Struktur zu simulieren. Um effizient die in das Substrat ausbreitenden Wellen ohne Beschneidungseffekte zu modellieren, wurde ein spezielles Perfectly-Matched-Layer Verfahren entwickelt. Die Algorithmen des numerischen Modells werden innerhalb der Finite-Elemente-Software CFS++ implementiert. Die Genauigkeit der Simulationsergebnisse wird durch den Vergleich mit Literaturdaten sowie Messergebnissen bestätigt. Zusätzlich erfolgt eine detaillierte Darstellung, wie man die Parameter von SAW-Sensoren durch die Simulationsergebnisse gewinnen kann, und auch wie die Temperatur- und mechanische Vorspannungseffekte die Ausbreitung der Wellen beeinflussen.

Diese Arbeit ist in Kooperation mit dem Kompetenzzentrum CTR Carinthian Tech Research AG (Villach, Österreich) durchgeführt worden. CTR wird im Rahmen von COMET – Competence Centers for Excellence Technologies durch das Bundesministerium für Verkehr, Innovation und Technologie (BMVIT), Bundesministerium für Wirtschaft und Arbeit (BMWA), Land Kärnten und Land Steiermark gefördert. Das Programm COMET wird durch die Österreichische Forschungsförderungsgesellschaft (FFG) abgewickelt.



## **Ehrenwörtliche Erklärung**

Ich erkläre ehrenwörtlich, dass ich die vorliegende wissenschaftliche Arbeit selbstständig angefertigt und die mit ihr unmittelbar verbundenen Tätigkeiten selbst erbracht habe. Ich erkläre weiters, dass ich keine anderen als die angegebenen Hilfsmittel benutzt habe. Alle aus gedruckten, ungedruckten oder dem Internet im Wortlaut oder im wesentlichen Inhalt übernommenen Formulierungen und Konzepte sind gemäß den Regeln für wissenschaftliche Arbeiten zitiert und durch Fußnoten bzw. durch andere genaue Quellenangaben gekennzeichnet.

Die während des Arbeitsvorganges gewährte Unterstützung einschließlich signifikanter Betreuungshinweise ist vollständig angegeben. Die wissenschaftliche Arbeit ist noch keiner anderen Prüfungsbehörde vorgelegt worden. Diese Arbeit wurde in gedruckter und elektronischer Form abgegeben. Ich bestätige, dass der Inhalt der digitalen Version vollständig mit dem der gedruckten Version übereinstimmt.

Ich bin mir bewusst, dass eine falsche Erklärung rechtliche Folgen haben wird.

---

**(Unterschrift)**

---

**(Ort, Datum)**



**Dissertation**

# **Finite Element Simulation of Piezoelectric Surface Acoustic Wave Sensors**

performed for the purpose of obtaining the academic degree  
of Doctor of Technical Science  
under the supervision of

Univ.Prof. Dipl.-Ing. Dr.techn. Manfred Kaltenbacher  
Institute of Mechanics and Mechatronics  
Measurement and Actuator, E325/A4

submitted to the Vienna University of Technology  
**Faculty of Mechanical and Industrial Engineering**

by

**Dipl.-Ing. Kirill Shaposhnikov**

Mat.Nr. 1426502

Waldgasse 17/11

1100 Wien

Vienna, December 2015

---



## Abstract

Surface acoustic wave devices have become in use for many industrial and civil applications. Features such as passiveness, robustness, reliability, and remote-control make them attractive for telecommunications, biotechnologies, chemical industry, etc. The operating principle of piezoelectric surface acoustic wave (SAW) devices lies in the transformation of an electric input signal into an acoustic wave that propagates over the piezoelectric substrate. The surface wave is then transformed back to an electric output signal. As a rule, SAW devices operate at radio frequencies and have a tiny size. The acoustic wave is generated by an grating, which can contain up to some hundreds of electrodes. The complexity of SAW devices implies therefore their precise modelling in order to meet design and operating requirements. In this thesis we suggest a mathematical model for a SAW interdigital transducer based on finite element method. The model is intended to be used for computation of the parameters of SAW devices for further design and optimisation. We also concentrate on the influence of such effects as temperature and mechanical prestressing on the propagation of SAW.

Here, as in the majority of models for SAW devices, we deal with the structures that have a periodic pattern and thereby turn to the model for a unit cell with periodic boundary conditions. In order to reduce computational costs, we utilise the perfectly matched layer technique. This numerical scheme is implemented within the finite element software CFS++ and validated through the comparison of the results with those obtained from other numerical approaches and reported in literature as well as measured data. We also discuss how the developed model can be used for calculation of SAW device parameters and estimation of temperature and prestressing effects on the propagation of SAW.

This work has been done in cooperation with the competence centre CTR Carinthian Tech Research AG (Villach, Austria). CTR is funded within the R&D Program COMET – Competence Centers for Excellent Technologies by the Federal Ministries of Transport, Innovation and Technology (BMVIT), of Economics and Labour (BMWA) and it is managed on their behalf by the Austrian Research Promotion Agency (FFG). The Austrian provinces (Carinthia and Styria) provide additional funding.

---

## Acknowledgement

In the first place, I wish to express my gratitude to my supervisor Prof. Dipl.-Ing. Dr. techn. Manfred Kaltenbacher, who has supported me since the very beginning of my work. He always believed in success of this research, even when it seemed to me that I had hit a dead-end. We spent a lot of time discussing physics, mathematics, and numerics to reach the goals of this Ph.D.. His ability to create a comfortable and cosy atmosphere within the working group made everyone feel free but, at the same time, confident and sustained in his work.

Second, I would like to thank Prof. Dipl.-Ing. Dr. techn. Franz Rammerstorfer for his interest to my work and the acceptance of the invitation to be a reviewer. Being an outstanding teacher, he has imparted a great deal of knowledge of solid mechanics to me. Third, I appreciate the support from Dr. Pascal Nicolay – my industrial supervisor at CTR AG – who has introduced me to the topic of piezoelectric SAW devices. His fine ideas and remarks often helped me to look at the things from a different angle and, in the end, hit the mark. He was always available for questions and discussions.

I would also like to thank all my colleagues at the research group of Measurements and Actuators of TU Wien for this pleasant time we have spent together – not only at work but also in everyday life. I could never wish a better team to work with. I want especially mention Dr. techn. Andreas Hüppe who has led me through the jungle of programming for CFS++.

I wish to express a special gratitude to my wife Anastasia, who every day beheld my pursuit towards Ph.D., and to my parents Olga and Sergey, who could only see me distantly, for their support, encouragement, and belief in me.

---

## Table of Contents

---

<b>Introduction</b>	<b>1</b>
<b>1 Phenomenological models of SAW devices</b>	<b>8</b>
1.1 Coupling of modes model . . . . .	8
1.2 P-matrix model . . . . .	13
1.3 Parameters extraction techniques. Harmonic admittance . . . . .	15
<b>2 Mathematical description of wave propagation in piezoelectric media</b>	<b>19</b>
2.1 Principles of linear elasticity and electrostatics . . . . .	19
2.2 Elastic waves in solids. Slowness curves . . . . .	24
2.3 Surface waves in piezoelectric half-space . . . . .	27
2.4 Second order effects on wave propagation in piezoelectric media . . . . .	29
<b>3 Numerical model of wave propagation and FE-formulation</b>	<b>36</b>
3.1 Finite element model of piezoelectric substrate with periodic electrode grating . . . . .	36
3.2 Boundary element method and absorbing boundary conditions . . . . .	42
3.3 Perfectly matched layer technique . . . . .	51
3.4 Periodic boundary conditions handling . . . . .	61
<b>4 Numerical aspects and model validation</b>	<b>68</b>
4.1 Periodic boundary conditions and perfectly matched layer . . . . .	68
4.2 Surface acoustic waves in piezoelectric substrates under periodic electrode gratings . . . . .	76
<b>5 Applications</b>	<b>83</b>
5.1 Dispersion curves and stop-band analysis . . . . .	83

5.2	Determination of temperature coefficient of frequency . . . . .	86
5.3	Lithium niobate crystal on steel blade subjected to longitudinal strain . .	87
	<b>Conclusion</b>	<b>91</b>
	<b>Appendix</b>	<b>93</b>
	<b>Bibliography</b>	<b>95</b>



Piezoelectric surface acoustic wave (SAW) devices find their application in various fields such as microelectromechanical systems (MEMS), telecommunications, non-destructive testing, biotechnology, chemical sensing, etc. [1–3]. They are highly appreciated because of their passiveness, robustness, reliability, and ability to operate in harsh environments. The operation principle of such devices lies in the transformation of an electric input signal into a mechanical SAW. The last in its turn is further converted back into an electric signal. The key feature is a high sensitivity of the mechanical wave to the surface state, which is in contrast to the electric signal. The surface state can be conditioned by such physical phenomena as temperature, humidity, pressure, etc., which affect the velocity of SAW. The velocity change can be measured as the change in amplitude, phase, frequency, or time-delay between the input and output electrical signals.

The existence of SAW was first discovered by Lord Rayleigh who studied the behaviour of waves on the plane free surface of an isotropic homogeneous elastic half-space. The wave solution described in his work [4] was then named after him. It was further confirmed that Rayleigh waves are present in earthquake shocks. Rayleigh waves have been used for non-destructive testing owing their ability to reflect from defects in the material [1], however, their usage in electronic devices had been imperceptible until the invention of the interdigital transducer (IDT) by White and Voltmer [2] in 1965. The IDT exploits the inverse piezoelectric effect to convert an input signal into an acoustic wave. An IDT contains two interlocking comb-shaped arrays of metallic electrodes. Being located on the surface of a piezoelectric material and driven by a voltage, the polarity of adjacent fingers will be switching from “+−” to “−+” and back, which will affect the direction of the electric field between the fingers. The electric field will in turn create compressible and tensile strains within the material, which will generate a mechanical wave. Travelling over the surface, the wave will reach a receiving IDT, where it will be transformed into an electric signal owing to the direct piezoelectric effect. Such a setup is schematically shown in fig. I.1. An IDT operates ensuring constructive interference

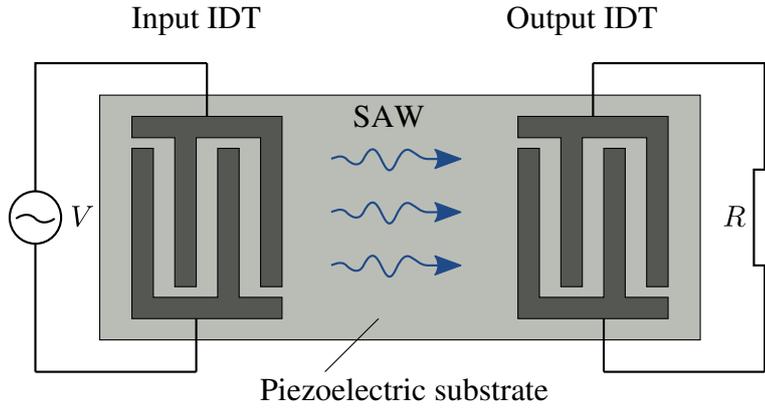


Figure I.1: Schematic picture of SAW transducer

between all finger pairs, which means that they generate the same level of compression or tension. This is achieved by having the same distance between the fingers that is known as the pitch  $p$ . Should the transducer have a grating with alternate polarity of the electrodes (single electrode IDT), the wavelength of the mechanical wave will be  $\lambda_0 = 2p$  [1]. The center frequency of the device then equals  $f_0 = v/\lambda_0$ , where  $v$  is the phase velocity. Ideally, the input electric signal should be at the synchronous frequency to minimize insertion loss.

The phenomenon of piezoelectricity exploited among others in SAW devices was discovered by brothers Curie in 1880. They found that pressure and tension applied to some crystalline minerals results in change of polarisation proportional to the mechanical load [5]. The piezoelectric effect is reversible, which was confirmed by the brothers in 1881, i.e. an external electric field causes a mechanical deformation of the crystal. Piezoelectric materials have first come to use in submarine sonar systems being a part of the transducer that generated acoustic waves in the sea: the material used there was quartz. It is important to mention that not every crystal exhibits piezoelectric properties. It was Voigt who described in his work [6] 20 classes of natural crystals capable to piezoelectricity and suggested a tensor form to piezoelectric constants. The presence or the absence of the piezoelectric properties are explained by the structure of the crystal lattice. For example, a sodium chloride (NaCl) crystal has an octahedral structure, and its unit cell can be schematically shown as a rectangle (see fig. I.2, (a)). The cell is obviously not polarized as the ions  $\text{Na}^+$  and  $\text{Cl}^-$  compensate each other. The compensation also remains if an external load is applied (see fig. I.2, (b)). The situation is different for quartz ( $\text{SiO}_2$ ). Its crystals have trigonal structure, and the unit cell has a hexagonal form. Being free the cell has no dipole moment (see fig. I.3, (a)). However, it becomes polarised under external mechanical loads (see fig. I.3, (b)). Another significant feature was discovered for  $\text{BaTiO}_3$  in 1945. It was capable of changing the form of its crystal lattice from cubic to perovskite (tetragonal) as the temperature goes down below Curie point. The position of  $\text{Ba}^{2+}$  ion in perovskite structure becomes shifted from the center

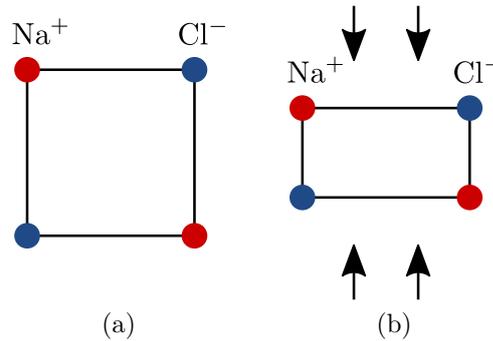


Figure I.2: NaCl unit cell without (a) and with (b) external mechanical load

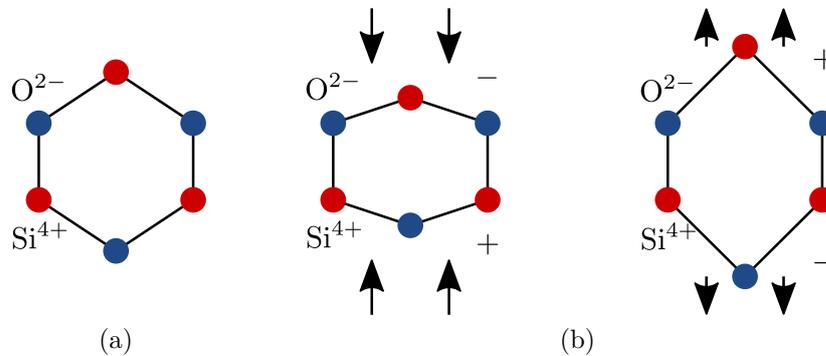


Figure I.3: SiO<sub>2</sub> unit cell without (a) and with (b) external mechanical load

of the cell so that a non-zero (spontaneous) polarisation occurs. The arrangement of cells in the same way (poling) delivers the piezoelectric constants many times higher than those of the natural crystals [5]. This gave impetus to the wide use of piezoelectric materials in industrial applications.

Different piezoelectric materials are used as substrates in SAW devices depending on the area of their applications. The materials differ in the velocity of SAW that can be excited on the substrate surface, electromechanical coupling coefficient, sensitivity to physical phenomena the device is designed to measure, etc. The device itself can be a complex structure that contains such parts as IDTs, reflectors (shot- or open-circuited metal strips), and delay lines of various forms. These propose the use of mathematical modelling for design and optimisation of SAW devices.

The mathematical models for SAW devices can be conventionally divided into two principal groups. The first group includes 1D models for SAW correlators that utilise approaches with lumped parameters. These models have come in use since the introduction of SAW devices in 1960s. They are not able to provide us with the field results at every point of interest, but can give a description of the device behaviour. For this reason these models have found their use in the design of SAW devices. The simplest

and one of the earliest approaches was the delta-function impulse/response model proposed by Tancrell and Holland [7]. The model requires that transducers be uniform, i.e. have the same pitch and width. Moreover, the transducers are assumed to be reflectionless. The model provides necessary information about the transducer response and is still in use nowadays. But its main limitation is that the device impedance is not obtainable [8]. This was overcome by the equivalent circuit model [9], where the transducer was modelled as an array of bulk wave transducers. The electric field was assumed to be either vertical or horizontal, which led to “cross-field” or “in-line” model respectively [8]. The “cross-field” model is more close to reality. It also allows to include reflections through the impedance discontinuities and covers all basic phenomena, such as capacitance, transduction, propagation, and reflection [8]. One of more recent models is coupling of modes (COM) model [10]. It suggests a 1D approach based on a system of ordinary differential equations. The model describes the interaction between forward- and backward propagating waves with slowly varying amplitudes without taking the penetration depth into account. The coupling between two modes is due to the presence of a weightless grating that causes reflections. This approach gives algebraic expressions for all the desired parameters (conversion, reflection, admittance). As input it requires such parameters as transduction, reflection, velocity and attenuation [8]. The P-matrix model [11] can be considered as an algebraic equivalent of the COM model. It is based on the principle of a three-port “black box” (similar to the equivalent circuit model) with two acoustic and one electric port. The model provides a coupling of incident wave amplitudes and voltage with reflected waves amplitudes and electric current through a  $3 \times 3$  matrix. The advantage of this approach is that a certain P-matrix can be found for every individual part of a SAW device. Their further concatenation provides a model for the whole device. We shall devote the next chapter to the details of the COM and the P-matrix models.

The approaches mentioned above give effective tools for design and optimisations of SAW devices. However, their use is possible only if the input parameters are known. They cannot be deduced from the models themselves and therefore need to be preliminary determined. One way is to obtain them experimentally analysing specially fabricated test structures, which is possible without considering the complexity of underlying physics [8]. This is however an extravagant approach, because the required parameters are functions of the geometry and the material data. Therefore, a test device must be fabricated for almost every measurement. On the other hand, one can gain these parameters through numerical simulations. This brings us to the second group of mathematical models for SAW devices. Stop-band analysis yields the velocity of SAW and the reflection coefficient. The transduction parameter of a transducer is available from the analysis of its short- and open-grating modes [8]. The models of this group are based on partial differential equations that describe electro-mechanical field coupling in SAW devices. They are thus field models, i.e. yield the solution in the form of a distribution of electrostatic and mechanical fields.

One of the first of such models was suggested by Milsom *et al.* in [12]. It combines

analytical and numerical techniques: the first is based on Green's function approach to a semi-infinite 2D piezoelectric half-space, and the second uses numerical integration methods to get the distribution of electric charge over the electrodes. The last assumes to be perfectly conductive and massless. Later, Hashimoto and Yamaguchi applied the discrete Green's function approach to the modelling of acoustic waves under periodic gratings [13]. The effect of electrode thickness was also neglected there. Hasegawa and Koshiha used the combination of finite element and analytical methods [14] to study reflective properties of gratings. Chen *et al.* investigated the effect of film thickness on the wave propagation in single-phase unidirectional transducers using the FEM and the COM model [15]. Since the influence of the electrode mass is an important factor, further models were developed to take this effect into account. They associated individual numerical or analytical techniques for different parts of the device. Regarding SAW transducers with periodic electrode gratings we refer to Reichinger [16], Ventura [17, 18], and Hashimoto [19]. The idea built into these models is to apply FEM for simulation of the electrode mechanical behaviour and the Green's function formalism to the piezoelectric substrate. The last leads to either boundary element method (BEM) in [17, 18] or spectral domain analysis (SDA) in [19]. These studies have stimulated further use of such a coupling by other researchers yielding tools able to deal with complex structures and different types of acoustic waves. The complexities include geometrical inhomogeneities such as layered patterns in electrode and substrate structures, covers, shape and position of electrodes. On the other hand, material inhomogeneities arise if external physical factors (temperature, humidity, pressure, etc.) are taken into account. Along with the approaches that used the coupling of FEM with other techniques, models built on "pure" FEM have become attractive to simulations of SAW devices. The strengths of such an approach are due to robustness, reliability, and simplicity of FEM. At the same time, FEM requires meshing of both the electrode and the substrate, which could lead to an enormous amount of computational efforts, at least in 1990s, when the models utilising "pure" FEM first came in use [20, 21]. To date, the problem of computational costs still remains important. For this reason both groups of numerical techniques exist and are used alongside with one another, being one more effective than the other for certain tasks and setups. For example, FEM/BEM coupling is far stronger than "pure" FEM for uniform substrates, while "pure" FEM keeps the same effectiveness regardless to the number of layers or other inhomogeneities. We should note that both ways do not provide models for a real device but simulate a simplified structure that approximately corresponds to the initial setup. Among others, the most significant simplifications in use are a periodic pattern of the electrode grating and a 2D spatial dependence of the acoustic waves generated in the piezoelectric substrate.

The goals of the current PhD thesis are as follow:

- development of a numerical model and a software tool for simulations of SAW in piezoelectric materials under periodic electrode gratings,
- investigation of SAW propagation in various crystals and extraction of design pa-

rameters,

- implementation of temperature and prestressing effects and investigation of their influence on the propagation of SAW.

The numerical model is based on finite element (FE) frequency domain approach for a unit cell of a periodic structure which contains piezoelectric substrate, metallic electrodes, and, perhaps, other extra structures that exhibit electric and/or mechanical properties. Bloch-periodic boundary conditions are incorporated into the model in order to take into account possible periodic patterns of the structure. In contrast to the conventional Lagrange multipliers approach to periodic boundary conditions, we implement here Nitsche's method that leads to a more stable and easier solvable numerical scheme. We apply special absorbing boundary conditions in the form of a perfectly matched layer (PML) and thereby significantly reduce computational domain and time. The PML is designed in a way which makes it possible to absorb both near-surface propagating waves and waves radiating down into the substrate. This is achieved by the use of a special shifted metric extensively utilised in geophysics for simulations of seismic waves. The effects of temperature and prestressing are implemented through the change of material data and, for prestressing, static analysis of preliminary deformations. This yields to a two-step approach to simulations of acoustic waves in prestressed media. The approach includes static analysis of mechanical stress caused by initial deformations with further use of the results in harmonic analysis of wave propagation. The association of FE and COM/P-matrix models is done through the harmonic admittance approach. The analysis of harmonic admittance curves obtained from finite element simulations provide desired parameters for COM/P-matrix models like SAW velocity, reflectivity, capacitance, etc. Having these parameters at hand, we can also study how they are influenced by the effects of temperature and prestressing.

The thesis is structured as follows

- In chapter 1, the derivation of COM and P-matrix models is briefly discussed. We provide the ideas of stop-band analysis and parameter extraction techniques. We also consider the harmonic admittance approach to simulation of an IDT.
- Chapter 2 is devoted to mathematical description of wave propagation in piezoelectric media. There, we derive the piezoelectric partial differential equations (PDE) and discuss the phenomena of bulk and surface waves in solids. We consider the influence of temperature and prestressing effects on wave propagation and take them into account within the mathematical model.
- Chapter 3 presents the numerical model for SAW in periodic structures based on FEM. The system of piezoelectric PDEs in its weak form is reduced to a linear system. We discuss the ways of computational domain truncation; namely, how it can be done using FEM/BEM or "pure" FEM with PML techniques. Two ways

of handling periodic boundary conditions – Lagrange multipliers and Nitsche’s approach – are discussed.

- In chapter 4, we touch upon the validation the developed model and talk about aspects of numerical computations. We also consider examples of SAW simulations in various piezoelectric substrates under periodic electrode gratings.
- Chapter 5 presents applications of the developed model. The questions of the stop-band determination and effects of temperature and preliminary prestressing on the propagation of SAW are discussed. We compare the simulation results with those obtained from literature and experiments.

# CHAPTER 1

---

## Phenomenological models of SAW devices

---

### 1.1 Coupling of modes model

The coupling-of-modes (COM) method has been extensively used for microwave and optical waveguides [22, 23] and has also found its application to the analysis of SAW devices [10, 24]. A thorough derivation of COM equations for SAW devices can be found for example in [1] or [25]. We present here a briefer description of the model as it is given in [26].

We consider two waves  $u_+(x)$  and  $u_-(x)$  propagating in  $x$ -direction to the right and to the left respectively. They satisfy the following equations

$$\begin{aligned}\frac{du_+}{dx}(x) &= -i\beta_u u_+(x), \\ \frac{du_-}{dx}(x) &= +i\beta_u u_-(x)\end{aligned}$$

with  $\beta_u$  denoting the wavenumber. The last is defined as  $\beta_u = \omega/v$ , where  $\omega = 2\pi f$  is the angular frequency and  $v$  is the wave velocity, and therefore depends on frequency. The presence of a grating leads to an interaction between the waves so that they start propagating with a reflection, i.e.

$$\begin{aligned}\frac{du_+}{dx}(x) &= -i\beta_u u_+(x) - i\tilde{\kappa}(x) u_-(x), \\ \frac{du_-}{dx}(x) &= +i\tilde{\kappa}'(x) u_+(x) + i\beta_u u_-(x).\end{aligned}$$

The conservation of power requires [27] that  $\frac{d}{dx} (|u_+(x)|^2 - |u_-(x)|^2) = 0$ . Therefore,

it follows that  $\tilde{\kappa}' = \bar{\tilde{\kappa}}$ .

If the grating is arranged in a periodic manner with a period  $p$ , we can expand the coupling parameter  $\tilde{\kappa}$  in a Fourier series

$$\tilde{\kappa}(x) = \sum_{n=-\infty}^{+\infty} \tilde{\kappa}_n e^{-in\beta_g x}$$

with  $\beta_g = 2\pi/p$ . According to [26], the  $M^{\text{th}}$ -order Bragg's condition [28] is satisfied when  $|\beta_u(f_0) - 2\pi M/p| = |\beta_u(f_0)|$ . The last condition leads to  $\beta_u(f_0) = -M\beta_g/2$ . We can now consider the coupling with a certain harmonic having the wavenumber  $-M\beta_g$ , which yields

$$\frac{du_+}{dx}(x) = -i\beta_u u_+(x) - i\kappa_{12} u_-(x) e^{-iM\beta_g x}, \quad (1.1)$$

$$\frac{du_-}{dx}(x) = +i\bar{\kappa}_{12} u_+(x) e^{iM\beta_g x} + i\beta_u u_-(x) \quad (1.2)$$

with  $\kappa_{12} = \tilde{\kappa}_{-M}$ .

Let  $u_+(x) = U_+(x) e^{-iM\beta_g x/2}$  and  $u_-(x) = U_-(x) e^{iM\beta_g x/2}$ . Substituting the last relations into (1.1), (1.2) we obtain

$$\begin{aligned} \frac{dU_+}{dx}(x) &= -i\theta_u U_+(x) - i\kappa_{12} U_-(x), \\ \frac{dU_-}{dx}(x) &= +i\bar{\kappa}_{12} U_+(x) + i\theta_u U_-(x). \end{aligned}$$

The parameter  $\theta_u(f) = \beta_u(f) - M\pi/p$  in (1.1), (1.2) is known as the detuning factor and means a deviation of the wavenumber from the Bragg's condition.

Let now a harmonic voltage  $V$  be applied to the grating such that the electric period of the grating equals  $p_I$ . We rewrite the system (1.1), (1.2) with the electric excitation taken into account as follows

$$\begin{aligned} \frac{du_+}{dx}(x) &= -i\beta_u u_+(x) - i\kappa_{12} u_-(x) e^{-iM\beta_g x} + i\zeta V e^{-iM\pi/p_I x}, \\ \frac{du_-}{dx}(x) &= +i\bar{\kappa}_{12} u_+(x) e^{iM\beta_g x} + i\beta_u u_-(x) - i\bar{\zeta} V e^{iM\pi/p_I x}. \end{aligned}$$

Setting  $p_I = 2p = \lambda$ , which corresponds to a single electrode IDT, and using the same substitution for  $u_{\pm}$  as above, we arrive at

$$\begin{aligned} \frac{dU_+}{dx}(x) &= -i\theta_u U_+(x) - i\kappa_{12} U_-(x) + i\zeta V, \\ \frac{dU_-}{dx}(x) &= +i\bar{\kappa}_{12} U_+(x) + i\theta_u U_-(x) - i\bar{\zeta} V. \end{aligned}$$

It can be shown [26] that the electric current  $I$  fulfils the following equation

$$\frac{dI}{dx}(x) = -i\eta U_+(x) - \eta' U_-(x) + i\omega CV,$$

where  $C$  is the capacitance per unit length. The coefficients  $\eta$  and  $\eta'$  can be defined in various ways (see [26]). One of them yields  $\eta = 2\bar{\zeta}$  and  $\eta' = 2\zeta$ , where  $\zeta$  is the transduction parameter. Assembling the equations for  $U_+$ ,  $U_-$  and  $I$ , we eventually obtain the system of COM equations

$$\frac{dU_+}{dx}(x) = -i\theta_u U_+(x) - i\kappa_{12} U_-(x) + i\zeta V, \quad (1.3)$$

$$\frac{dU_-}{dx}(x) = +i\bar{\kappa}_{12} U_+(x) + i\theta_u U_-(x) - i\bar{\zeta} V, \quad (1.4)$$

$$\frac{dI}{dx}(x) = -2i\bar{\zeta} U_+(x) - 2i\zeta U_-(x) + i\omega CV. \quad (1.5)$$

This model provides an effective and simple approach to a SAW device and is extensively used in design works. The model is phenomenological, which means its parameters have to be determined from simulations or measurements.

The analysis of the system of COM differential equations (1.3)–(1.5) delivers valuable information about the propagation of SAW. Its solution can be found as a sum of that of the corresponding homogeneous system and a particular solution of the original system. The homogeneous system reads

$$\frac{dU_+}{dx}(x) = -i\theta_u U_+(x) - i\kappa_{12} U_-(x), \quad (1.6)$$

$$\frac{dU_-}{dx}(x) = +i\bar{\kappa}_{12} U_+(x) + i\theta_u U_-(x). \quad (1.7)$$

Obviously, it corresponds to the short-circuited (SC) mode of the device. Its non-zero solution exists only if

$$\begin{vmatrix} -i\theta_u - \Lambda & -i\kappa_{12} \\ i\bar{\kappa}_{12} & i\theta_u - \Lambda \end{vmatrix} = \Lambda^2 + \theta_u^2 - |\kappa_{12}|^2 = 0.$$

Therefore, it follows that  $\Lambda = \pm i\sqrt{\theta_u^2 - |\kappa_{12}|^2} = \pm i\Delta$ , and the solution of the system (1.6), (1.7) reads

$$\begin{pmatrix} U_+^{\text{SC}}(x) \\ U_-^{\text{SC}}(x) \end{pmatrix} = C_+ \begin{pmatrix} 1 \\ \Gamma_+ \end{pmatrix} e^{-i\Delta x} + C_- \begin{pmatrix} \Gamma_- \\ 1 \end{pmatrix} e^{i\Delta x}, \quad (1.8)$$

where

$$\begin{aligned}\Delta &= \begin{cases} -\sqrt{\theta_u^2 - |\kappa_{12}|^2}, & \theta_u < -|\kappa_{12}|, \\ -i\sqrt{|\kappa_{12}|^2 - \theta_u^2}, & |\theta_u| < |\kappa_{12}|, \\ \sqrt{\theta_u^2 - |\kappa_{12}|^2}, & \theta_u > |\kappa_{12}|; \end{cases} \\ \Gamma_+ &= \frac{\Delta - \theta_u}{\kappa_{12}}; \\ \Gamma_- &= \frac{\Delta - \theta_u}{\bar{\kappa}_{12}} \end{aligned}$$

and  $C_+, C_-$  are constants determined from boundary conditions. A particular solution is defined in the following form

$$\begin{pmatrix} \tilde{U}_+ \\ \tilde{U}_- \end{pmatrix} = \begin{pmatrix} A_+ \\ A_- \end{pmatrix} V. \quad (1.9)$$

Substituting (1.9) into (1.3), (1.4), one determines the coefficients

$$\begin{aligned} A_+ &= \frac{\theta_u \zeta - \kappa_{12} \bar{\zeta}}{\Delta^2}, \\ A_- &= \frac{\theta_u \bar{\zeta} - \bar{\kappa}_{12} \zeta}{\Delta^2}. \end{aligned}$$

It is clear from (1.8) that  $\Delta = \Delta(f)$  specifies a frequency dependent wavenumber of the eigenmodes. It is called the dispersion relation. One can see that the region  $|\theta_u| < |\kappa_{12}|$ , where  $\Delta$  is pure imaginary, corresponds to the stop-band. Its width is thus determined by  $|\kappa_{12}|$ . The waves attenuate within the stop-band owing to Bragg's reflection, and the attenuation coefficients  $\Gamma_{\pm}$  reach their maximums at  $\beta_u = 0$ . The frequencies at which  $\Delta = 0$  give the edges of the stop-band. Considering the principal harmonics with  $M = 1$ , we can write  $\theta_u = \beta_u - \pi/p = 2\pi f/v - 2\pi/\lambda$ . The stop-band frequencies therefore fulfil the equation

$$\Delta^2(f) = \left( \frac{2\pi f}{v} - \frac{2\pi}{\lambda} \right)^2 - |\kappa_{12}|^2 = 0. \quad (1.10)$$

Moreover, one finds from Bragg's condition that  $f_0 = v/\lambda$ , which according to (1.10) results in

$$f_{\pm}^{\text{SC}} = f_0 \left( 1 \pm \frac{|\kappa_p|}{2\pi} \right), \quad (1.11)$$

where  $|\kappa_p| = |\kappa_{12}| \lambda$ .

Similarly, we can take the open-grating (OG) mode into consideration setting  $I = 0$

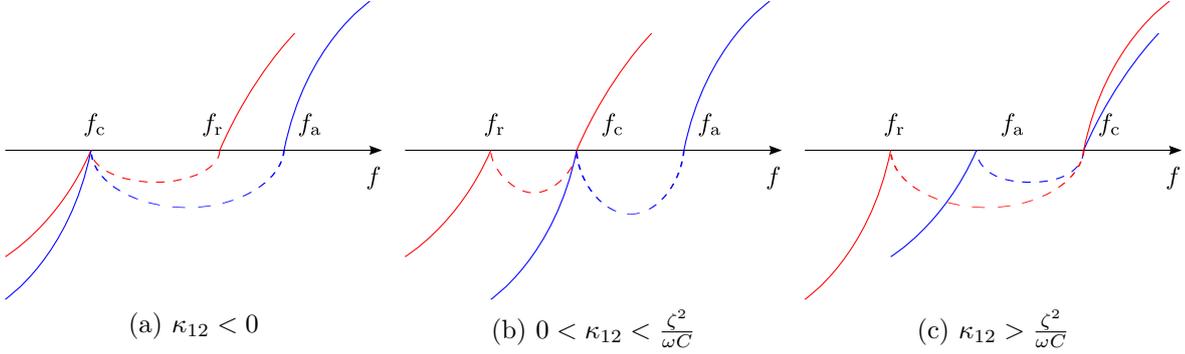


Figure 1.1: Principal look of the dispersion curves vs.  $\kappa_{12}$ : real (solid) and imaginary (dashed) parts

in (1.5). This yields

$$V = \frac{2}{\omega C} (\bar{\zeta} U_+ + \zeta U_-). \quad (1.12)$$

Substituting (1.12) for  $V$  in (1.3), (1.4), we arrive at

$$\frac{dU_+}{dx}(x) = -i\theta'_u U_+(x) - i\kappa'_{12} U_-(x), \quad (1.13)$$

$$\frac{dU_-}{dx}(x) = +i\bar{\kappa}'_{12} U_+(x) + i\theta'_u U_-(x). \quad (1.14)$$

The parameters  $\theta'_u$  and  $\kappa'_{12}$  are defined as follows

$$\theta'_u = \theta_u - \frac{2|\zeta|^2}{\omega C}, \quad \kappa'_{12} = \kappa_{12} - \frac{2\zeta^2}{\omega C}.$$

The solution for the open-grating mode coincides with that for the short-circuited mode (1.8) if we replace  $\theta_u$  and  $\kappa_{12}$  by  $\theta'_u$  and  $\kappa'_{12}$  respectively. The corresponding dispersion relation reads

$$\Delta^2 = \left( \frac{\omega}{v} - \frac{2\pi}{\lambda} - \frac{2|\zeta|^2}{\omega C} \right)^2 - \left| \kappa_{12} - \frac{2\zeta^2}{\omega C} \right|^2 = 0. \quad (1.15)$$

Suppose that  $\arg \kappa_{12} = \arg \zeta = 0$ . Then one can notice that the dispersion relations (1.10) and (1.15) have two identical roots; namely,  $\theta_u^{(1)} = \kappa_{12}$ . The other two roots are  $\theta_u^{(2)} = -\kappa_{12}$  and  $\theta_u^{(3)} = -\kappa_{12} + \frac{2\zeta^2}{\omega C}$ . This means that the dispersion relations have at least one point in common. Depending on the sign of  $\kappa_{12}$ , the dispersion curves corresponding to  $\Delta^{\text{SC}}$  and  $\Delta^{\text{OG}}$  can in principle look as shown in fig. 1.1. The frequencies  $f_r$  and  $f_a$  correspond to the resonant and the anti-resonant ones and are related to  $\theta_u^{(2)}$  and  $\theta_u^{(3)}$  respectively. Note that  $f_a > f_r$  independent of  $\kappa_{12}$ . Once the frequencies  $f_r, f_a$ ,

and  $f_c$  have been determined (through measurements or simulations), one obtains the dispersion relations (1.10), (1.15).

## 1.2 P-matrix model

The P-matrix model [11] is closely related to the previously discussed COM model and, same as the last, couples the incident and the reflected waves, the voltage, and the current. The P-matrix model is based on the “black box” principle and describes a certain part of the simulated device. Therefore, it can be considered as a discrete equivalent of the COM model. The use of the P-matrix model assumes that the device exhibits only one type of acoustic waves [1].

A three-ports “black box” can be schematically drawn as shown in fig. 1.2, and the P-matrix coupling is defined as follows

$$\begin{pmatrix} b_1 \\ b_2 \\ I \end{pmatrix} = \begin{pmatrix} p_{11} & p_{12} & p_{13} \\ p_{21} & p_{22} & p_{23} \\ p_{31} & p_{32} & p_{33} \end{pmatrix} \begin{pmatrix} a_1 \\ a_2 \\ V \end{pmatrix}. \quad (1.16)$$

If the electric behaviour of the device is not taken into account, one refers to the scattering matrix [26]

$$\begin{pmatrix} b_1 \\ b_2 \end{pmatrix} = \begin{pmatrix} s_{11} & s_{12} \\ s_{21} & s_{22} \end{pmatrix} \begin{pmatrix} a_1 \\ a_2 \end{pmatrix}. \quad (1.17)$$

The reciprocity property of a SAW device ensures that  $s_{12} = s_{21}$ . If the device is symmetrical, then  $s_{11} = s_{22}$  [26]. It is easy to find the elements of the scattering matrix (1.17) –which coincide with the corresponding elements of the P-matrix (1.16) – from the COM equations. Let the length of the device be  $L$ . Consider the short-circuited mode that is described by the system (1.6), (1.7). The last has a solution in the form (1.8). Obviously (see fig. 1.2), the values  $a_1$  and  $a_2$  are equal to the amplitudes of the incident waves  $U_+(0)$  and  $U_-(L)$  respectively. Making the substitution in (1.8), we arrive at

$$a_1 = C_+ + C_- \Gamma_-, \quad (1.18)$$

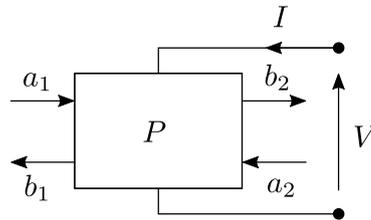


Figure 1.2: To the P-matrix definition

$$a_2 = C_+ \Gamma_+ e^{-i\Delta L} + C_- e^{i\Delta L}. \quad (1.19)$$

We solve the system (1.18), (1.19) for  $C_+$  and  $C_-$  and obtain

$$C_+ = a_1 \frac{1}{1 - \Gamma_+ \Gamma_- E^2} - a_2 \frac{\Gamma_- E}{1 - \Gamma_+ \Gamma_- E^2}, \quad (1.20)$$

$$C_- = -a_1 \frac{\Gamma_+ E^2}{1 - \Gamma_+ \Gamma_- E^2} + a_2 \frac{E}{1 - \Gamma_+ \Gamma_- E^2}, \quad (1.21)$$

where  $E = e^{-i\Delta L}$ . On the other hand,  $b_1 = U_-(0)$  and  $b_2 = U_+(L)$ , which together with (1.20) and (1.21) yields

$$b_1 = a_1 \frac{\Gamma_+ (1 - E^2)}{1 - \Gamma_+ \Gamma_- E^2} + a_2 \frac{E (1 - \Gamma_+ \Gamma_-)}{1 - \Gamma_+ \Gamma_- E^2} = s_{11} a_1 + s_{12} a_2, \quad (1.22)$$

$$b_2 = a_1 \frac{E (1 - \Gamma_+ \Gamma_-)}{1 - \Gamma_+ \Gamma_- E^2} + a_2 \frac{\Gamma_- (1 - E^2)}{1 - \Gamma_+ \Gamma_- E^2} = s_{21} a_1 + s_{22} a_2. \quad (1.23)$$

Assuming that there is no power loss, one gets [1]

$$\begin{aligned} |s_{11}|^2 + |s_{12}|^2 &= |s_{22}|^2 + |s_{21}|^2 = 1, \\ s_{11} \bar{s}_{12} + \bar{s}_{22} s_{12} &= 0. \end{aligned}$$

The other elements of the P-matrix can be obtained in the same way. For the sake of brevity we only list their values without a detailed derivation:

$$\begin{aligned} p_{13} &= \frac{(1 - E) [A_- (1 + \Gamma_+ \Gamma_- E) A_+ \Gamma_+ (1 + E)]}{1 - \Gamma_+ \Gamma_- E^2}, \\ p_{23} &= \frac{(1 - E) [A_+ (1 + \Gamma_+ \Gamma_- E) A_- \Gamma_- (1 + E)]}{1 - \Gamma_+ \Gamma_- E^2}, \\ p_{33} &= \frac{2(1 - E)}{\Delta (1 - \Gamma_+ \Gamma_- E^2)} \left[ (A_+ - A_- \Gamma_- E) (\bar{\zeta} + \zeta \Gamma_+) + \right. \\ &\quad \left. + (A_- - A_+ \Gamma_+ E) (\zeta + \bar{\zeta} \Gamma_-) \right] - i2L (A_+ \bar{\zeta} + A_- \zeta) + i\omega CL. \end{aligned}$$

Note that  $p_{31} = -2p_{13}$  and  $p_{32} = -2p_{23}$  [1]. In case of a symmetric device  $p_{13} = p_{23}$ , and the expressions for the P-matrix elements become simpler (see for example [25]).

A significant property of the P-matrix model is that it is possible to assemble two P-matrices into a single one. It makes the model useful for wide range of applications. Indeed, let two parts of a SAW device be cascade-connected acoustically and parallel-connected electrically, and let them be described by the P-matrices  $P^A$  and  $P^B$ ,

respectively<sup>1</sup>. Then the resultant P-matrix is defined as follows [25, 26]

$$\begin{aligned}
 p_{11} &= p_{11}^A + p_{11}^B \frac{p_{21}^A p_{12}^A}{1 - p_{11}^B p_{22}^A}, \quad p_{12} = \frac{p_{12}^A p_{12}^B}{1 - p_{11}^B p_{22}^A}, \quad p_{22} = p_{22}^A + p_{22}^B \frac{p_{12}^B p_{21}^B}{1 - p_{11}^B p_{22}^A}, \\
 p_{13} &= p_{13}^A + p_{12}^A \frac{p_{13}^B + p_{11}^B p_{23}^A}{1 - p_{11}^B p_{22}^A}, \quad p_{23} = p_{23}^A + p_{21}^A \frac{p_{23}^B + p_{22}^B p_{13}^A}{1 - p_{11}^B p_{22}^A}, \\
 p_{33} &= p_{33}^A + p_{33}^B + p_{32}^A \frac{p_{13}^B + p_{11}^B p_{23}^A}{1 - p_{11}^B p_{22}^A} + p_{31}^B \frac{p_{23}^B + p_{22}^B p_{13}^A}{1 - p_{11}^B p_{22}^A}.
 \end{aligned}$$

This means that one can model very complex SAW devices by means of the P-matrix model using right-to-left assembling of the P-matrices for individual parts. The last are in their turn obtainable as soon as the COM parameters are known.

We should remind that the P-matrix model remains phenomenological as it is based on the COM model. Therefore, one must possess the required parameters. Further we shall consider the development of a numerical approach that in the end allows us to extract the COM parameters in order to proceed to simulations using the COM/P-matrix technique.

### 1.3 Parameters extraction techniques. Harmonic admittance

In this section we show how the input parameters for the COM/P-matrix model can be derived by means of the stop-band analysis of an IDT. Let the edges of the stop-bands – i.e. the frequencies  $f_r$ ,  $f_a$ , and  $f_c$  – be known from either measurements or simulations. First, we recollect the expressions for the stop-band edges in the SC mode (1.11):

$$\begin{aligned}
 f_+^{\text{SC}} &= f_0 \left( 1 + \frac{|\kappa_p|}{2\pi} \right), \\
 f_-^{\text{SC}} &= f_0 \left( 1 - \frac{|\kappa_p|}{2\pi} \right).
 \end{aligned}$$

Summing  $f_+^{\text{SC}}$  and  $f_-^{\text{SC}}$ , we obtain the center frequency

$$f_0 = \frac{f_+^{\text{SC}} + f_-^{\text{SC}}}{2}$$

and therefore the velocity of SAW propagating under the periodic grating

$$v_{\text{SAW}} = \lambda f_0 = \frac{\lambda (f_+^{\text{SC}} + f_-^{\text{SC}})}{2}. \quad (1.24)$$

---

<sup>1</sup>“B” is to the right of “A”

Thereby we get the detuning factor

$$\theta_u(f) = \frac{\omega}{\lambda} - \frac{2\pi}{\lambda} = \frac{2\pi(f - f_0)}{v_{\text{SAW}}}.$$

The subtraction of  $f_-^{\text{SC}}$  from  $f_+^{\text{SC}}$  yields the reflection coefficient

$$|\kappa_p| = |\kappa_{12}\lambda| = 2\pi \frac{f_+^{\text{SC}} - f_-^{\text{SC}}}{f_+^{\text{SC}} + f_-^{\text{SC}}}. \quad (1.25)$$

Since either of the stop-band edges corresponds to  $f_r$  and  $f_c$ , their position relative to one another determines the sign of  $\kappa_p$ .

Now, let us have a look at the dispersion relation in the OG-mode (1.15). For real  $\zeta$  and  $\kappa_{12}$  one of its roots coincides with the anti-resonant frequency  $f_a$ . Namely,

$$\frac{2\pi(f_a - f_0)}{v_{\text{SAW}}} = -\kappa_{12} + \frac{2\zeta^2}{\pi f_a C}.$$

Then, we multiply the last expression by  $v_{\text{SAW}} f_a C / (2\pi)$ , which in the end yields

$$C \left[ f_a - f_0 \left( 1 - \frac{\kappa_p}{2\pi} \right) \right] = \frac{f_0 \zeta^2}{\pi^2}.$$

Taking into account that  $f_r = f_0 (1 - \kappa_p / (2\pi))$  and denoting  $\delta f = f_a - f_r$ , we arrive at

$$\frac{\delta f}{f_0} = \frac{\zeta_p^2}{\pi^2 f_a C_p}, \quad (1.26)$$

where  $\zeta_p = \zeta \lambda$  and  $C_p = C \lambda$ . The quantity  $\delta f / f_0$  is known as resonance-anti-resonance distance [29].

It follows from the last equation that the transduction parameter  $\zeta$  and the capacitance  $C$  are not independent from each other. The possession of the stop-band edges is therefore not enough for the derivation of all COM parameters. However, the missing parameters can be obtained from the admittance of the device. To gain the admittance, we substitute (1.9) for  $U_{\pm}$  in (1.5). This yields

$$\frac{dI}{dx} = \left( -4i \frac{\theta_u |\zeta|^2 - \Re(\kappa_{12} \bar{\zeta}^2)}{\theta_u^2 - |\kappa_{12}|^2} + i\omega C \right) V.$$

Integrating the local current density  $dI/dx$  over the period  $\lambda$  and dividing the result by  $V$ , we arrive at

$$Y(f) = -4i\lambda \frac{\theta_u |\zeta|^2 - \Re(\kappa_{12} \bar{\zeta}^2)}{\theta_u^2 - |\kappa_{12}|^2} + i\omega C_p. \quad (1.27)$$

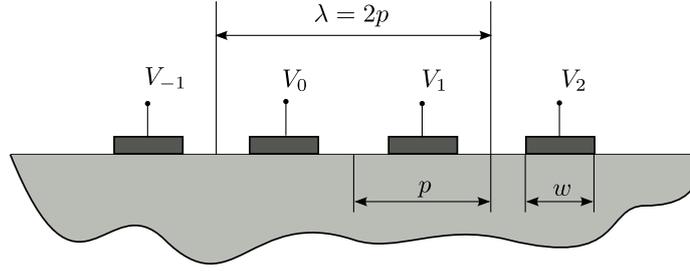


Figure 1.3: To the harmonic admittance approach

The last expression describes the admittance of a unit period of an infinitely long periodic transducer in terms of the COM parameters [30]. If the admittance of the transducer is known (from measurements or simulations), we can fit it with the COM admittance (1.27) and hence get the desired parameters.

Now, the goal is to obtain the stop-band edges and the admittance as the results of FEM or FEM/BEM simulations. The concept that becomes very useful here is referred to as the harmonic admittance. It was suggested by Bløtekjær *et al.* in [31]<sup>2</sup> and further developed and widely used by many authors [29, 32, 33]. This technique is based on the following approach. Consider an infinite periodic electrode grating placed on the top of a piezoelectric substrate (see fig. 1.3). First, suppose that all the fingers were grounded except the  $m^{\text{th}}$  one. The mutual admittance  $y_{mn}$  between the  $m^{\text{th}}$  and the  $n^{\text{th}}$  fingers is defined as

$$y_{mn} = I_n/V_m.$$

It only depends on the difference between  $m$  and  $n$ , which is due to the translation symmetry of the structure [32]. Then we have  $y_{mn} = y_{m-n}$  and  $I_n = y_{m-n}V_m$ . If more electrodes are loaded, the superposition principle yields

$$I_n = \sum_{m=-\infty}^{+\infty} y_{m-n}V_m. \quad (1.28)$$

Let the voltage be harmonic in physical space domain [32], i.e. in general case we have

$$V_n = V e^{-i2\pi n\delta}. \quad (1.29)$$

Equation (1.29) specifies a quasi-periodic function with a period  $p$ :  $V_{n+1} = V_n e^{-i2\pi\delta}$ . The substitution of (1.29) for  $V_n$  in (1.28) results in

$$I_n = V \sum_{m=-\infty}^{+\infty} y_{m-n} e^{-i2\pi m\delta}. \quad (1.30)$$

The harmonic admittance  $Y$  is defined as the ratio between  $I_n$  and  $V_n$ . Taking into

<sup>2</sup>They used the term “strip admittance” in [31]

account that the current  $I_n$  is a function of the frequency and the periodicity  $\delta$ , (1.29) and (1.30) yield

$$Y(f, \delta) = \frac{I_n(f, \delta)}{V} = \sum_{m=-\infty}^{+\infty} y_m e^{-i2\pi m\delta}. \quad (1.31)$$

The mutual admittance is then defined as

$$y_m(f) = \int_0^1 Y(f, \delta) e^{-i2\pi m\delta} d\delta.$$

It follows from (1.31) that the harmonic admittance is a periodic function with the period  $p = 1$ . The reciprocity  $y_m = y_{-m}$  yields the symmetry of the harmonic admittance about  $\delta = 1/2$ . The case  $\delta = 0$  obviously corresponds to a grounded grating ( $V_n$  is a constant); the case  $\delta = 1/2$ , to an infinitely long periodic single electrode transducer ( $V_{n+1} = -V_n$ ) [29]. The functions  $\delta^{\text{SC}}(f)$  and  $\delta^{\text{OG}}(f)$  correspond to the poles and the zeros of  $Y(f, \delta)$ , respectively and give the dispersion curves for the short and open circuit modes of the device [29]. Plessky *et al.* showed in [33] the validity of the following formula

$$Y(f, \delta) = \frac{\Delta^{\text{OG}}(f, \delta)}{\Delta^{\text{SC}}(f, \delta)}, \quad (1.32)$$

where  $\Delta^{\text{OG}}(f, \delta)$  and  $\Delta^{\text{SC}}(f, \delta)$  are the dispersion relation for the open- and short-circuited electrodes. At the same time, these relations are parts of the COM-model (see (1.10), (1.15)).

On the other hand, the admittance (1.31) is obtainable as

$$Y(f, \delta) = \frac{I(f, \delta)}{V} = \frac{i\omega q_e(f, \delta)}{V}, \quad (1.33)$$

where  $q_e$  is the total electric charge distributed over the electrode surface. It is seen from (1.32) that the poles of the admittance correspond to the zeros of  $\Delta^{\text{SC}}$ , and its roots coincide with those of  $\Delta^{\text{OG}}$ . Fitting the admittance (1.32) with (1.33), we are able to extract desired parameters of the COM model from FEM or FEM/BEM simulations.

---

## Mathematical description of wave propagation in piezoelectric media

---

### 2.1 Principles of linear elasticity and electrostatics

As we have said earlier in the introduction, the phenomenon of piezoelectricity presents a coupling between mechanical and electric fields. The mathematical model that illustrates the behaviour of a piezoelectric material must therefore take both contributions into account. In order to describe the mechanical field, we take a small part  $\Delta\Omega$  of a solid yet deformable body  $\Omega$  that is subjected to external forces and supposed to be in a state of equilibrium. We denote the boundary of  $\Delta\Omega$  by  $\Delta\Gamma$  and define the densities of the surface and the volume forces as  $\mathbf{f}_S = \frac{\Delta\mathbf{F}_S}{\Delta\Gamma}$  and  $\mathbf{f}_V = \frac{\Delta\mathbf{F}_V}{\Delta\Omega}$ , respectively. Then, following the stress principle of Euler and Cauchy [34], there exists a vector  $\mathbf{T}^{(n)}(\mathbf{x}) = \mathbf{f}_S(\mathbf{x})$  at any point  $\mathbf{x}$  of the surface  $\Delta\Gamma$  where a normal vector  $\mathbf{n}$  can be defined. And the state of equilibrium is described by the axiom of force balance

$$\int_{\Delta\Omega} \mathbf{f}_V d\Omega + \oint_{\Delta\Gamma} \mathbf{T}^{(n)} d\Gamma = 0 \quad (2.1)$$

and the axiom of moment balance

$$\int_{\Delta\Omega} \mathbf{r} \times \mathbf{f}_V d\Omega + \oint_{\Delta\Gamma} \mathbf{r} \times \mathbf{T}^{(n)} d\Gamma = 0. \quad (2.2)$$

The vector  $\mathbf{T}^{(n)}$  is called the Cauchy stress vector, and the equations (2.1), (2.2) hold for any  $\Delta\Omega \in \Omega$ .

Cauchy's theorem [34] states that the stress vector is coupled with the surface normal

through a second order tensor field  $[\boldsymbol{\sigma}]$  called Cauchy stress tensor

$$\Delta \mathbf{F}_S = \mathbf{T}^{(n)} \Delta \Gamma = [\boldsymbol{\sigma}] \mathbf{n} \Delta \Gamma. \quad (2.3)$$

Moreover, the Cauchy stress tensor is defined in such a way that

$$\nabla \cdot [\boldsymbol{\sigma}] + \mathbf{f}_V = 0, \quad (2.4)$$

$$[\boldsymbol{\sigma}] = [\boldsymbol{\sigma}]^T, \quad (2.5)$$

which follows from the axioms (2.1), (2.2) after the substitution  $[\boldsymbol{\sigma}] \mathbf{n}$  for  $\mathbf{T}^{(n)}$  and applying the divergence theorem [34]. Taking (2.5) into account, we can write  $[\boldsymbol{\sigma}]$  in a Cartesian coordinate system as

$$[\boldsymbol{\sigma}] = \begin{pmatrix} \sigma_{xx} & \sigma_{xy} & \sigma_{xz} \\ \sigma_{xy} & \sigma_{yy} & \sigma_{yz} \\ \sigma_{xz} & \sigma_{yz} & \sigma_{zz} \end{pmatrix} = \begin{pmatrix} \sigma_{11} & \sigma_{12} & \sigma_{13} \\ \sigma_{12} & \sigma_{22} & \sigma_{23} \\ \sigma_{13} & \sigma_{23} & \sigma_{33} \end{pmatrix}.$$

The symmetry of  $[\boldsymbol{\sigma}]$  makes it possible to regard it as a six-component algebraic vector using Voigt notation [35], namely

$$\boldsymbol{\sigma} = (\sigma_{xx} \ \sigma_{yy} \ \sigma_{zz} \ \sigma_{yz} \ \sigma_{xz} \ \sigma_{xy})^T = (\sigma_1 \ \sigma_2 \ \sigma_3 \ \sigma_4 \ \sigma_5 \ \sigma_6)^T.$$

After that the equilibrium equation (2.4) reads [35]

$$\mathcal{B}^T \boldsymbol{\sigma} + \mathbf{f}_V = 0, \quad (2.6)$$

where

$$\mathcal{B} = \begin{pmatrix} \frac{\partial}{\partial x} & 0 & 0 & 0 & \frac{\partial}{\partial z} & \frac{\partial}{\partial y} \\ 0 & \frac{\partial}{\partial y} & 0 & \frac{\partial}{\partial z} & 0 & \frac{\partial}{\partial x} \\ 0 & 0 & \frac{\partial}{\partial z} & \frac{\partial}{\partial y} & \frac{\partial}{\partial x} & 0 \end{pmatrix}.$$

If a non-static case is considered, then, according to Newton's second law of motion, the resultant of the external loads is proportional to the acceleration  $\mathbf{a}$  of the body. Thus we shall write (2.6) as

$$\mathcal{B}^T \boldsymbol{\sigma} + \mathbf{f}_V = \rho \mathbf{a}, \quad (2.7)$$

where  $\rho$  is the volume mass density of the body.

Let  $\Omega_0$  be the state of the body  $\Omega$  before the external forces have been applied, which we will further refer to as the reference configuration. Then there is a map  $\mathbf{x} = \boldsymbol{\Phi}(\mathbf{X}, t)$  that associates a point  $\mathbf{X}$  of the reference configuration  $\Omega_0$  with a point  $\mathbf{x}$  of the deformed body  $\Omega$ . The difference between these point defines the displacement vector

$$\mathbf{u}(\mathbf{X}, t) = \mathbf{x}(\mathbf{X}, t) - \mathbf{X}. \quad (2.8)$$

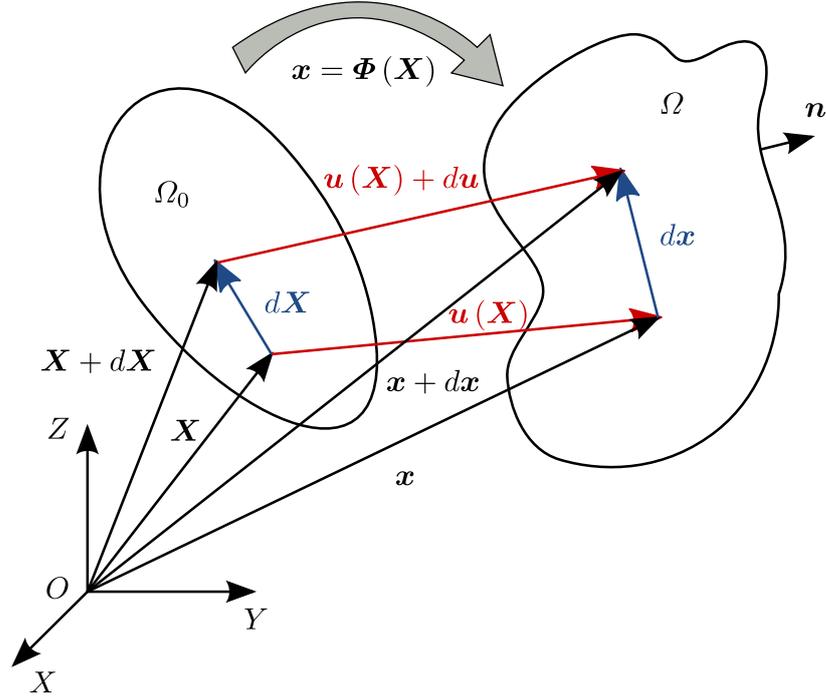


Figure 2.1: Finite deformation of a solid body

A line element  $d\mathbf{x}$  of the deformed body is related to that  $d\mathbf{X}$  of the reference one as

$$d\mathbf{x} = \frac{\partial \Phi}{\partial \mathbf{X}} d\mathbf{X} = [\mathbf{F}] d\mathbf{X}. \quad (2.9)$$

Here,  $\frac{\partial \Phi}{\partial \mathbf{X}}$  is the Jacobian matrix of the vector field  $\Phi$

$$\frac{\partial \Phi}{\partial \mathbf{X}} = \begin{pmatrix} \frac{\partial \Phi_x}{\partial X} & \frac{\partial \Phi_x}{\partial Y} & \frac{\partial \Phi_x}{\partial Z} \\ \frac{\partial \Phi_y}{\partial X} & \frac{\partial \Phi_y}{\partial Y} & \frac{\partial \Phi_y}{\partial Z} \\ \frac{\partial \Phi_z}{\partial X} & \frac{\partial \Phi_z}{\partial Y} & \frac{\partial \Phi_z}{\partial Z} \end{pmatrix}.$$

A volume element  $dv$  of the deformed body is defined through the scalar triple product of three vectors

$$dv = [d\mathbf{x}_1 \times d\mathbf{x}_2] \cdot d\mathbf{x}_3.$$

According to (2.9) it is equal to

$$dv = |\det[\mathbf{F}]| dV = JdV. \quad (2.10)$$

It follows from (2.10) that  $\rho_0 = J\rho$ , which provides the conservation of mass. An oriented surface element  $d\mathbf{a} = \mathbf{n}da$  in the current state is connected to that  $d\mathbf{A} = \mathbf{N}dA$  of the

reference state through Nanson's formula [36]

$$\mathbf{n} da = J [\mathbf{F}]^{-T} \mathbf{N} dA. \quad (2.11)$$

As a measure of deformations we introduce the Green-Lagrangian strain tensor  $[\mathbf{E}]$

$$[\mathbf{E}] = \frac{1}{2} \left( [\mathbf{F}]^T [\mathbf{F}] - [\mathbf{I}] \right).$$

It shows the change of the squared length of the element  $d\mathbf{X}$  as a result of deformations [37]

$$d\mathbf{x}^T d\mathbf{x} - d\mathbf{X}^T d\mathbf{X} = d\mathbf{X}^T \left( [\mathbf{F}]^T [\mathbf{F}] - [\mathbf{I}] \right) d\mathbf{X} = d\mathbf{X}^T 2[\mathbf{E}] d\mathbf{X}.$$

Taking (2.8) and (2.9) into account, we can write

$$[\mathbf{E}] = \frac{1}{2} \left( \nabla_{\mathbf{X}} \mathbf{u} + (\nabla_{\mathbf{X}} \mathbf{u})^T + (\nabla_{\mathbf{X}} \mathbf{u})^T \nabla_{\mathbf{X}} \mathbf{u} \right). \quad (2.12)$$

In case of infinitesimal deformations the second order terms in (2.12) can be neglected. Moreover, we do not distinguish between the reference and the deformed configurations, which yields

$$[\mathbf{S}] = \frac{1}{2} \left( \nabla_{\mathbf{x}} \mathbf{u} + (\nabla_{\mathbf{x}} \mathbf{u})^T \right). \quad (2.13)$$

The tensor  $[\mathbf{S}]$  is obviously symmetric, i.e. it has only six distinct components. Therefore it can also be written as a six-component algebraic vector in Voigt form

$$\mathbf{S} = \left( S_{xx} \ S_{yy} \ S_{zz} \ 2S_{yz} \ 2S_{xz} \ 2S_{xy} \right)^T = \left( S_1 \ S_2 \ S_3 \ S_4 \ S_5 \ S_6 \right)^T.$$

The expression (2.13) then reads

$$\mathbf{S} = \mathcal{B} \mathbf{u}. \quad (2.14)$$

As regard to the electric field, we use quasi-static approximation to describe it. This approximation is adequate for the waves in piezoelectric media, because the elastic disturbances travel much slower than the electric ones [1]. The electric field intensity  $\mathbf{E}$  is then irrotational and is defined by the electric potential  $\varphi$

$$\nabla \times \mathbf{E} = 0; \text{ therefore, } \mathbf{E} = -\nabla \varphi. \quad (2.15)$$

The electric displacement field  $\mathbf{D}$  fulfils Gauss's law

$$\nabla \cdot \mathbf{D} = \varrho_e, \quad (2.16)$$

where  $\varrho_e$  is the volume density of free electric charge.

The equations (2.6), (2.16) describe the mechanical and the electric fields in piezoelec-

tric materials. The fields are not independent from each other, but are coupled by means of the constitutive equations. The last can be derived in various forms from different thermodynamic potentials [5]. For linear piezoelectric materials the total work is given by the sum of the mechanical and the electric work. Then, in the absence of a heat flux, the differential form of the inner energy density reads [35]

$$dU = [\boldsymbol{\sigma}] : d[\mathbf{S}] + \mathbf{E} \cdot d\mathbf{D}. \quad (2.17)$$

The substitution of (2.17) into the differential form for the electric Gibbs energy (electric enthalpy) [5]  $G_e = U - \mathbf{E} \cdot \mathbf{D}$  yields

$$dG_e = [\boldsymbol{\sigma}] : d[\mathbf{S}] - \mathbf{D} \cdot d\mathbf{E}.$$

From the last expression we obtain that

$$\sigma_{ij} = \left. \frac{\partial G_e}{\partial S_{ij}} \right|_E, \quad D_i = \left. \frac{\partial G_e}{\partial E_i} \right|_S,$$

where the subscripts mean that the corresponding field remains constant.

Regarding the stress and the electric displacement as functions of the strain and the electric field intensity, we can write their differentials as follows

$$d\sigma_{ij}([\mathbf{S}], \mathbf{E}) = \sum_{k,l} \left. \frac{\partial \sigma_{ij}}{\partial S_{kl}} \right|_E dS_{kl} + \sum_k \left. \frac{\partial \sigma_{ij}}{\partial E_k} \right|_S dE_k, \quad (2.18)$$

$$dD_i([\mathbf{S}], \mathbf{E}) = \sum_{j,k} \left. \frac{\partial D_i}{\partial S_{jk}} \right|_E dS_{jk} + \sum_j \left. \frac{\partial D_i}{\partial E_j} \right|_S dE_j. \quad (2.19)$$

The partial derivatives in (2.18), (2.19) define the material tensors. Namely,

- $\left. \frac{\partial \sigma_{ij}}{\partial S_{kl}} \right|_E = c_{ijkl}^E$  is the 4<sup>th</sup> rank tensor of elastic stiffness moduli,
- $\left. \frac{\partial D_i}{\partial S_{jk}} \right|_E = - \left. \frac{\partial \sigma_{ij}}{\partial E_k} \right|_S = e_{ijk}$  is the 3<sup>rd</sup> rank tensor of piezoelectric constants,
- $\left. \frac{\partial D_i}{\partial E_j} \right|_S = \varepsilon_{ij}^S$  is the 2<sup>nd</sup> rank tensor of dielectric permittivity.

Applying Voigt notation and taking the symmetry of the material tensors [5] into account, we come to the following form of constitutive equations

$$\boldsymbol{\sigma} = [\mathbf{c}^E] \mathbf{S} - [\mathbf{e}]^T \mathbf{E}, \quad (2.20)$$

$$\mathbf{D} = [\mathbf{e}] \mathbf{S} + [\boldsymbol{\varepsilon}^S] \mathbf{E}. \quad (2.21)$$

The expressions (2.20), (2.21) make up a so-called e-form of the constitutive equations [35]. This model is suitable for further steps in the sense that we can directly

substitute (2.20) and (2.21) for  $\boldsymbol{\sigma}$  and  $\mathbf{D}$  in (2.6) and (2.16) respectively. Taking (2.13), (2.15) and the fact that  $\mathbf{a} = \frac{\partial^2 \mathbf{u}}{\partial t^2}$  into account, we obtain

$$\mathcal{B}^T \left( [\mathbf{c}^E] \mathcal{B} \mathbf{u} + [\mathbf{e}]^T \nabla \varphi \right) + \mathbf{f}_V = \rho \frac{\partial^2 \mathbf{u}}{\partial t^2}, \quad (2.22)$$

$$\nabla \cdot \left( [\mathbf{e}] \mathbf{u} - [\boldsymbol{\varepsilon}^S] \nabla \varphi \right) = \varrho_e. \quad (2.23)$$

The system of partial differential equations (2.22), (2.23) thoroughly describes the propagation of elastic waves in linear piezoelectric materials. Note that in case of absence of piezoelectric properties, i.e. when  $[\mathbf{e}] = 0$ , the system (2.22), (2.23) splits into two independent partial differential equations for mechanics and electrostatics.

## 2.2 Elastic waves in solids. Slowness curves

In order to study what kind of waves can propagate in certain piezoelectric materials, we consider the system (2.22), (2.23) in case of the absence of external forces, i.e.  $\mathbf{f}_V = 0$ . We seek for a plane wave solution of the form

$$\begin{pmatrix} \mathbf{u} \\ \varphi \end{pmatrix} (\mathbf{x}, t) = \begin{pmatrix} \underline{u} \\ \underline{\varphi} \end{pmatrix} \cdot e^{i(\omega t - \mathbf{k} \cdot \mathbf{x})},$$

where the vector  $\mathbf{k} = k_x \mathbf{e}_x + k_y \mathbf{e}_y + k_z \mathbf{e}_z$  points to the wave propagation direction. In such a case the operators  $\mathcal{B}$  and  $\nabla$  take the following form

$$\mathcal{B} = - \begin{pmatrix} k_x & 0 & 0 & 0 & k_z & k_y \\ 0 & k_y & 0 & k_z & 0 & k_x \\ 0 & 0 & k_z & k_y & k_x & 0 \end{pmatrix} = \underline{\underline{B}}, \quad \nabla = - \begin{pmatrix} k_x \\ k_y \\ k_z \end{pmatrix} = \underline{\underline{D}},$$

and we are able to write

$$\begin{aligned} \underline{\underline{B}}^T [\mathbf{c}^E] \underline{\underline{B}} \underline{u} + \underline{\underline{B}}^T [\mathbf{e}]^T \underline{\underline{D}} \underline{\varphi} &= \omega^2 \rho \underline{u}, \\ \underline{\underline{D}}^T [\mathbf{e}] \underline{\underline{B}} \underline{u} - \underline{\underline{D}}^T [\boldsymbol{\varepsilon}^S] \underline{\underline{D}} \underline{\varphi} &= 0 \end{aligned}$$

instead of (2.22), (2.23).

Obviously,  $\underline{\varphi}$  can be expressed from the last equation. As the result, we obtain the Christoffel equation [38]

$$\underline{\underline{A}}(\mathbf{k}) \underline{u} = \omega^2 \underline{u}. \quad (2.24)$$

The equation (2.24) is an eigenvalue problem with respect to  $\omega^2$ . It has a non-trivial solution only when  $\det \left( \underline{\underline{A}}(\mathbf{k}) - \omega^2 \underline{\underline{I}} \right) = 0$ . If we introduce the phase velocity as  $v = \omega / |\mathbf{k}|$ , the solution of (2.24) will give us three velocities  $v_i$  accompanied with three polarisation vectors  $\underline{u}^{(i)}$  as functions of the propagation direction [39].

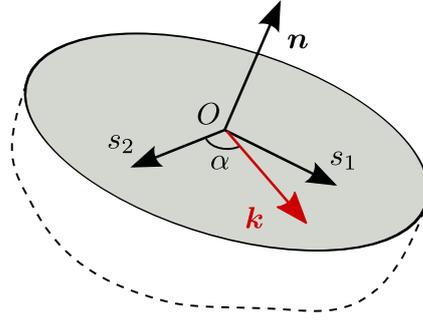


Figure 2.2: To the definition of slowness curves

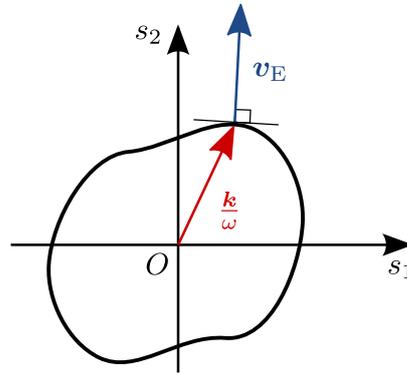


Figure 2.3: Schematic view of a slowness curve

In case of a non-piezoelectric isotropic material the solution of (2.24) consists of a longitudinal wave propagating along  $\mathbf{k}$  and two shear waves propagating orthogonal to  $\mathbf{k}$  [1, 35]. Taking the elastic stiffness tensor of an isotropic material as

$$[\mathbf{c}] = \begin{pmatrix} \lambda + 2\mu & \lambda & \lambda & 0 & 0 & 0 \\ \lambda & \lambda + 2\mu & \lambda & 0 & 0 & 0 \\ \lambda & \lambda & \lambda + 2\mu & 0 & 0 & 0 \\ 0 & 0 & 0 & \mu & 0 & 0 \\ 0 & 0 & 0 & 0 & \mu & 0 \\ 0 & 0 & 0 & 0 & 0 & \mu \end{pmatrix},$$

we obtain the following values for the longitudinal  $v_1 = v_l = \sqrt{\frac{\lambda+2\mu}{\rho}}$  and the shear  $v_{2,3} = v_s = \sqrt{\frac{\mu}{\rho}}$  wave velocities [1, 35]. The waves in isotropic materials are independent of the frequency  $\omega$  and therefore non-dispersive [1]. It should also be noted that  $v_l > v_s$ .

For a general anisotropic material pure modes do not exist, which means that the velocities  $v_i$ ,  $i = \overline{1, 3}$  are not independent of one another and therefore cannot be derived explicitly. We refer to quasi-longitudinal and quasi-shear waves in this case. Here, it is convenient to use the concept of slowness surfaces [38] which are the inverse phase

velocities  $s = 1/v$ . If we are interested in the propagation in a certain plane of the material, we refer to the slowness curves. The last are the traces of the slowness surfaces on the plane. Let the plane be orthogonal to some vector  $\mathbf{n}$ . We can introduce a polar coordinate system on it (see fig. 2.2), such that  $\mathbf{k} = |\mathbf{k}|(\mathbf{e}_x \cos \alpha + \mathbf{e}_y \sin \alpha)$ . Then we obtain the slowness curves as polar plots. The curve corresponding to the quasi-longitudinal wave will be the one whose eigenvector is the closest to the direction of propagation  $\mathbf{k}$ ; the quasi shear ones, with the eigenvectors closest to the directions  $\mathbf{n}$  and  $\mathbf{k} \times \mathbf{n}$ . An effective algorithm for making slowness curves plots from numerically calculated modes was proposed by Conry in [39].

There exist explicit forms of the slowness curves for some crystal classes, e.g. isotropic and cubic [1, 38]. In case of an isotropic material and the propagation of waves in  $xz$ -plane<sup>1</sup>, the Christoffel equation reads

$$\begin{aligned}\rho\omega^2 u_x &= (\lambda + 2\mu) k_x^2 u_x + (\lambda + \mu) k_z^2 u_z, \\ \rho\omega^2 u_y &= \mu (k_x^2 + k_z^2) u_y, \\ \rho\omega^2 u_z &= (\lambda + \mu) k_x^2 u_x + (\lambda + 2\mu) k_z^2 u_z.\end{aligned}\tag{2.25}$$

The second equation directly yields the slowness curve for the shear-horizontal wave

$$\frac{\rho}{\mu} = s_x^2 + s_z^2 = |\mathbf{s}|^2 = \frac{1}{|\mathbf{v}|^2}.\tag{2.26}$$

The other slowness curves are derived from the two remaining equations of the system (2.25). We equate its determinant to zero and obtain

$$\begin{aligned}[(\lambda + 2\mu) s_x^2 + \mu s_z^2 - \rho] [\mu s_x^2 + (\lambda + 2\mu) s_z^2 - \rho] - (\lambda + \mu) s_x^2 s_z^2 &= \\ = [\mu (s_x^2 + s_z^2) - \rho] [(\lambda + 2\mu) (s_x^2 + s_z^2) - \rho] &= 0.\end{aligned}$$

The first term of the last expression is the same as (2.26) and corresponds to the shear-vertical wave. The second one gives the slowness curve for the longitudinal wave

$$\frac{\rho}{\lambda + 2\mu} = s_x^2 + s_z^2 = |\mathbf{s}|^2 = \frac{1}{|\mathbf{v}|^2}.\tag{2.27}$$

Obviously, the slowness curves (2.26) and (2.27) are circles, and their radii are equal to the inverses of  $v_s$  and  $v_l$  respectively.

Another concept used alongside the slowness is the vector of energy velocity  $\mathbf{v}_E$ . It is related to the phase velocity  $v$  as  $\mathbf{v}_E \cdot \mathbf{k}^0 = v$  [38]. Being drawn on a slowness diagram, the vectors of the phase and the energy velocities look as shown in fig. 2.3. The vector of energy velocity indicates the propagation of energy for specific modes with respect to

---

<sup>1</sup>So that the variations in  $y$ -directions are neglected and therefore  $\partial/\partial y = 0$

a propagation direction and is always normal to the slowness surface (curve) [38]. Note that in lossless media the energy velocity  $\mathbf{v}_E$  is identical to the group velocity  $\mathbf{v}_g$  [38].

### 2.3 Surface waves in piezoelectric half-space

So far we have dealt with the waves that propagate without an attenuation in certain directions. They are referred to as bulk waves. However, they are not the only kinds of waves that exist in solids. In this section we concern ourselves with the waves propagating in a half-space occupied by an elastic (not necessary piezoelectric) material. Let us have a Cartesian coordinate system  $Oxyz$  such that the elastic material is located in the lower half-space  $z \leq 0$ . The region above is supposed to be vacuum. Assuming stress-free boundary conditions on  $z = 0$  and taking  $x$  as the propagation direction, we can find a surface wave solution named after Lord Rayleigh who first discovered it [4]. The wave existence is due to interaction of longitudinal and plane shear waves, and its wavefront is parallel to the  $y$ -axis. We give here a brief description of the properties of Rayleigh waves in isotropic materials. For more details we refer to [1] or [40]. Further derivations are in accordance with [1].

The mechanical displacement as a result of a Rayleigh wave can be written as the sum

$$\mathbf{u}_R = \mathbf{u}_l + \mathbf{u}_s, \quad (2.28)$$

where  $\mathbf{u}_l$  and  $\mathbf{u}_s$  are the longitudinal and the shear waves propagating with the velocities  $v_l = \sqrt{\frac{\lambda+2\mu}{\rho}}$  and  $v_s = \sqrt{\frac{\mu}{\rho}}$ , respectively. Suppose the wave propagates in  $x$ -direction as  $e^{-i\beta x}$ :  $\beta = \omega/v_R$ . Then the wavevectors of the corresponding longitudinal and shear waves are

$$\mathbf{k}_l = \mathbf{e}_x\beta + \mathbf{e}_z\xi, \quad \mathbf{k}_s = \mathbf{e}_x\beta + \mathbf{e}_z\eta,$$

with

$$\xi^2 = \left(\frac{\omega}{v_l}\right)^2 - \beta^2, \quad \eta^2 = \left(\frac{\omega}{v_s}\right)^2 - \beta^2.$$

The longitudinal wave propagates parallel to the vector  $\mathbf{k}_l$ ; the shear one, orthogonal to the vector  $\mathbf{k}_s$  [1]. For this reason (2.28) can be written as

$$\begin{pmatrix} u_x \\ u_z \end{pmatrix} = e^{-i\beta x} \left( A \begin{pmatrix} 1 \\ \xi/\beta \end{pmatrix} e^{-i\xi z} + B \begin{pmatrix} 1 \\ -\beta/\eta \end{pmatrix} e^{-i\eta z} \right). \quad (2.29)$$

An important thing here is that we are interested in surface wave solutions whose displacement attenuate as  $z \rightarrow -\infty$ . This means the values of  $\xi$  and  $\eta$  must be positive imaginary. Thus, it follows that

$$\left(\frac{\omega}{v_l}\right)^2 - \beta^2 < 0, \quad \left(\frac{\omega}{v_s}\right)^2 - \beta^2 < 0,$$

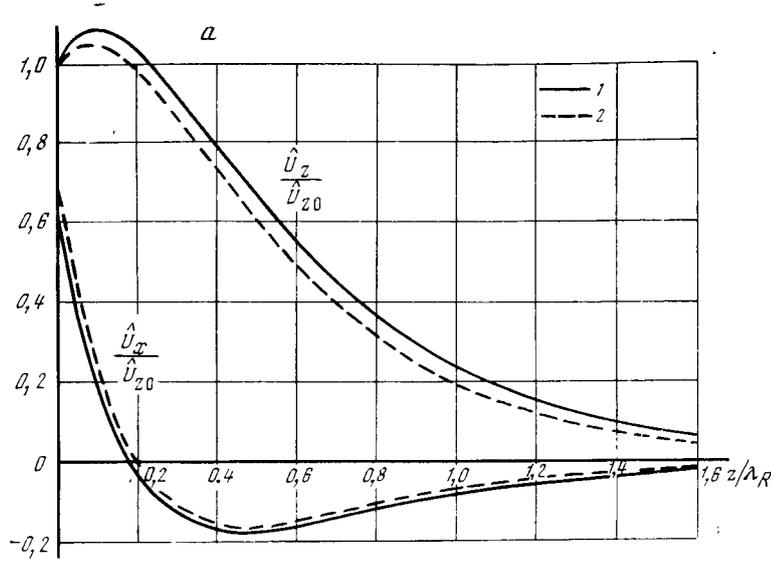


Figure 2.4: Amplitudes of the  $x$ - and  $z$ -components of the Rayleigh wave displacements for  $\nu = 0.25$  (solid line) and  $\nu = 0.34$  (dashed line) [40]

which gives us an important property of Rayleigh waves. Namely,  $v_R < v_s < v_1$ , which holds for anisotropic (and piezoelectric) materials, too.

An explicit expression for  $v_R$  is obtained through the stress-free boundary conditions on the plane  $z = 0$  [1]. Viktorov [40] gives an approximate solution in the following form

$$v_R \approx \frac{0.86 + 1.12\nu}{1 + \nu} v_s, \quad (2.30)$$

where  $\nu$  is the Poisson ratio. The components of the mechanical displacement  $u_x$ ,  $u_z$  of the Rayleigh wave are shifted by  $\pi/2$  in phase [40], and therefore the profile of the wave is an ellipse. The wave propagates in a shallow surface layer of depth between  $\lambda_R$  and  $2\lambda_R$  [40]. The displacements as functions of the normalized depth are shown in fig. 2.4.

If the material is anisotropic, the properties of surface waves depend on the propagation direction and the crystal symmetry (see for details [38]). There can arise other types of waves different from the Rayleigh ones [40]. In order to specify the orientation of a certain crystal, we shall use the common notation [1] relating the axes of the crystal lattice to the chosen Cartesian coordinate system. The material properties become therefore different for various crystal cuts and orientations.

The study of surface waves in a piezoelectric half-space requires in addition the equation for the electric potential

$$\Delta\varphi = 0, \quad z > 0$$

and electrical boundary conditions on the plane  $z = 0$ . The last can be of two types:

- free  $\frac{\partial \varphi^+}{\partial z} \Big|_{z=0} = \frac{\partial \varphi^-}{\partial z} \Big|_{z=0}$  and
- metallized  $\varphi|_{z=0} = 0$  surface.

These two cases give different velocities of surface acoustic wave:  $v_f$  and  $v_m$ . The difference between them determines the electromechanical coupling factor of SAW [26]

$$K^2 = \frac{v_f^2 - v_m^2}{v_f^2}.$$

The computation of  $v_f$  and  $v_m$  requires numerical procedures in case of arbitrary orientation of a piezoelectric crystal. The surface wave solution can thus exhibit different properties. Depending on the crystal symmetry we can get Rayleigh waves with displacements  $u_x, u_z$  coupled with or decoupled from  $\varphi$ . For some orientations there exists a Bluestein-Gulyaev wave solution with displacements  $u_y$  coupled with  $\varphi$  [1]. Other solutions are Lamb waves arising in layered media and leaky (pseudo) surface acoustic waves with their velocity higher than that of the slow shear wave [40].

## 2.4 Second order effects on wave propagation in piezoelectric media

In this section we touch upon the questions of SAW propagation under the influence of second order factors: temperature and prestressing. Both affect the velocity of SAW through the change of the shape of the considered structure and the material parameters of the crystal. These effects can also occur simultaneously, because the thermal expansion causes deformations and therefore stresses in elastic materials.

The quantities that characterise effects of the temperature are [26]:

- temperature coefficient of frequency (TCF) and
- temperature coefficient of the time delay (TCD).

The concept of temperature coefficients is based on the Taylor series expansion for corresponding quantities. Namely,

$$\xi(\tau_0 + \Delta\tau) = \xi(\tau_0) + \Delta\tau \frac{\partial \xi}{\partial \tau} \Big|_{\tau=\tau_0} + \frac{(\Delta\tau)^2}{2!} \frac{\partial^2 \xi}{\partial \tau^2} \Big|_{\tau=\tau_0} + \dots,$$

where  $\tau_0$  is a reference temperature. The first order temperature coefficient for  $\xi$  is then defined as

$$\text{TC}(\xi) = \frac{1}{\xi(\tau_0)} \frac{\partial \xi}{\partial \tau} \Big|_{\tau=\tau_0},$$

so that

$$\xi(\tau_0 + \Delta\tau) \approx \xi(\tau_0)(1 + \text{TC}(\xi)\Delta\tau).$$

The above-mentioned temperature coefficients can be derived from those of the particle and the group velocities as follows [26]

$$\begin{aligned} \text{TCF} &= \text{TCV}_p - \alpha_T, \\ \text{TCD} &= \alpha_T - \text{TCV}_g, \end{aligned}$$

where  $\alpha_T$  is the thermal expansion coefficient. The coefficients  $\text{TCV}_p$  and  $\text{TCV}_g$  are in turns obtained from the numerical computation of corresponding velocities.

The velocity change because of temperature is due to the thermal sensitivity of the material. The last is represented through the temperature coefficients of the material parameters and has the following form within a linear approach [41]

$$\begin{aligned} c_{ij}(\tau_0 + \Delta\tau) &= c_{ij}^0(1 + \text{TC}(c_{ij})\Delta\tau), \quad i, j = \overline{1, 6}; \\ e_{ij}(\tau_0 + \Delta\tau) &= e_{ij}^0(1 + \text{TC}(e_{ij})\Delta\tau), \quad i = \overline{1, 3}, j = \overline{1, 6}; \\ \varepsilon_{ij}(\tau_0 + \Delta\tau) &= \varepsilon_{ij}^0(1 + \text{TC}(\varepsilon_{ij})\Delta\tau), \quad i, j = \overline{1, 3}; \\ \rho(\tau_0 + \Delta\tau) &= \rho^0(1 - (\alpha_x + \alpha_y + \alpha_z)\Delta\tau). \end{aligned}$$

Here,  $\alpha_{x,y,z}$  are the thermal expansion coefficients in the corresponding coordinate directions. The values of material temperature coefficients are discovered experimentally and are well known for the majority of materials [42–45]. Thus, the consideration of temperature only requires the change of material parameters and therefore does not bring any extra complications into the mathematical model (2.22), (2.23).

This is not the case if we model the wave propagation in an initially deformed (pre-stressed) solid body. The total deformation can be split into two parts (see fig. 2.5):

- a stationary deformation  $\mathbf{u}_1$  leading from the reference configuration  $\Omega_0$  to the prestressed configuration  $\Omega_1$  and
- time-harmonic deformations  $\mathbf{u}_2(t)$  causing the wave propagation in the prestressed body.

Presuming small deformations we are able to write (2.4) for  $\mathbf{u}(t)$  with respect to the configuration  $\Omega_1$ . However,  $\Omega_1$  is already a deformed state, and the body bears stresses and strains that must be taking into account. For this reason we use here another measure for the stress. Instead of the Cauchy stress tensor  $[\boldsymbol{\sigma}]$ , we write the equilibrium equations for the first Piola-Kirchhoff stress  $[\mathbf{P}]$  [46]. It has a different physical meaning. Namely, it relates the surface forces acting in the deformed configuration to the oriented surface elements in the reference configuration

$$\Delta \mathbf{F}_S = [\mathbf{P}] \mathbf{N} \Delta \Gamma_0, \tag{2.31}$$

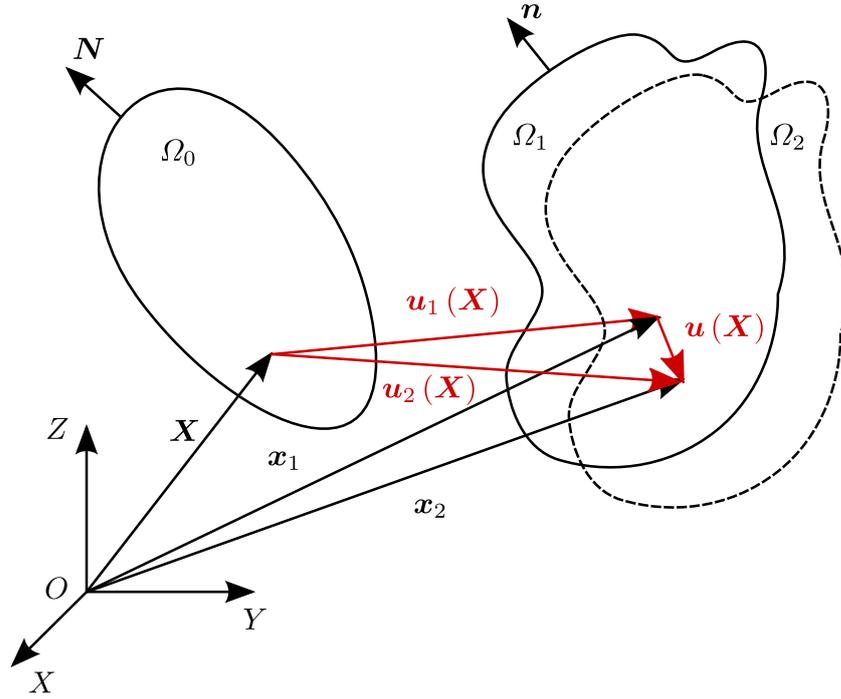


Figure 2.5: To the model for a prestressed body

whereas the Cauchy stress tensor is defined with respect to the deformed configuration (see (2.3)). The link between the Cauchy and the 1<sup>st</sup> Piola-Kirchhoff stress tensors follows from their definitions (2.3), (2.31) and Nanson's formula (2.11), which yields

$$[\boldsymbol{\sigma}] = J^{-1} [\mathbf{P}] [\mathbf{F}]^T. \quad (2.32)$$

The equilibrium equations for the states  $\Omega_1$  and  $\Omega_2$  with respect to the reference configuration  $\Omega_0$  read

$$\nabla_{\mathbf{X}} \cdot [\mathbf{P}_1] = 0, \quad (2.33)$$

$$\nabla_{\mathbf{X}} \cdot [\mathbf{P}_2] = \rho_0 \frac{\partial^2 \mathbf{u}_2}{\partial t^2}. \quad (2.34)$$

Here,  $\rho_0$  is the volume mass density in the reference state.

The tensor  $[\mathbf{P}]$  is non-symmetrical, which is due to the non-symmetry of the deformation gradient  $[\mathbf{F}]$  in (2.32). For this reason it is more convenient to introduce the second Piola-Kirchhoff tensor  $[\mathbf{T}]$  defined as [46]

$$[\mathbf{T}] = [\mathbf{F}]^{-1} [\mathbf{P}] \quad (2.35)$$

Table 2.1: Different measures of stress

	Cauchy	1 <sup>st</sup> Piola-Kirchhoff	2 <sup>nd</sup> Piola-Kirchhoff
Cauchy	$[\boldsymbol{\sigma}]$	$J^{-1} [\mathbf{P}] [\mathbf{F}]^T$	$J^{-1} [\mathbf{F}] [\mathbf{T}] [\mathbf{F}]^T$
1 <sup>st</sup> Piola-Kirchhoff	$J [\boldsymbol{\sigma}] [\mathbf{F}]^{-T}$	$[\mathbf{P}]$	$[\mathbf{F}] [\mathbf{T}]$
2 <sup>nd</sup> Piola-Kirchhoff	$J [\mathbf{F}]^{-1} [\boldsymbol{\sigma}] [\mathbf{F}]^{-T}$	$[\mathbf{F}]^{-1} [\mathbf{P}]$	$[\mathbf{T}]$

and, obviously, symmetrical. The relations between all three measures of the stress are listed in Table 2.1.

Using (2.35) we can re-write (2.33) and (2.34) as

$$\nabla_{\mathbf{X}} \cdot [\mathbf{F}_1] [\mathbf{T}_1] = 0, \quad (2.36)$$

$$\nabla_{\mathbf{X}} \cdot [\mathbf{F}_2] [\mathbf{T}_2] = \rho_0 \frac{\partial^2 \mathbf{u}_2}{\partial t^2}. \quad (2.37)$$

The deformation gradients  $[\mathbf{F}_1]$ ,  $[\mathbf{F}_2]$  mean the deformations from  $\Omega_0$  to the corresponding states

$$[\mathbf{F}_1] = \frac{\partial \mathbf{x}_1}{\partial \mathbf{X}} = \nabla_{\mathbf{X}} \mathbf{u}_1 + [\mathbf{I}], \quad (2.38)$$

$$[\mathbf{F}_2] = \frac{\partial \mathbf{x}_2}{\partial \mathbf{X}} = \nabla_{\mathbf{X}} \mathbf{u}_2 + [\mathbf{I}]. \quad (2.39)$$

The two-step scheme (2.36), (2.37) thoroughly describes the propagation of waves in prestressed elastic solids. In the first step we solve (2.36) in order to extract the data necessary for the next analysis. Then, we seek for a solution of (2.37) taking the results gained from (2.36) into account. Since  $\mathbf{u}_1$  is supposed to be known, (2.36) can be reduced to the computation of the displacement increment  $\mathbf{u} = \mathbf{u}_2 - \mathbf{u}_1$ . This approach was widely used, for example, in the works of Nalamwar [47], Lee [48], Kuang [49, 50], Lematre and Lethiecq [51–53], and many others. Two assumptions have to be mentioned here:

- the effect of the initial stress upon the electric properties of the body is negligible;
- the deformation  $\mathbf{u}$  is small relative to  $\mathbf{u}_1$  and  $\mathbf{u}_2$ .

We multiply (2.37) by a finite test function  $\boldsymbol{\xi}$  and integrate over a domain  $\Delta\Omega_0 \in \Omega_0$ , which yields

$$\int_{\Delta\Omega_0} \nabla_{\mathbf{X}} \cdot [\mathbf{F}_2] [\mathbf{T}_2] \cdot \boldsymbol{\xi} d\Omega = \int_{\Delta\Omega_0} \rho_0 \frac{\partial^2 \mathbf{u}_2}{\partial t^2} \cdot \boldsymbol{\xi} d\Omega. \quad (2.40)$$

Denoting  $[\mathbf{T}_2] = [\mathbf{T}_1] + [\mathbf{T}]$  and integrating the left-hand side of (2.40) by parts with the

use of (2.38), (2.39), we obtain

$$\begin{aligned}
 \int_{\Delta\Omega_0} \nabla_{\mathbf{X}} \cdot [\mathbf{F}_2] [\mathbf{T}_2] \cdot \boldsymbol{\xi} d\Omega &= - \int_{\Delta\Omega_0} [\mathbf{F}_2] [\mathbf{T}_2] : \nabla_{\mathbf{X}} \boldsymbol{\xi} d\Omega + \oint_{\Delta\Gamma_0} ([\mathbf{F}_2] [\mathbf{T}_2])^T \boldsymbol{\xi} \cdot \mathbf{N} d\Gamma \\
 &= - \int_{\Delta\Omega_0} [\mathbf{T}_2] : [\mathbf{F}_2]^T \nabla_{\mathbf{X}} \boldsymbol{\xi} d\Omega + \oint_{\Delta\Gamma_0} [\mathbf{F}_2] [\mathbf{T}_2] \mathbf{N} \cdot \boldsymbol{\xi} d\Gamma \\
 &= - \int_{\Delta\Omega_0} ([\mathbf{T}_1] + [\mathbf{T}]) : ([\mathbf{F}_1] + \nabla_{\mathbf{X}} \mathbf{u})^T \nabla_{\mathbf{X}} \boldsymbol{\xi} d\Omega \\
 &\quad + \oint_{\Delta\Gamma_0} ([\mathbf{F}_1] + \nabla_{\mathbf{X}} \mathbf{u}) ([\mathbf{T}_1] + [\mathbf{T}]) \mathbf{N} \cdot \boldsymbol{\xi} d\Gamma.
 \end{aligned}$$

Here, we have used the following relation

$$[\mathbf{A}] [\mathbf{B}] : [\mathbf{C}] = [\mathbf{B}] : [\mathbf{A}]^T [\mathbf{C}] = [\mathbf{A}] : [\mathbf{C}] [\mathbf{B}]^T. \quad (2.41)$$

Since the deformation  $\mathbf{u}$  and therefore the stress  $[\mathbf{T}]$  are small in comparison to  $\mathbf{u}_1, \mathbf{u}_2$  and  $[\mathbf{T}_1], [\mathbf{T}_2]$ , respectively, we can drop the terms

$$[\mathbf{T}] : \nabla_{\mathbf{X}}^T \mathbf{u} \nabla_{\mathbf{X}} \boldsymbol{\xi} \approx 0 \text{ and } \nabla_{\mathbf{X}} \mathbf{u} [\mathbf{T}] \mathbf{N} \cdot \boldsymbol{\xi} \approx 0.$$

Moreover, from (2.36) we obtain

$$\int_{\Delta\Omega_0} \nabla_{\mathbf{X}} \cdot [\mathbf{F}_1] [\mathbf{T}_1] \cdot \boldsymbol{\xi} d\Omega = - \int_{\Delta\Omega_0} [\mathbf{T}_1] : [\mathbf{F}_1]^T \nabla_{\mathbf{X}} \boldsymbol{\xi} d\Omega + \oint_{\Delta\Gamma_0} [\mathbf{F}_1] [\mathbf{T}_1] \mathbf{N} \cdot \boldsymbol{\xi} d\Gamma = 0.$$

Eventually, we are able to write (2.40) as follows

$$\begin{aligned}
 &- \int_{\Delta\Omega_0} [\mathbf{F}_1] [\mathbf{T}] : \nabla_{\mathbf{X}} \boldsymbol{\xi} d\Omega + \oint_{\Delta\Gamma_0} [\mathbf{F}_1] [\mathbf{T}] \mathbf{N} \cdot \boldsymbol{\xi} d\Gamma \\
 &- \int_{\Delta\Omega_0} \nabla_{\mathbf{X}} \mathbf{u} [\mathbf{T}_1] : \nabla_{\mathbf{X}} \boldsymbol{\xi} d\Omega + \oint_{\Delta\Gamma_0} \nabla_{\mathbf{X}} \mathbf{u} [\mathbf{T}] \mathbf{N} \cdot \boldsymbol{\xi} d\Gamma = \int_{\Delta\Omega_0} \rho_0 \frac{\partial^2 \mathbf{u}_2}{\partial t^2} \cdot \boldsymbol{\xi} d\Omega,
 \end{aligned} \quad (2.42)$$

The differential form of (2.42) reads

$$\nabla_{\mathbf{X}} \cdot ([\mathbf{F}_1] [\mathbf{T}] + \nabla_{\mathbf{X}} \mathbf{u} [\mathbf{T}_1]) = \rho_0 \frac{\partial^2 \mathbf{u}_2}{\partial t^2} \quad (2.43)$$

and describes the propagation of waves in initially prestressed structures with respect to the reference state  $\Omega_0$ .

Recollecting (2.10), (2.11) and applying the chain rule

$$\nabla_{\mathbf{X}} \boldsymbol{\xi} = \left\{ \frac{\partial \xi_i}{\partial X_j} \right\} = \left\{ \sum_k \frac{\partial \xi_i}{\partial x_k} \frac{\partial x_k}{\partial X_j} \right\} = \nabla_{\mathbf{x}} \boldsymbol{\xi} [\mathbf{F}], \quad (2.44)$$

we can proceed from (2.42) to a form related to the prestressed state. Indeed,

$$\begin{aligned}
 \int_{\Delta\Omega_0} [\mathbf{F}_1] [\mathbf{T}] : \nabla_{\mathbf{X}} \boldsymbol{\xi} d\Omega &= \int_{\Delta\Omega_1} J^{-1} [\mathbf{F}_1] [\mathbf{T}] : \nabla_{\mathbf{x}_1} \boldsymbol{\xi} [\mathbf{F}_1] d\Omega \\
 &\stackrel{(2.41)}{=} \int_{\Delta\Omega_1} J^{-1} [\mathbf{F}_1] [\mathbf{T}] [\mathbf{F}_1]^T : \nabla_{\mathbf{x}_1} \boldsymbol{\xi} d\Omega = \int_{\Delta\Omega_1} [\boldsymbol{\sigma}] : \nabla_{\mathbf{x}_1} \boldsymbol{\xi} d\Omega; \\
 \oint_{\Delta\Gamma_0} [\mathbf{F}_1] [\mathbf{T}] \mathbf{N} \cdot \boldsymbol{\xi} d\Gamma &= \oint_{\Delta\Gamma_1} J^{-1} [\mathbf{F}_1] [\mathbf{T}] [\mathbf{F}_1]^T \mathbf{n}_1 \cdot \boldsymbol{\xi} d\Gamma = \oint_{\Delta\Gamma_1} [\boldsymbol{\sigma}] \mathbf{n} \cdot \boldsymbol{\xi} d\Gamma; \\
 \int_{\Delta\Omega_0} \nabla_{\mathbf{X}} \mathbf{u} [\mathbf{T}_1] : \nabla_{\mathbf{X}} \boldsymbol{\xi} d\Omega &= \int_{\Delta\Omega_1} J^{-1} \nabla_{\mathbf{x}_1} \mathbf{u} [\mathbf{F}_1] [\mathbf{T}_1] : \nabla_{\mathbf{x}_1} \boldsymbol{\xi} [\mathbf{F}_1] d\Omega \\
 &\stackrel{(2.41)}{=} \int_{\Delta\Omega_1} J^{-1} \nabla_{\mathbf{x}_1} \mathbf{u} [\mathbf{F}_1] [\mathbf{T}_1] [\mathbf{F}_1]^T : \nabla_{\mathbf{x}_1} \boldsymbol{\xi} d\Omega \\
 &= \int_{\Delta\Omega_1} \nabla_{\mathbf{x}_1} \mathbf{u} [\boldsymbol{\sigma}_1] : \nabla_{\mathbf{x}_1} \boldsymbol{\xi} d\Omega; \\
 \oint_{\Delta\Gamma_0} \nabla_{\mathbf{X}} \mathbf{u} [\mathbf{T}] \mathbf{N} \cdot \boldsymbol{\xi} d\Gamma &= \oint_{\Delta\Gamma_1} J^{-1} \nabla_{\mathbf{x}_1} \mathbf{u} [\mathbf{F}_1] [\mathbf{T}] [\mathbf{F}_1]^T \mathbf{n}_1 \cdot \boldsymbol{\xi} d\Gamma \\
 &= \oint_{\Delta\Gamma_1} \nabla_{\mathbf{x}_1} \mathbf{u} [\boldsymbol{\sigma}_1] \mathbf{n}_1 \cdot \boldsymbol{\xi} d\Gamma; \\
 \int_{\Delta\Omega_0} \rho_0 \frac{\partial^2 \mathbf{u}_2}{\partial t^2} \cdot \boldsymbol{\xi} d\Omega &= \int_{\Delta\Omega_1} J^{-1} \rho_0 \frac{\partial^2 \mathbf{u}_2}{\partial t^2} \cdot \boldsymbol{\xi} d\Omega = \int_{\Delta\Omega_1} \rho_1 \frac{\partial^2 \mathbf{u}_2}{\partial t^2} \cdot \boldsymbol{\xi} d\Omega.
 \end{aligned}$$

Taking into account that  $\mathbf{u}_1$  is independent of time and therefore

$$\frac{\partial^2 \mathbf{u}_2}{\partial t^2} = \frac{\partial^2 \mathbf{u}}{\partial t^2},$$

we finally arrive at the equation

$$\nabla_{\mathbf{x}_1} \cdot ([\boldsymbol{\sigma}] + \nabla_{\mathbf{x}_1} \mathbf{u} [\boldsymbol{\sigma}_1]) = \rho_1 \frac{\partial^2 \mathbf{u}}{\partial t^2} \quad (2.45)$$

which instead of (2.43) is related to the prestressed state  $\Omega_1$ . With (2.45) the full system of piezoelectric PDEs reads

$$\nabla_{\mathbf{x}_1} \cdot ([\boldsymbol{\sigma}] + \nabla_{\mathbf{x}_1} \mathbf{u} [\boldsymbol{\sigma}_1]) = \rho_1 \frac{\partial^2 \mathbf{u}}{\partial t^2}, \quad (2.46)$$

$$\nabla_{\mathbf{x}_1} \cdot \mathbf{D} = 0. \quad (2.47)$$

The mechanical stress  $[\boldsymbol{\sigma}]$  and the electric displacement  $\mathbf{D}$  still fulfil the constitutive equations (2.20), (2.21) with the difference that the tensor  $[\mathbf{c}^E]$  must now reflect the initial deformation. For this reason we use the tensor of effective elastic moduli  $[\tilde{\mathbf{c}}^E]$

which depends on the strain  $[\mathbf{S}_1]$  [47]

$$\tilde{c}_{ij} = c_{ij} + \sum_{k=1}^6 c_{ijk} S_{1;k}, \quad i, j = \overline{1, 6}, \quad (2.48)$$

where  $c_{ijk}$  are the third order elastic constants [54]. These constants are known for a large number of materials [55, 56], which makes it possible to use the developed model for practical applications.

---

### Numerical model of wave propagation and FE-formulation

---

#### 3.1 Finite element model of piezoelectric substrate with periodic electrode grating

In this part we shall proceed to the numerical modelling of a SAW device. Though the analysis of a piezoelectric half-space given in section 2.3 can provide us with some valuable facts about the propagation of SAW in piezoelectric materials, for real devices, where a metal electrode grating is applied to a piezoelectric substrate, we can hardly get the necessary information without taking the complexity of the structure into account. Speaking about the complexity we bear in mind the following:

- the shape and the mass of the electrodes;
- position of the grating relative to the substrate, i.e. whether it is located directly on the top of the substrate or lifted above/buried into it;
- the structure of the substrate, i.e. whether the substrate contains one or more than one layers.

This implies using numerical modelling in order to simulate the behaviour of the device.

We concern ourselves with the modelling of an IDT as a principal part of a SAW device. It consists of a piezoelectric substrate and an electrode grating applied to the substrate's top (see fig. 3.1). Before we proceed to the mathematical model of an IDT, we should mention the fact that for many industrial applications IDTs are designed to have hundreds of electrodes (fingers) [3]. When the fingers of the IDT are put together in a periodic manner (see fig. 3.2), the simulation of the whole structure can be reduced to the simulation of a unit cell. Making such a reduction, we imply that the substrate

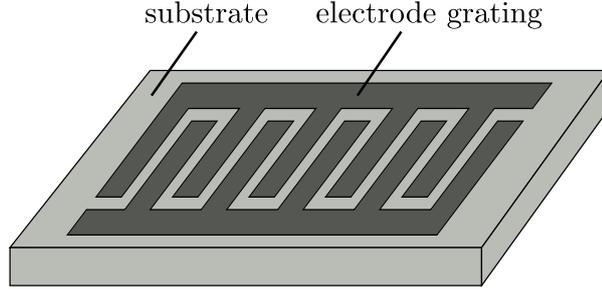


Figure 3.1: Schematic picture of an IDT

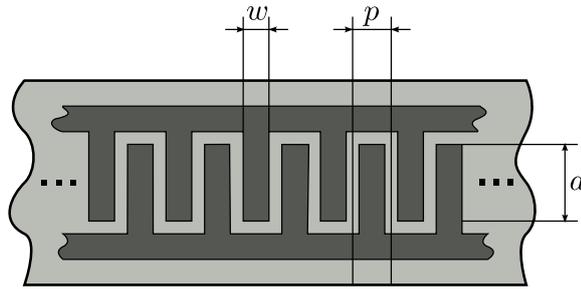


Figure 3.2: Approximation of the IDT as a structure with a periodic electrode grating

is homogeneous in the direction of propagation. This sufficiently shrinks the computational time and makes it possible to use particular procedures relevant to the analysis of periodic structures which will be discussed later. The sketch in fig. 3.2 depicts an approximation of a single-electrode transducer with an infinite number of fingers. The wavelength in such an IDT is equal to doubled pitch  $\lambda = 2p$ . The pitch  $p$  and the width  $w$  of the electrodes define together the metallisation ratio  $\eta = w/p$ . The aperture  $a$  is usually chosen from 10 to 100 of  $\lambda$  [2, 57], which enables us to make further simplifications. Though the single-electrode transducer is not the only possible configuration [1, 26], we stick to this one developing the mathematical model.

We introduce the Cartesian coordinate system as shown in fig. 3.3. Namely, the  $x$ -axes point to the direction of wave propagation, i.e. along the grating; the  $y$ -axis is parallel to the aperture; the  $z$ -axis is orthogonal to the substrate. We denote the area of the unit cell by

$$\Omega = \Omega_{\text{sub}} \cup \Omega_{\text{ele}} \cup \Omega_{\text{air}}.$$

The coupling between the electrostatic and the mechanical fields in  $\Omega$  is described by the system of partial differential equations (2.22), (2.23). We presume the absence of external forces  $\mathbf{f}_V = 0$  and free volume charges  $\varrho_e = 0$  and a harmonic dependence on time with the angular frequency  $\omega$ , so that

$$\frac{\partial^2 \mathbf{u}}{\partial t^2} = -\omega^2 \mathbf{u}.$$

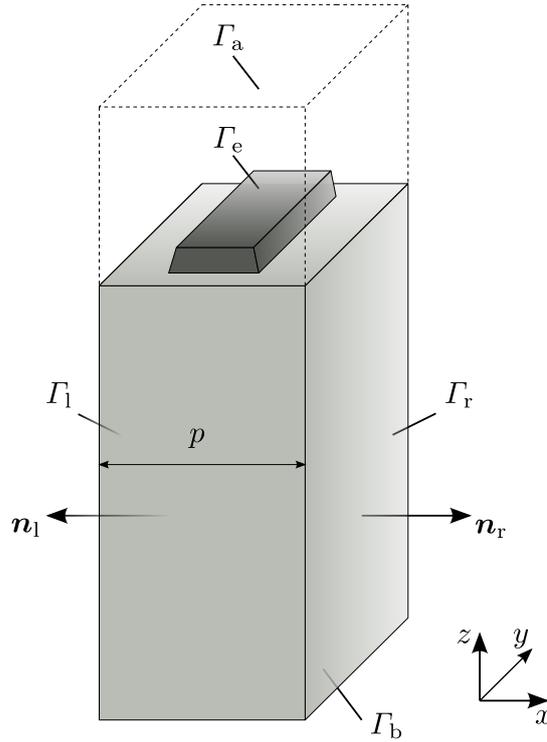


Figure 3.3: A unit cell of the IDT with a periodic electrode grating

Therefore, we obtain

$$\mathcal{B}^T \left( [\mathbf{c}^E] \mathcal{B} \mathbf{u} + [\mathbf{e}]^T \nabla \varphi \right) + \omega^2 \rho \mathbf{u} = 0 \text{ in } \Omega, \quad (3.1)$$

$$\nabla \cdot \left( [\mathbf{e}] \mathbf{u} - [\boldsymbol{\varepsilon}^S] \nabla \varphi \right) = 0 \text{ in } \Omega, \quad (3.2)$$

where  $\mathbf{u}$  and  $\varphi$  act as the complex amplitudes of displacement and scalar electric potential. The system (3.1), (3.2) is split into two independent equations if the material does not show piezoelectric properties, because  $[\mathbf{e}] = 0$ . Within the electrodes,  $\varphi = 0$ , and therefore only mechanical field is to be computed from the equation (3.1). On the contrary, only electric field exists in the air surrounding the device, and (3.1) can be stricken out. In case of a prestressed material an extra term is to be added to the equation (3.1) such that it gets the following form

$$\nabla \cdot (\nabla \mathbf{u} [\boldsymbol{\sigma}_1]) + \mathcal{B}^T \left( [\mathbf{c}^E] \mathcal{B} \mathbf{u} + [\mathbf{e}]^T \nabla \varphi \right) + \omega^2 \rho_1 \mathbf{u} = 0 \text{ in } \Omega.$$

For the sake of brevity we do not carry this term through the further expressions.

We impose the following boundary conditions that complement the system (3.1), (3.2):

- the structure is fixed at the bottom

$$\mathbf{u} = \mathbf{0} \text{ on } \Gamma_b, \quad (3.3)$$

- other surfaces are free of stress

$$[\boldsymbol{\sigma}] \mathbf{n} = \mathbf{0} \text{ on } \Gamma_{\Omega \setminus \Omega_{\text{air}}} \setminus \Gamma_b, \quad (3.4)$$

- the electric field is given by a harmonic driving voltage of the amplitude  $V$ ; therefore,

$$\varphi = V \text{ on } \Gamma_e, \quad (3.5)$$

- the electric potential  $\varphi(\mathbf{x})$  vanishes in the air as  $\mathbf{x} \rightarrow \infty$  so that, approximately,

$$\varphi = 0 \text{ on some artificial boundary } \Gamma_a. \quad (3.6)$$

The boundary value problem (3.1)–(3.6) is still incomplete, for it lacks boundary conditions on  $\Gamma_l$  and  $\Gamma_r$ . To that end, we refer to Floquet’s theorem [58] (also known as Floquet-Lyapunov theorem). It asserts that if  $\psi(x)$  is a fundamental solution of an ordinary differential equation  $f'_x(x) = A(x)f(x)$  with a periodic function  $A(x+p) = A(x)$ , then

$$\psi(x) = \psi_p(x) e^{xB}. \quad (3.7)$$

In (3.7),  $\psi_p(x+p) = \psi_p(x)$  and  $e^{pB} = \psi(p)\psi^{-1}(0)$ . Bloch has proven that similar results are valid for the stationary Schrödinger equation with a periodic potential function (Bloch’s theorem [58]) in  $n$ -dimensional space, i.e. it has a non-trivial solution of the form

$$\psi(\mathbf{x}) = \psi_p(\mathbf{x}) e^{i\mathbf{x}\mathbf{k}}, \quad (3.8)$$

where  $\psi_p(\mathbf{x})$  is a periodic function. Finally, Kouchment in his work [59] extended Floquet’s theory to the partial differential equations of parabolic and elliptic types. Eventually, we can write by analogy with (3.8)

$$\mathbf{u}|_{\Gamma_r} = \vartheta \mathbf{u}|_{\Gamma_l}, \quad \varphi|_{\Gamma_r} = \vartheta \varphi|_{\Gamma_l}; \quad (3.9)$$

$$[\boldsymbol{\sigma}] \mathbf{n}_r|_{\Gamma_r} = -\vartheta [\boldsymbol{\sigma}] \mathbf{n}_l|_{\Gamma_l}, \quad \mathbf{D}\mathbf{n}_l|_{\Gamma_r} = -\vartheta \mathbf{D}\mathbf{n}_r|_{\Gamma_l}. \quad (3.10)$$

We shall refer (3.9) and (3.10) as Bloch-periodic boundary conditions.

The boundary value problem (3.1)–(3.6) is now completed by the boundary conditions (3.9), (3.10), and we are able to proceed to its weak formulation. Let  $\mathbf{u}'$  and  $\varphi'$  be appropriate test functions. Following the standard procedure [35] we multiply (3.1) and (3.2) by  $\mathbf{u}'$  and  $\varphi'$  and integrate over  $\Omega$  by parts. This yields

$$\int_{\Omega} (\mathcal{B}\mathbf{u}')^T [\mathbf{c}^E] \mathcal{B}\mathbf{u} d\Omega + \int_{\Omega} (\mathcal{B}\mathbf{u}')^T [\mathbf{e}]^T \nabla \varphi d\Omega - \omega^2 \int_{\Omega} \rho (\mathbf{u}')^T \mathbf{u} d\Omega$$

$$- \int_{\Gamma_1} (\mathbf{u}')^T [\boldsymbol{\sigma}] \mathbf{n}_1 d\Gamma - \int_{\Gamma_r} (\mathbf{u}')^T [\boldsymbol{\sigma}] \mathbf{n}_r d\Gamma = 0, \quad (3.11)$$

$$\begin{aligned} \int_{\Omega} (\nabla \varphi')^T [\mathbf{e}] \mathcal{B} \mathbf{u} d\Omega - \int_{\Omega} (\nabla \varphi')^T [\boldsymbol{\varepsilon}^S] \nabla \varphi d\Omega \\ - \int_{\Gamma_1} \varphi' D_{n_1} d\Gamma - \int_{\Gamma_r} \varphi' D_{n_r} d\Gamma = 0 \end{aligned} \quad (3.12)$$

with  $[\boldsymbol{\sigma}]$  and  $\mathbf{D}$  defined according to (2.20) and (2.21) respectively.

The system (3.9), (3.10) can be rewritten in a brief form such that

$$\int_{\Omega} (\mathcal{D} \mathbf{w}')^T [\mathbf{C}] \mathcal{D} \mathbf{w} d\Omega - \omega^2 \int_{\Omega} (\mathbf{w}')^T [\boldsymbol{\rho}] \mathbf{w} d\Omega - \int_{\Gamma_1} (\mathbf{w}')^T \mathbf{T}|_{\Gamma_1} d\Gamma - \int_{\Gamma_r} (\mathbf{w}')^T \mathbf{T}|_{\Gamma_r} d\Gamma = 0. \quad (3.13)$$

Here,

$$\mathcal{D} \mathbf{w} = \begin{pmatrix} \mathcal{B} & 0 \\ 0 & \nabla \end{pmatrix} \begin{pmatrix} \mathbf{u} \\ \varphi \end{pmatrix}, \quad [\mathbf{C}] = \begin{pmatrix} [\mathbf{c}^E] & [\mathbf{e}]^T \\ [\mathbf{e}] & -[\boldsymbol{\varepsilon}^S] \end{pmatrix}, \quad [\boldsymbol{\rho}] = \begin{pmatrix} \rho & 0 & 0 & 0 \\ 0 & \rho & 0 & 0 \\ 0 & 0 & \rho & 0 \\ 0 & 0 & 0 & 0 \end{pmatrix}, \quad \mathbf{T} = \begin{pmatrix} [\boldsymbol{\sigma}] \mathbf{n} \\ D_n \end{pmatrix}.$$

The boundary conditions (3.9), (3.10) then read

$$\mathbf{w}|_{\Gamma_r} = \vartheta \mathbf{w}|_{\Gamma_1}, \quad \mathbf{T}|_{\Gamma_r} = -\vartheta \mathbf{T}|_{\Gamma_1}. \quad (3.14)$$

Let  $\Omega^h = \cup_{i=1}^{n_e} \Omega^{(i)}$  be a mesh of  $\Omega$ , and  $\mathcal{N}(\Omega^h) = \{\mathbf{M}_1, \mathbf{M}_2, \dots, \mathbf{M}_{n_n}\}$  be the set of nodes of  $\Omega^h$ . We approximate the unknown  $\mathbf{w}$  on  $\Omega^h$  as

$$\begin{aligned} \mathbf{w}(\mathbf{x}) \simeq \mathbf{w}^h(\mathbf{x}) &= \sum_{k=1}^{n_n} \mathbf{N}_k(\mathbf{x}) \mathbf{w}_k, \quad \mathbf{x} \in \Omega; \\ \mathbf{N}_k &= \begin{pmatrix} N_k & 0 & 0 & 0 \\ 0 & N_k & 0 & 0 \\ 0 & 0 & N_k & 0 \\ 0 & 0 & 0 & N_k \end{pmatrix}, \quad \mathbf{w}_k = \begin{pmatrix} u_{x,k} \\ u_{y,k} \\ u_{z,k} \\ \varphi_k \end{pmatrix}; \end{aligned} \quad (3.15)$$

where  $N_k$  is an interpolation (FE basis) function, and  $n_n$  is the number of nodes in  $\Omega^h$ . In order to be consistent with (3.13), the basis functions have to be continuous and at least piecewise continuously differentiable on  $\Omega^h$ . If basis functions are chosen in such a way that for each  $\mathbf{M}_j \in \mathcal{N}(\Omega^h)$

$$N_k(\mathbf{M}_j) = \begin{cases} 1, & j = k, \\ 0, & j \neq k, \end{cases}$$

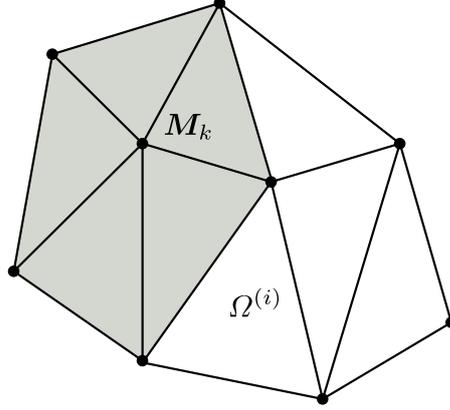


Figure 3.4: To the definition of basis functions

it follows that  $\mathbf{w}(\mathbf{x}) \simeq \mathbf{w}^h(\mathbf{x}) = \mathbf{w}_k$  if  $\mathbf{x} = \mathbf{M}_k$ . As a rule, basis functions used within the FEM routine are built to have a local support. This means that the function  $N_k$  is non-zero only on the elements  $\Omega^{(i)}$  having the node  $\mathbf{M}_k$  in common (see the shaded elements in fig. 3.4). The procedures of constructing appropriate basis functions for various element types are given in details in [35].

Substituting (3.15) for  $\mathbf{w}$  and  $\mathbf{w}'$  in (3.13), we obtain

$$\sum_{k=1}^{n_n} \mathbf{w}_k \left( \int_{\Omega} (\mathcal{D}\mathbf{N}_j)^T [\mathbf{C}] \mathcal{D}\mathbf{N}_k d\Omega - \omega^2 \int_{\Omega} (\mathbf{N}_j)^T [\boldsymbol{\rho}] \mathbf{N}_k d\Omega \right) - \int_{\Gamma_1} (\mathbf{N}_j)^T \mathbf{T}|_{\Gamma_1} d\Gamma - \int_{\Gamma_r} (\mathbf{N}_j)^T \mathbf{T}|_{\Gamma_r} d\Gamma = 0, \quad j = \overline{1, n_n}. \quad (3.16)$$

Owing to the additivity of integrals, we can rewrite an integral over  $\Omega$  according to the following rule

$$\int_{\Omega} \dots \simeq \int_{\Omega^h} \dots = \sum_{i=1}^{n_e} \int_{\Omega^{(i)}} \dots$$

and therefore

$$\int_{\Omega} (\mathcal{D}\mathbf{N}_j)^T [\mathbf{C}] \mathcal{D}\mathbf{N}_k d\Omega \simeq \sum_{i=1}^{n_e} \int_{\Omega^{(i)}} (\mathcal{D}\mathbf{N}_j)^T [\mathbf{C}] \mathcal{D}\mathbf{N}_k d\Omega, \quad (3.17)$$

$$\int_{\Omega} (\mathbf{N}_j)^T [\boldsymbol{\rho}] \mathbf{N}_k d\Omega \simeq \sum_{i=1}^{n_e} \int_{\Omega^{(i)}} (\mathbf{N}_j)^T [\boldsymbol{\rho}] \mathbf{N}_k d\Omega. \quad (3.18)$$

If a basis function  $N_j = 0$  in  $\Omega^{(i)}$ , then  $\forall k$

$$\int_{\Omega^{(i)}} (\mathbf{N}_j)^T [\boldsymbol{\rho}] \mathbf{N}_k d\Omega = \int_{\Omega^{(i)}} (\mathcal{D}\mathbf{N}_j)^T [\mathbf{C}] \mathcal{D}\mathbf{N}_k d\Omega = 0.$$

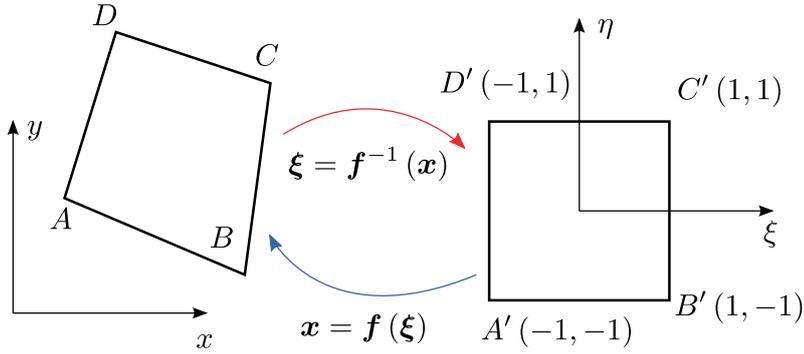


Figure 3.5: To the evaluation of integrals

Gaussian quadrature rules [60] are used for numerical evaluation of the integrals in (3.17), (3.18). This procedure requires that the element  $\Omega^{(i)}$  be preliminarily transformed to a reference element  $\Omega^e$  [35]. If, for example,  $\Omega^{(i)}$  is a quadrilateral in 2D, its reference element will be a square  $[-1, 1] \times [-1, 1]$  (see fig. 3.5). For the integrals containing the product of the basis functions we thus obtain

$$\int_{\Omega^{(i)}} N_j(\mathbf{x}) N_k(\mathbf{x}) d\Omega = \int_{\Omega^e} N_j(\boldsymbol{\xi}) N_k(\boldsymbol{\xi}) J^e d\Omega,$$

where  $J^e = \left| \det \left( \frac{\partial \mathbf{f}}{\partial \boldsymbol{\xi}} \right) \right| = |\det [\mathbf{F}]|$ . For the integrals containing the derivatives one finds that

$$\int_{\Omega^{(i)}} \nabla_{\mathbf{x}} N_j(\mathbf{x}) \cdot \nabla_{\mathbf{x}} N_k(\mathbf{x}) d\Omega = \int_{\Omega^e} [\mathbf{F}]^{-T} \nabla_{\boldsymbol{\xi}} N_j(\boldsymbol{\xi}) \cdot [\mathbf{F}]^{-T} \nabla_{\boldsymbol{\xi}} N_k(\boldsymbol{\xi}) J^e d\Omega,$$

The integrals over the reference elements are then easy to evaluate. Indeed, for a quadrilateral element it follows that

$$\int_{\Omega^e} f(\boldsymbol{\xi}) d\Omega = \int_{-1}^1 \int_{-1}^1 f(\xi, \eta) d\eta d\xi.$$

The incorporation of the periodic boundary conditions into the finite element model (3.16) requires a special treatment. Therefore, we shall discuss this issue in a separate section.

## 3.2 Boundary element method and absorbing boundary conditions

Although the problem of wave propagation is already solvable through the model developed in the previous section, provided that we have properly incorporated the periodic boundary conditions, such a direct way will bring large computational costs. This is due to the thickness of the substrate which is usually much greater than the wavelength [26]. Therefore, the consideration of the whole substrate is in many cases unnecessary, for

example, in case of a Rayleigh wave which penetrates the depth up to 2 wavelength into the substrates. Neglecting the reflections from  $\Gamma_b$ , we are able to treat the substrate as an infinite half-space  $z < 0$ . It allows us to utilise certain techniques and significantly reduce the computational time.

First, we focus on the boundary element method. The idea of the method is to find a boundary integral representation of the solution of a partial differential equation. This is done by means of the Green's function of the corresponding differential operator. Let  $\Omega \subset \mathbb{R}^3$  and  $\mathfrak{G}$  be the Green's function of the differential operator  $\mathcal{L}_x$ . Then it satisfies the equation [61]

$$\mathcal{L}_x \mathfrak{G}(\mathbf{x}, \boldsymbol{\xi}) = \delta(\mathbf{x} - \boldsymbol{\xi}), \quad \mathbf{x}, \boldsymbol{\xi} \in \Omega,$$

where  $\delta(\mathbf{x} - \boldsymbol{\xi})$  is the Dirac delta function. Once the Green's function is known, we obtain the solution of the inhomogeneous equation  $\mathcal{L}_x \varphi(\mathbf{x}) = f(\mathbf{x})$ ,  $\mathbf{x} \in \Omega$  through the following representation

$$\varphi(\mathbf{x}) = \int_{\Omega} f(\boldsymbol{\xi}) \mathfrak{G}(\mathbf{x}, \boldsymbol{\xi}) d\Omega_{\boldsymbol{\xi}}, \quad \mathbf{x} \in \Omega.$$

Indeed,

$$\mathcal{L}_x \varphi(\mathbf{x}) = \mathcal{L}_x \int_{\Omega} f(\boldsymbol{\xi}) \mathfrak{G}(\mathbf{x}, \boldsymbol{\xi}) d\Omega_{\boldsymbol{\xi}} = \int_{\Omega} f(\boldsymbol{\xi}) \delta(\mathbf{x} - \boldsymbol{\xi}) d\Omega_{\boldsymbol{\xi}} = f(\mathbf{x}), \quad \mathbf{x} \in \Omega.$$

Let  $\mathcal{L} = -\Delta$ , then we get the Poisson equation  $-\Delta \varphi(\mathbf{x}) = f(\mathbf{x})$ ,  $\mathbf{x} \in \Omega$ . The Green's function for the Laplace operator in 3D space reads [62]

$$\mathfrak{G}(\mathbf{x}, \boldsymbol{\xi}) = \frac{1}{4\pi} \frac{1}{|\mathbf{x} - \boldsymbol{\xi}|}.$$

Let  $\Delta \varphi(\mathbf{x}) = 0$ ,  $\mathbf{x} \notin \Omega$ . Then we obtain the following well-known representation of  $\varphi$  through the volume potential [62]

$$\begin{aligned} \varphi(\mathbf{x}) &= \int_{\mathbb{R}^3} \varphi(\boldsymbol{\xi}) \delta(\mathbf{x} - \boldsymbol{\xi}) d\Omega_{\boldsymbol{\xi}} = - \int_{\Omega} \varphi(\boldsymbol{\xi}) \Delta_{\boldsymbol{\xi}} \mathfrak{G}(\mathbf{x}, \boldsymbol{\xi}) d\Omega_{\boldsymbol{\xi}} \\ &- \int_{\mathbb{R}^3 \setminus \Omega} \varphi(\boldsymbol{\xi}) \Delta_{\boldsymbol{\xi}} \mathfrak{G}(\mathbf{x}, \boldsymbol{\xi}) d\Omega_{\boldsymbol{\xi}} = - \int_{\Omega} \Delta \varphi(\boldsymbol{\xi}) \mathfrak{G}(\mathbf{x}, \boldsymbol{\xi}) d\Omega_{\boldsymbol{\xi}} \\ &- \int_{\mathbb{R}^3 \setminus \Omega} \Delta \varphi(\boldsymbol{\xi}) \mathfrak{G}(\mathbf{x}, \boldsymbol{\xi}) d\Omega_{\boldsymbol{\xi}} = \frac{1}{4\pi} \int_{\Omega} \frac{f(\boldsymbol{\xi})}{|\mathbf{x} - \boldsymbol{\xi}|} d\Omega_{\boldsymbol{\xi}}, \quad \mathbf{x} \in \mathbb{R}^3, \end{aligned} \quad (3.19)$$

where the first Green's formula has been used [63].

If boundary conditions are given on  $\Gamma = \partial\Omega$ , the explicit form of the Green's function is not obvious. Suppose

$$-\Delta \varphi(\mathbf{x}) = f(\mathbf{x}), \quad \mathbf{x} \in \Omega,$$

$$\varphi(\mathbf{x}) = h(\mathbf{x}), \mathbf{x} \in \Gamma.$$

Define the Green's function as a solution of the following boundary value problem for an arbitrary  $\mathbf{x} \in \Omega$

$$-\Delta_{\xi} \mathfrak{G}(\mathbf{x}, \xi) = \delta(\mathbf{x} - \xi), \xi \in \Omega, \quad (3.20)$$

$$\mathfrak{G}(\mathbf{x}, \xi) = 0, \xi \in \Gamma. \quad (3.21)$$

Then, working in the same way as in (3.19), we obtain

$$\varphi(\mathbf{x}) = \int_{\Omega} f(\xi) \mathfrak{G}(\mathbf{x}, \xi) d\Omega_{\xi} + \oint_{\Gamma} h(\xi) \frac{\partial \mathfrak{G}}{\partial n}(\mathbf{x}, \xi) d\Gamma_{\xi}, \mathbf{x} \in \Omega.$$

Thus, the desired integral representation of the solution of the boundary value problem through the Green's function is obtained. The issue is henceforth to gain the Green's function, i.e., for the example above, to solve the boundary value problem (3.20), (3.21). Obviously, it can be a very sophisticated task to derive the Green's function explicitly in an arbitrary domain  $\Omega$  even for the Laplace operator [62]. If it is possible to split the domain  $\Omega = \Omega_1 \cup \Omega_2$  such that an explicit form of the Green's function is known for  $\Omega_2$ , one can solve the given boundary value problem using FEM in  $\Omega_1$  and integral representation through the Green's function in  $\Omega_2$ . Such a technique is called FEM/BEM coupling.

Now, let us turn to the system of PDEs (3.1), (3.2) and see how the concepts of the Green's function and FEM/BEM approach can be used here. Suppose that the substrate is homogeneous and semi-infinite, i.e. it occupies the lower half-space  $z < 0$ . Let the driving voltage be applied to an infinitely long periodic electrode grating placed on the top of the substrate. Then we are able to use the FEM/BEM approach in the following way:

- BEM is used to model the piezoelectric half-space,
- FEM takes the influence of the electrodes into account.

For the sake of simplicity assume that  $\mathbf{u}$  and  $\varphi$  are independent of the  $y$ -coordinate and consider the problem (3.1), (3.2) for a unit cell in 2D  $-p/2 \leq x \leq p/2$  as shown in fig. 3.6. We recount here the approach first given in [17] and since then used in the number of works [18, 30, 64].

Suppose we are in possession of the following relation

$$\begin{pmatrix} \mathbf{u}(x) \\ \varphi(x) \end{pmatrix} = \int_{\Gamma_{\text{int}}} \mathfrak{G}_{\text{p}}(x - \xi) \begin{pmatrix} \sigma_z(\xi) \\ q_e(\xi) \end{pmatrix} d\xi, \quad -p/2 \leq x \leq p/2. \quad (3.22)$$

Here,  $\sigma_z$  is the normal to the surface  $z = 0$  component of the stress, and  $q_e$  is the surface density of the electric charge on  $\Gamma_{\text{int}}$  which is the interface between the electrode and the

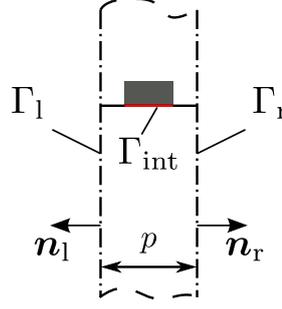


Figure 3.6: To the periodic Green's function definition

substrate. The periodic Green's function  $\mathfrak{G}_p$  can be represented as a matrix operator containing mechanical, electric, and coupling parts

$$\mathfrak{G}_p = \begin{pmatrix} \mathfrak{G}_m & \mathfrak{G}_c^T \\ \mathfrak{G}_c & \mathfrak{G}_e \end{pmatrix}$$

There is no electric field within the electrode  $\Omega_{\text{ele}}$ , and the distribution of the mechanical field can be modelled by means of FEM, so that (3.11) reads

$$\int_{\Omega_{\text{ele}}} (\mathcal{B}\mathbf{u}')^T [\mathbf{c}^E] \mathcal{B}\mathbf{u} d\Omega - \omega^2 \int_{\Omega_{\text{ele}}} \rho (\mathbf{u}')^T \mathbf{u} d\Omega + \int_{\Gamma_{\text{int}}} (\mathbf{u}')^T \boldsymbol{\sigma}_z d\Gamma = 0. \quad (3.23)$$

Setting  $x$  to  $\Gamma_{\text{int}}$  in (3.22) and multiplying it by test functions  $\boldsymbol{\sigma}'_z, q'$ , we obtain

$$\begin{aligned} \int_{\Gamma_{\text{int}}} (\boldsymbol{\sigma}'_z)^T \mathbf{u} dx &= \int_{\Gamma_{\text{int}}} (\boldsymbol{\sigma}'_z)^T \int_{\Gamma_{\text{int}}} \left( \tilde{\mathfrak{G}}_m(\xi - x) + \tilde{\mathfrak{G}}_c^T(\xi - x) \right) \boldsymbol{\sigma}_z(\xi) d\xi dx, \\ \int_{\Gamma_{\text{int}}} q' \varphi dx &= \int_{\Gamma_{\text{int}}} q'(x) \int_{\Gamma_{\text{int}}} \left( \tilde{\mathfrak{G}}_c(\xi - x) + \tilde{\mathfrak{G}}_e(\xi - x) \right) q_e(\xi) d\xi dx. \end{aligned} \quad (3.24)$$

The potential  $\varphi$  is constant on  $\Gamma_{\text{int}}$  and supposed to be given through the driving voltage.

In order to get the numerical model of FEM/BEM, we need to approximate the unknowns

$$\begin{aligned} \mathbf{u}(x, z) &\simeq \mathbf{u}_h(x, z) = \sum_i \mathbf{N}_i(x, z) \mathbf{u}^{(i)}, \quad (x, z) \in \Omega_{\text{ele}}, \\ \boldsymbol{\sigma}_z(x, z) &\simeq \boldsymbol{\sigma}_{zh}(x) = \sum_j \mathbf{P}_j(x) \boldsymbol{\sigma}_z^{(j)}, \quad x \in \Gamma_{\text{int}}, \\ q_e(x, z) &\simeq q_{eh}(x) = \sum_j P_j(x) q_e^{(j)}, \quad x \in \Gamma_{\text{int}}; \end{aligned}$$

substitute them for  $\mathbf{u}$ ,  $\boldsymbol{\sigma}_z$ , and  $q_e$  in (3.23), (3.24); and use the basis functions instead of the corresponding test functions. The numerical model (3.23), (3.24) ensures a very high precision of the computations if the basis functions approximating  $q_e$  take into account

the asymptotic behaviour of the charge density near the edges of the electrodes [65]. Such basis functions were suggested in the work [18] and have been widely used [66–68] since then.

The derivation of the Green's function  $\mathfrak{G}_p$  is a separate task. We shall follow the way proposed by Peach in [64]. As before, we suppose that the piezoelectric material occupies the 2D lower half-space  $\mathbb{R}^{2-} = \{(x, z) : -\infty < x < \infty, z \leq 0\}$ . Provided that  $\partial/\partial y = 0$ , we can write the equation of motion (2.7) and Gauss's law (2.16) in  $\mathbb{R}^{2-}$  as

$$\begin{aligned} \frac{\partial \sigma_{xx}}{\partial x} + \frac{\partial \sigma_{xz}}{\partial z} &= -\omega^2 \rho u_x, \\ \frac{\partial \sigma_{xy}}{\partial x} + \frac{\partial \sigma_{yz}}{\partial z} &= -\omega^2 \rho u_y, \\ \frac{\partial \sigma_{xz}}{\partial x} + \frac{\partial \sigma_{zz}}{\partial z} &= -\omega^2 \rho u_z, \\ \frac{\partial D_x^-}{\partial x} + \frac{\partial D_z^-}{\partial z} &= 0. \end{aligned} \tag{3.25}$$

As long as  $-\infty < x < \infty$ , it is worth applying the Fourier transform with respect to  $x$  in (3.25)

$$\psi(k_x, z) = \int_{-\infty}^{\infty} \psi(x, z) e^{-ik_x x} dx. \tag{3.26}$$

The derivatives  $\partial/\partial x$  in (3.25) then turn into the products of the corresponding quantities and  $-ik_x$ .

Let all the quantities be dependent on  $z$  as  $e^{-ik_z z}$ . We expand (2.20) and (2.21) using the representations  $\mathbf{S} = \mathcal{B}\mathbf{u}$  and  $\mathbf{E} = -\nabla\varphi$  as follows

$$\begin{aligned} \sigma_{xx} &= -i(k_x c_{11} + k_z c_{15}) u_x - i(k_x c_{16} + k_z c_{14}) u_y \\ &\quad - i(k_x c_{15} + k_z c_{13}) u_z - i(k_x e_{11} + k_z e_{31}) \varphi, \\ \sigma_{zz} &= -i(k_x c_{31} + k_z c_{35}) u_x - i(k_x c_{36} + k_z c_{34}) u_y \\ &\quad - i(k_x c_{35} + k_z c_{33}) u_z - i(k_x e_{13} + k_z e_{33}) \varphi, \\ \sigma_{yz} &= -i(k_x c_{41} + k_z c_{45}) u_x - i(k_x c_{46} + k_z c_{44}) u_y \\ &\quad - i(k_x c_{45} + k_z c_{43}) u_z - i(k_x e_{14} + k_z e_{34}) \varphi, \\ \sigma_{xz} &= -i(k_x c_{51} + k_z c_{55}) u_x - i(k_x c_{56} + k_z c_{14}) u_y \\ &\quad - i(k_x c_{55} + k_z c_{53}) u_z - i(k_x e_{15} + k_z e_{35}) \varphi, \\ \sigma_{xy} &= -i(k_x c_{61} + k_z c_{65}) u_x - i(k_x c_{66} + k_z c_{64}) u_y \\ &\quad - i(k_x c_{65} + k_z c_{63}) u_z - i(k_x e_{16} + k_z e_{36}) \varphi, \\ D_x^- &= -i(k_x e_{11} + k_z e_{15}) u_x - i(k_x e_{16} + k_z e_{14}) u_y \\ &\quad - i(k_x e_{15} + k_z e_{13}) u_z + i(k_x \varepsilon_{11} + k_z \varepsilon_{13}) \varphi, \\ D_z^- &= -i(k_x e_{31} + k_z e_{35}) u_x - i(k_x e_{36} + k_z e_{34}) u_y \\ &\quad - i(k_x e_{35} + k_z e_{33}) u_z + i(k_x \varepsilon_{31} + k_z \varepsilon_{33}) \varphi. \end{aligned} \tag{3.27}$$

The components  $\sigma_{yy}$  and  $D_y$  are omitted in (3.27), because they do not appear in (3.25). Now, we set  $z = 0$  in (3.25) and substitute (3.27) for  $\sigma_{xx}, \sigma_{xy}, \sigma_{xz}$ , and  $D_x$  in (3.25). Denoting  $k_x = \omega s$  and  $k_z = \alpha \omega s$  we obtain

$$\begin{aligned}
 & s^2 (c_{11} + \alpha c_{15}) u_x + s^2 (c_{16} + \alpha c_{14}) u_y + \\
 & \quad + s^2 (c_{15} + \alpha c_{13}) u_z + s^2 (e_{11} + \alpha e_{31}) \varphi + \alpha s \frac{i\sigma_{xz}}{\omega} = \rho u_x, \\
 & s^2 (c_{61} + \alpha c_{65}) u_x + s^2 (c_{66} + \alpha c_{64}) u_y + \\
 & \quad + s^2 (c_{65} + \alpha c_{63}) u_z + s^2 (e_{16} + \alpha e_{36}) \varphi + \alpha s \frac{i\sigma_{yz}}{\omega} = \rho u_y, \\
 & s^2 (c_{51} + \alpha c_{55}) u_x + s^2 (c_{56} + \alpha c_{54}) u_y + \\
 & \quad + s^2 (c_{55} + \alpha c_{53}) u_z + s^2 (e_{15} + \alpha e_{35}) \varphi + \alpha s \frac{i\sigma_{zz}}{\omega} = \rho u_z, \\
 & s^2 (e_{11} + \alpha e_{15}) u_x + s^2 (e_{16} + \alpha e_{14}) u_y + \\
 & \quad + s^2 (e_{15} + \alpha e_{13}) u_z - s^2 (\varepsilon_{11} + \alpha \varepsilon_{13}) \varphi + \alpha s \frac{iD_z^-}{\omega} = 0.
 \end{aligned} \tag{3.28}$$

We write the equations for  $\sigma_{xz}, \sigma_{yz}, \sigma_{zz}$  and  $D_z$  from (3.27)

$$\begin{aligned}
 & s (c_{51} + \alpha c_{55}) u_x + s (c_{56} + \alpha c_{14}) u_y + \\
 & \quad + s (c_{55} + \alpha c_{53}) u_z + s (e_{15} + \alpha e_{35}) \varphi - \frac{i\sigma_{xz}}{\omega} = 0, \\
 & s (c_{41} + \alpha c_{45}) u_x + s (c_{46} + \alpha c_{44}) u_y + \\
 & \quad + s (c_{45} + \alpha c_{43}) u_z + s (e_{14} + \alpha e_{34}) \varphi - \frac{i\sigma_{yz}}{\omega} = 0, \\
 & s (c_{31} + \alpha c_{35}) u_x + s (c_{36} + \alpha c_{34}) u_y + \\
 & \quad + s (c_{35} + \alpha c_{33}) u_z + s (e_{13} + \alpha e_{33}) \varphi - \frac{i\sigma_{zz}}{\omega} = 0, \\
 & s (e_{31} + \alpha e_{35}) u_x + s (e_{36} + \alpha e_{34}) u_y + \\
 & \quad + s (e_{35} + \alpha e_{33}) u_z - s (\varepsilon_{31} + \alpha \varepsilon_{33}) \varphi - \frac{iD_z^-}{\omega} = 0
 \end{aligned} \tag{3.29}$$

and add them to system (3.28). Being written together, (3.28) and (3.29) compose a linear eigenvalue problem with respect to  $\alpha$  for a certain value of  $s$  [69].

In order to get expressions containing the charge density  $q_e$  instead of  $D_z^-$ , we point out that

$$\begin{aligned}
 & \mathbf{D}^+ = 0, \text{ in } \Omega_{\text{ele}}, \\
 & \mathbf{D}^+ = -\varepsilon_0 \nabla \varphi, \quad \frac{\partial D_x^+}{\partial x} + \frac{\partial D_z^+}{\partial z} = 0, \text{ in } \Omega_{\text{air}}.
 \end{aligned} \tag{3.30}$$

We assume that the electrode is thin enough. Then, since  $\varphi$  is continuous at  $z = 0$ , we

are able to write that, approximately,  $D_z^+ = \varepsilon_0 \omega |s_x| \varphi$  at  $z = 0$  and

$$\varepsilon_0 \omega |s_x| \varphi - D_z^- = \begin{cases} q_e, & \text{on } \Gamma_{\text{int}}, \\ 0, & \text{outside } \Gamma_{\text{int}}. \end{cases}$$

The last expression allows us to make a substitution for  $D_z^-$  in (3.28), (3.29) and obtain the eigenvalue problem that couples  $\mathbf{u}$  and  $\varphi$  with  $\sigma_z$  and  $q_e$  on the interface surface  $\Gamma_{\text{int}}$ .

The solution of this eigenvalue problem is a set of eight eigenvalues  $\{\alpha_i\}_{i=1}^8$  with corresponding eigenvectors

$$\underline{v}^{(i)} = \left( u_x^{(i)}, u_y^{(i)}, u_z^{(i)}, \varphi^{(i)}, \frac{i}{\omega} \sigma_{xz}^{(i)}, \frac{i}{\omega} \sigma_{yz}^{(i)}, \frac{i}{\omega} \sigma_{zz}^{(i)}, \frac{i}{\omega} q_e^{(i)} \right)^T = \left( \underline{w}_i, \frac{i}{\omega} \underline{T}_i \right)^T, \quad i = \overline{1, 8}.$$

Thus, a wave propagating in a piezoelectric half-space is a linear combination of eight partial waves  $v^{(i)}$

$$\begin{pmatrix} \mathbf{w}(z) \\ \frac{i}{\omega} \mathbf{T}(z) \end{pmatrix} = \sum_{i=1}^8 A_i \begin{pmatrix} \underline{w}_i \\ \frac{i}{\omega} \underline{T}_i \end{pmatrix} e^{-i\alpha_i \omega s z} \quad (3.31)$$

However, only four of eight eigenmodes satisfy with the boundary conditions as  $z \rightarrow -\infty$ : the partial waves have to transfer energy down from the surface  $z = 0$  and not the other way round [69].

Let  $\alpha_i$ ,  $i = \overline{1, 4}$  be the appropriate eigenvalues. They are in line with four eigenvectors  $v^{(i)}$ ,  $i = \overline{1, 4}$ . These four eigenvectors make it possible to find a  $4 \times 4$  matrix  $\underline{\underline{G}}$  that associates  $\underline{w} = \mathbf{w}|_{z=0}$  with  $\underline{T} = \mathbf{T}|_{z=0}$  as

$$\underline{w} = \underline{\underline{G}} \frac{i}{\omega} \underline{T}. \quad (3.32)$$

Since (3.32) must be valid for every  $\underline{w}$  and  $\underline{T}$  including the four admissible eigenvectors, one can find that [69]

$$\underline{\underline{G}} = \begin{pmatrix} u_x^{(1)} & u_x^{(2)} & u_x^{(3)} & u_x^{(4)} \\ u_y^{(1)} & u_y^{(2)} & u_y^{(3)} & u_y^{(4)} \\ u_z^{(1)} & u_z^{(2)} & u_z^{(3)} & u_z^{(4)} \\ \varphi^{(1)} & \varphi^{(2)} & \varphi^{(3)} & \varphi^{(4)} \end{pmatrix} \begin{pmatrix} \frac{i}{\omega} \sigma_{xz}^{(1)} & \frac{i}{\omega} \sigma_{xz}^{(2)} & \frac{i}{\omega} \sigma_{xz}^{(3)} & \frac{i}{\omega} \sigma_{xz}^{(4)} \\ \frac{i}{\omega} \sigma_{yz}^{(1)} & \frac{i}{\omega} \sigma_{yz}^{(2)} & \frac{i}{\omega} \sigma_{yz}^{(3)} & \frac{i}{\omega} \sigma_{yz}^{(4)} \\ \frac{i}{\omega} \sigma_{zz}^{(1)} & \frac{i}{\omega} \sigma_{zz}^{(2)} & \frac{i}{\omega} \sigma_{zz}^{(3)} & \frac{i}{\omega} \sigma_{zz}^{(4)} \\ \frac{i}{\omega} q_e^{(1)} & \frac{i}{\omega} q_e^{(2)} & \frac{i}{\omega} q_e^{(3)} & \frac{i}{\omega} q_e^{(4)} \end{pmatrix}^{-1}.$$

The matrix  $\underline{\underline{G}}$  which is obviously a function of  $s$  is referred to as the spectral Green's function [70]. According to the convolution theorem, the spacial analogue of (3.32) reads

$$\mathbf{w}(x, 0) = \int_{-\infty}^{\infty} \underline{\underline{G}}(\xi - x) \mathbf{T}(\xi) d\xi, \quad -\infty < x < \infty,$$

where  $\mathfrak{G}$  is obtained through the inverse Fourier transform of  $\frac{i}{\omega} \underset{\approx}{G}$

$$\mathfrak{G}(x) = \frac{i}{2\pi} \int_{-\infty}^{+\infty} \underset{\approx}{G}(s) e^{i\omega s x} ds. \quad (3.33)$$

In fact, the Green's function  $\mathfrak{G}$  for the whole axis  $-\infty < x < \infty$  is not the desired one. It is the Green's function  $\mathfrak{G}_p$  for one period. It is related to the spectral Green's function as [18]

$$\mathfrak{G}_p(x) = \frac{e^{-i\kappa x}}{p} \sum_{n=-\infty}^{+\infty} \mathfrak{G}\left(\kappa - \frac{2\pi n}{p}\right) e^{-i\frac{2\pi n}{p}x}, \quad -p/2 < x < p/2, \quad (3.34)$$

where  $e^{-i\kappa p} = \vartheta$ .

A remarkable feature of the spectral Green's function  $\underset{\approx}{G}$  is that it depends only on  $s_x$ , but has no implicit dependence on  $\omega$ . This means that  $\underset{\approx}{G}$  for a homogeneous piezoelectric half-space is a function of the slowness  $s_x$  and the material properties only. Once  $\underset{\approx}{G}$  has been computed, it can be used within the FEM/BEM routine for each frequency  $\omega$ . This makes the model (3.23), (3.24) a powerful tool for simulation of such structures. The situation becomes different and more complex for a layered substrate. For the sake of simplicity we shall consider a substrate that contains only two layers:  $-\infty < z \leq -d$  and  $-d < z \leq 0$ . We can compute the corresponding partial waves for both layers according to the previously given eigenvalue problem. However, in contrast to a single-layered substrate, we have eight admissible eigenvalues for the upper layer and four for the lower layer, i.e.

$$\begin{pmatrix} \mathbf{w}^{(1)}(z) \\ \frac{i}{\omega} \mathbf{T}^{(1)}(z) \end{pmatrix} = \sum_{i=1}^8 A_i \begin{pmatrix} \mathcal{W}_i^{(1)} \\ \frac{i}{\omega} \mathcal{T}_i^{(2)} \end{pmatrix} e^{-i\alpha_i^{(1)}\omega s z}, \quad -d < z \leq 0; \quad (3.35)$$

$$\begin{pmatrix} \mathbf{w}^{(2)}(z) \\ \frac{i}{\omega} \mathbf{T}^{(2)}(z) \end{pmatrix} = \sum_{i=1}^4 B_i \begin{pmatrix} \mathcal{W}_i^{(2)} \\ \frac{i}{\omega} \mathcal{T}_i^{(2)} \end{pmatrix} e^{-i\alpha_i^{(2)}\omega s z}, \quad -\infty < z \leq -d. \quad (3.36)$$

The spectral Green's function (3.32) is then defined as

$$\begin{pmatrix} \mathcal{U}_1^{(1)} & \dots & \mathcal{U}_8^{(1)} \end{pmatrix} \begin{pmatrix} A_1 \\ \dots \\ A_8 \end{pmatrix} = \underset{\approx}{G} \begin{pmatrix} \frac{i}{\omega} \mathcal{T}_1^{(1)} & \dots & \frac{i}{\omega} \mathcal{T}_8^{(1)} \end{pmatrix} \begin{pmatrix} A_1 \\ \dots \\ A_8 \end{pmatrix} \quad (3.37)$$

and cannot be calculated as earlier by the matrix inversion.

If the interface between the layers is non-conductive, the interface conditions read

$$\mathbf{w}^{(1)}(x, -d) = \mathbf{w}^{(2)}(x, -d), \quad \mathbf{T}^{(1)}(x, -d) = \mathbf{T}^{(2)}(x, -d). \quad (3.38)$$

The substitution of (3.35) and (3.36) into (3.38) yields

$$\begin{pmatrix} \underline{y}_1^{(1)} & \cdots & \underline{y}_8^{(1)} \\ \frac{i}{\omega} \underline{T}_1^{(1)} & \cdots & \frac{i}{\omega} \underline{T}_8^{(1)} \end{pmatrix} \text{diag} \left( e^{i\alpha_i^{(1)} \omega sd} \right) \begin{pmatrix} A_1 \\ \cdots \\ A_8 \end{pmatrix} = \begin{pmatrix} \underline{y}_1^{(2)} & \cdots & \underline{y}_4^{(2)} \\ \frac{i}{\omega} \underline{T}_1^{(2)} & \cdots & \frac{i}{\omega} \underline{T}_4^{(2)} \end{pmatrix} \text{diag} \left( e^{i\alpha_i^{(2)} \omega sd} \right) \begin{pmatrix} B_1 \\ \cdots \\ B_4 \end{pmatrix},$$

or shorter  $\underline{V}_1 \underline{D}_1 \underline{A} = \underline{V}_2 \underline{D}_2 \underline{B}$ . It follows that

$$\underline{A} = \underline{D}_1^{-1} \underline{V}_1^{-1} \underline{V}_2 \underline{D}_2 \underline{B}. \quad (3.39)$$

This enables us to use the matrix inversion to compute  $\underline{G}$  from (3.37) after the substitution of (3.39) for  $\underline{A}$  in (3.37).

Note that the spectral Green's function for a two-layered substrate is not any more independent of  $\omega$ . This is due to the matrices  $\underline{D}_1$  and  $\underline{D}_2$ , which depend on both  $\omega$  and  $d$ . This means that a new Green's function is to be computed for each frequency step within the FEM/BEM routine. The more layers the substrate has, the more effort is required for the numerical procedure. A way to overcome this is to extend the FEM scheme (3.11), (3.12) to some area that embrace all the inhomogeneities of the structure, like they have suggested in [71, 72]. Namely, the idea is to use BEM to describe the lowermost part of the substrate that is homogeneous<sup>1</sup>. It should help us to save the computational time, but one of the most important advantages of the model (3.23), (3.24) will be lost. It is the approximation of  $q_e$  that takes its behaviour near the electrode edges into account.

Another method closely related to FEM/BEM is FEM/SDA (spectral domain analysis) suggested by Hashimoto [19, 73, 74] and further developed by Naumenko for multi-layered structures [75, 76]. Similarly to the BEM analysis for the semi-infinite piezoelectric half-space, the partial wave decomposition (3.31) is used here, which in the end gives a relation like (3.32). However, the dependence of the quantities on  $x$  is not given through the Green's function (3.22), but by means of Fourier series expansion

$$\xi(x) = e^{-i\kappa x} \sum_{n=-\infty}^{+\infty} \xi_n e^{-i \frac{2\pi n x}{p}}.$$

Obviously, the last expression must be used with a finite number of harmonics within the numerical routine.

Along with the models that use coupling of FEM with BEM or SDA there is a possibility to stay within the pure FEM model yet reducing the computational domain. Such an approach has its advantages. FEM is robust and capable to effectively treat geometrical and material inhomogeneities as well as the effects caused by prestressing. The computational domain truncation can be done by introducing an artificial boundary  $\Gamma_0$  and impose absorbing boundary conditions on it. The idea has been inspired by the fact

---

<sup>1</sup>If there is a layered structure above the electrodes, its uppermost layer is modelled by means of BEM.

that there is a unique solution  $\xi$  of the Helmholtz equation

$$\Delta \xi(\mathbf{x}) + k^2 \xi(\mathbf{x}) = -f(\mathbf{x}), \quad \mathbf{x} \in \mathbb{R}^3$$

fulfilling boundary conditions [62]

$$\xi = O\left(\frac{1}{r}\right), \quad \frac{\partial \xi}{\partial r} + ik\xi = o\left(\frac{1}{r}\right), \quad r = |\mathbf{x}| \rightarrow \infty.$$

Analogous boundary conditions for the propagation of mechanical waves in isotropic solids can be found, for example, in [77].

If there is no waves coming from the area beyond  $\Gamma_0$ , we can set the first order absorbing boundary conditions

$$\left(\frac{\partial}{\partial n} + ik\right)\xi \Big|_{\Gamma_0} = 0. \quad (3.40)$$

These boundary conditions can be easily incorporated into the FEM model [35]. For our problem, there can only exist waves radiating into the substrate away from the electrode grating but not coming from the point at infinity  $z = -\infty$ . This makes the use of absorbing boundary conditions attractive. However, the condition (3.40) remains reflectionless only if the waves impinge on the surface  $\Gamma_0$  at right angles. If it is not the case, higher order ABC have to be used [78]. The situation is even more complex for waves propagating in anisotropic piezoelectric materials, where there are in general three kinds of waves at the same time. Investigation of this case can be found in [79].

In order to overcome the difficulties arising with the use of absorbing boundary conditions, we consider the perfectly matched layer (PML) absorbing technique. This approach provides a way to truncate the computational domain such that reflections from the artificial boundary are suppressed. A detailed description of the PML technique is to be found in the next section.

### 3.3 Perfectly matched layer technique

The PML was for the first time introduced by Berenger in his work [80] for the Maxwell equations. It was designed as a lossy layer that absorbed the waves impinging on the interface “layer/physical domain” without reflections at any angle and at any frequency. Berenger’s formulation has been referred to as the split field PML, because the physical solution were split into two non-physical artificial components. Sacks *et al.* in their work [81] suggested another PML formulation, where the layer was taken as an artificial anisotropic absorbing material. A more general way was proposed by Chew and Weedon in [82] using a complex coordinate stretching. It also turned out that the suggested formulations led to the same model. Being first introduced for the Maxwell equations, the PML technique was further applied by Chew and Liu [83] and Hastings *et al.* [84]

to elastodynamics.

Consider a 1D homogeneous wave equation

$$\frac{\partial^2 u}{\partial x^2}(x, t) = \frac{1}{c^2} \frac{\partial^2 u}{\partial t^2}(x, t), \quad x \in \mathbb{R}, \quad (3.41)$$

and let a PML occupy the right half-space  $x > 0$ . Introduced in such a way, the PML must be able to absorb right travelling wave solutions of (3.41) which are of the form

$$u_r(x, t) = \sum_{k, \omega} u_k(k, \omega) e^{i(\omega t - kx)}, \quad \frac{\omega}{k} = c.$$

The complex coordinate stretching technique is based on the analytic continuation of the exponential function so that it can take not only real  $x$  but also complex  $\tilde{x}$  arguments. The complex-valued function  $u_r(\tilde{x}, t)$  will satisfy with the equation (3.41) continued analytically to the complex plane. Namely,

$$\frac{\partial^2 u}{\partial \tilde{x}^2}(\tilde{x}, t) = \frac{1}{c^2} \frac{\partial^2 u}{\partial t^2}(\tilde{x}, t), \quad \tilde{x} \in \mathbb{C}. \quad (3.42)$$

Let the analytic continuation be defined as  $\tilde{x}(x) = x + if(x)$ . Then it follows that  $d\tilde{x} = (1 + if'(x)) dx$  and

$$\frac{\partial u}{\partial \tilde{x}} = \frac{\partial u}{\partial x} \left( \frac{d\tilde{x}}{dx} \right)^{-1} = \frac{1}{1 + if'(x)} \frac{\partial u}{\partial x}.$$

The choice  $f'(x) = -\sigma_x(x)/\omega$  yields

$$\frac{\partial u}{\partial \tilde{x}} = \frac{1}{1 + \frac{\sigma_x(x)}{i\omega}} \frac{\partial u}{\partial x} = \frac{1}{s_x(x, \omega)} \frac{\partial u}{\partial x}, \quad \tilde{x}(x) = x + \frac{1}{i\omega} \int_0^x \sigma_x(\xi) d\xi,$$

and the partial waves transform as follows

$$e^{i(\omega t - kx)} \rightarrow e^{i(\omega t - kx)} e^{-\frac{k}{\omega} \int_0^x \sigma_x(\xi) d\xi}. \quad (3.43)$$

In the PML region we choose  $\sigma_x > 0$ , which turns propagating waves into exponentially decaying ones. The attenuation rate is independent of the frequency, because of the factor  $k/\omega = 1/c$  in the exponent. In the region of propagation  $\sigma_x = 0$  and therefore  $\tilde{x} = x$ , which keeps the solution unchanged. Moreover, there are no reflections from the interface between the PML region and the region of propagation. In case of a 3D wave equation, the PML regions are introduced perpendicular to the  $x$ -,  $y$ -, and  $z$ -axes in order to provide the attenuation in the corresponding direction. The attenuation with respect to  $x$ ,  $y$ , and  $z$  is achieved by choosing non-zero functions  $\sigma_x(x)$ ,  $\sigma_y(y)$ , and  $\sigma_z(z)$  respectively. In the areas where two or more PML regions overlap one another the waves are damped in several directions simultaneously [35] (see fig. 3.7). Obviously, in our case

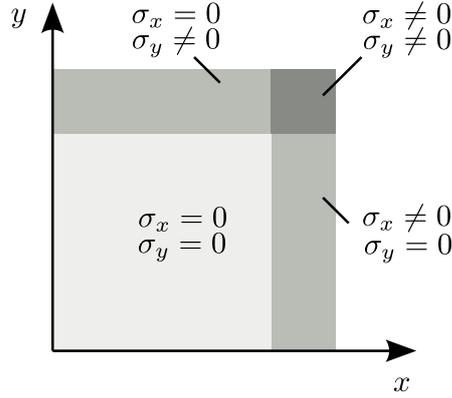


Figure 3.7: PML regions in 2D

a PML should be applied in order to damp the waves propagating in  $-z$ -direction.

We refer the coordinate stretching metric  $d\tilde{x} = s_x(x, \omega) dx$ , where

$$s_x(x, \omega) = 1 + \frac{\sigma_x(x)}{i\omega}, \quad (3.44)$$

as the classic metric. The formulation based on such a metric is then called the classic PML formulation. This metric modifies the waves in accordance to (3.43). Although it damps the propagating modes, it does not increase the damping of pure exponentially attenuating modes  $e^{i\omega t} e^{-kx}$ . Indeed,

$$e^{i\omega t} e^{-kx} = e^{i(\omega t + ikx)} \rightarrow e^{i(\omega t + \frac{k}{\omega} \int_0^x \sigma_x(\xi) d\xi)} e^{-kx}. \quad (3.45)$$

A more general way is to use the shifted metric defined as

$$s_x(x, \omega) = \nu(x) + \frac{\sigma_x(x)}{\alpha(x) + i\omega}, \quad (3.46)$$

where  $\sigma_x$  is the same as in (3.44),  $\nu \geq 1$ , and  $\alpha \geq 0$ . The parameters  $\nu$  and  $\alpha$  deliver specific properties to the metric (3.46). The first one is responsible for attenuation of evanescent waves and waves incident on the PML interface at near-grazing angles [85, 86]. The second one causes absorption of evanescent waves at low frequencies [87]. We refer to the PML formulation utilizing the metric (3.46) as the complex frequency shifted PML (CFS-PML) [88]. It was initially proposed for Maxwell equations by Kuzuoglu and Mittra [89] and further developed for elastodynamics [85, 86, 88, 90]. The classic formulation is obtainable from the shifted one by setting  $\nu = 1$  and  $\alpha = 0$ . The metric (3.46) modifies the waves according to the following rule

$$e^{i(\omega t - kx)} \rightarrow e^{i(\omega t - k \int_0^x \nu(\xi) d\xi)} e^{-\frac{k}{\omega} \int_0^x \frac{i\omega \sigma_x(\xi)}{\alpha(\xi) + i\omega} d\xi}. \quad (3.47)$$

Let  $\beta(\omega, x) = \omega/\alpha(x)$ , then (3.47) reads

$$e^{i(\omega t - kx)} \rightarrow e^{i(\omega t - k \int_0^x \nu(\xi) d\xi)} e^{-\frac{k}{\omega} \left( \int_0^x \frac{\beta^2(\xi) \sigma_x(\xi)}{1 + \beta^2(\xi)} d\xi + i \int_0^x \frac{\beta(\xi) \sigma_x(\xi)}{1 + \beta^2(\xi)} d\xi \right)}.$$

For a pure real wavenumber  $k$  corresponding to pure propagating modes we obtain

$$e^{-ikx} \rightarrow e^{-ik \int_0^x \left( \nu + \frac{1}{\omega} \frac{\beta \sigma_x}{1 + \beta^2} \right) d\xi} e^{-\frac{k}{\omega} \int_0^x \frac{\beta^2 \sigma_x}{1 + \beta^2} d\xi}, \quad (3.48)$$

where the factor  $e^{i\omega t}$  and the argument  $\xi$  are omitted for the sake of brevity. The attenuation in this case is caused by the exponent

$$-\frac{k}{\omega} \int_0^x \frac{\beta^2 \sigma_x}{1 + \beta^2} d\xi$$

and is not independent of the frequency as it is within the classic formulation, because  $\beta$  is a function of  $\omega$ . The parameter  $\nu$  changes the wavenumber, and the term  $\frac{\beta \sigma_x}{1 + \beta^2}$  shifts the phase of the wave, hence the name CFS-PML.

In case of a pure imaginary wavenumber  $-ik$ , which describes a pure exponentially attenuating wave, we have

$$e^{-kx} \rightarrow e^{i \frac{k}{\omega} \int_0^x \frac{\beta^2 \sigma_x}{1 + \beta^2} d\xi} e^{-k \int_0^x \left( \nu + \frac{1}{\omega} \frac{\beta \sigma_x}{1 + \beta^2} \right) d\xi}. \quad (3.49)$$

Thus the shifted metric amplifies the damping rate of evanescent waves, which is in contrast to the classic one. The increasing of the attenuation is due to the parameters  $\nu$  and  $\frac{\beta \sigma_x}{1 + \beta^2}$ . The first one provides the frequency independent attenuation, whereas the second one acts depending on the frequency.

Now, let us focus on the role of the parameter  $\alpha$  in the damping of propagating and evanescent waves. For the sake of simplicity we take  $\alpha = \text{const}$  and consider the functions

$$\begin{aligned} f_1(\beta) &= \frac{\beta^2}{1 + \beta^2} = \frac{\omega^2}{\alpha^2 + \omega^2} \quad \text{and} \\ f_2(\beta) &= \frac{\beta}{1 + \beta^2} = \frac{\omega \alpha}{\alpha^2 + \omega^2}. \end{aligned}$$

They are responsible for the frequency dependent attenuation of propagating and evanescent waves, respectively. The plots in fig. 3.8 show that  $f_1(\beta) \rightarrow 1$  as  $\beta \rightarrow +\infty$  and therefore the difference between the shifted and the classic PML formulations becomes negligible at high frequencies. On the other hand, we see a tremendous fall of the attenuation rate at low frequencies. As for evanescent waves, the most efficient damping is reachable near  $\beta = 1$ , whereas at high frequencies  $f_2(\beta) \rightarrow 0$ . Thus the CFS-PML formulation causes the attenuation of evanescent waves at low frequencies [87].

The fact that  $\alpha$  can be chosen in a way to “switch” the damping properties of CFS-

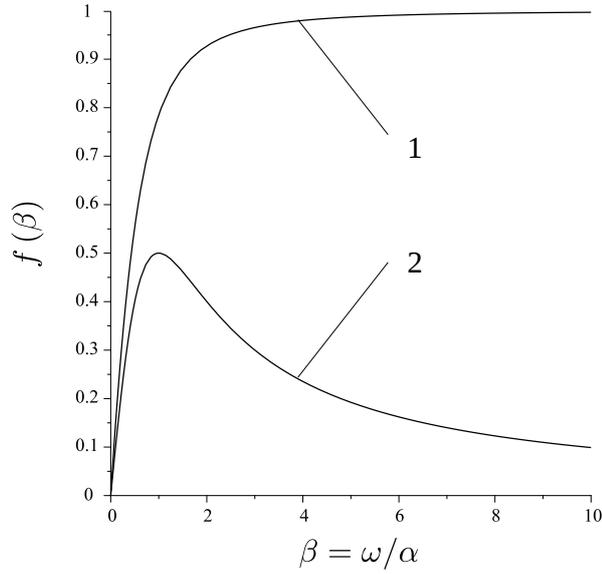


Figure 3.8: To the frequency dependent attenuation rates of propagating (1) and evanescent (2) waves

PML will play a significant role in the problem we consider here. Indeed, pure surface waves, whose displacements vanish with the substrate depth, propagate with velocities lower than the slow shear wave velocity  $v_{\text{SSW}}$  (see section 2.3). It means they can arise at frequencies  $f < f_{\text{SSW}} = v_{\text{SSW}}/\lambda$ . On the contrary, if the frequency is higher than  $f_{\text{SSW}}$ , some components of the mechanical displacements start radiating into the substrate. Thus a proper choice of  $\alpha$  can make the PML absorb the waves within the whole frequency range [91]. It is obvious that the classic PML would be only able to deal with the waves radiating into the substrate remaining of no use for the damping of surface waves.

The role of the parameter  $\nu$  is clear in case of evanescent waves, but is not obvious for propagating waves. Some authors used to take  $\nu = 1$ ; thus leaving only the frequency dependent damping caused by  $\alpha$  [90, 92]. Others mentioned its role in the damping of attenuating waves [85, 87], or concluded from numerical tests that it affected the waves propagating at near-grazing angles to the interface between the PML and the propagation domain [88]. The last observation was theoretically explained by Zhang and Shen in their work [93]. A  $\nu > 1$  introduces an anisotropy in the PML domain such that the components of the wavevectors normal to the interface increase, whereas the tangential ones remain the same. It is illustrated in fig. 3.9, where the slowness diagram for the pressure wave in steel is shown. The material is isotropic and the slowness curve in propagation domain is a circle. The waves propagate towards the planes  $s_x = \text{const}$  with the angle  $\phi$ . If a CFS-PML with  $\nu > 1$  is applied in  $z$ -direction, the slowness curve gets stretched to an elliptic form, because of the anisotropy caused by  $\nu$ . The angle is then changed to  $\tilde{\phi} < \phi$ . Therefore the wave propagates closer to the direction normal

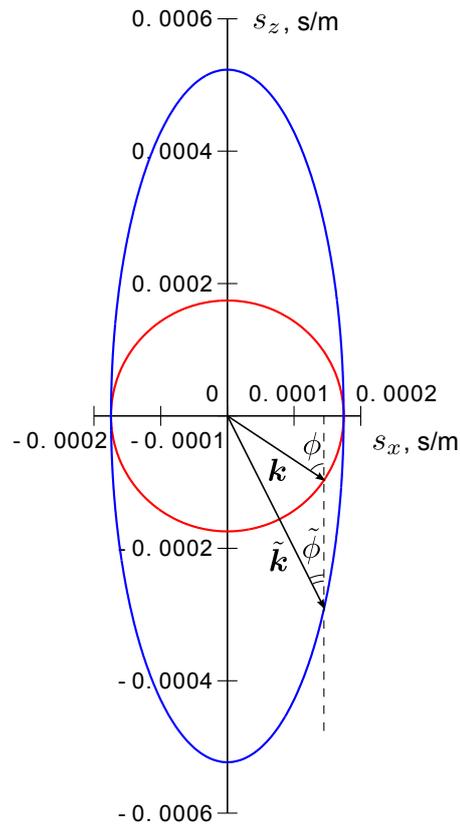
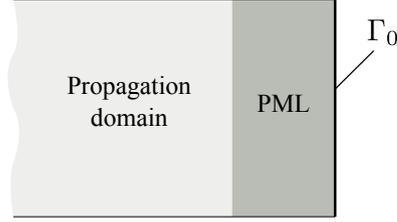


Figure 3.9: Pressure wave slowness diagram in stainless steel in propagation domain (red) and in PML domain applied in  $z$ -direction (blue)


 Figure 3.10: PML domain truncated by the boundary  $\Gamma_0$ 

to the interface, which leads to a better damping than if it were for  $\nu = 1$ . The blue curve in fig. 3.9 corresponds to  $\nu = 2$ . Another way to increase the damping of obliquely propagating waves is to scale the parameter  $\sigma$  to  $\sigma/\cos\phi$  [35].

The PML technique is used in practice to reduce the computational domain. Since the waves that penetrate the PML domain become attenuating, we may assume that at some distance their amplitudes are small enough. This enables us to truncate the PML domain imposing the homogeneous Dirichlet boundary condition at some surface  $\Gamma_0$  [94] (see fig. 3.10). A wave impinging on  $\Gamma_0$  will positively be reflected from it and travel back towards the region of propagation. The reflected wave will thus affect the solution, whereas the interface between the region of propagation and the PML is still reflectionless. However, the wave reflected from  $\Gamma_0$  will be again damped on its way back. Indeed, let the incident and the reflected wave have the following forms

$$A(x) = A_0 e^{-ikx} e^{-\frac{\sigma_0}{c}x}, \quad B(x) = B_0 e^{ikx} e^{\frac{\sigma_0}{c}x}, \quad (3.50)$$

where  $c = \omega/k$ ,  $\sigma_x = \sigma_0$  is taken to be a constant, and the dependence on time is omitted for brevity. Then it follows that

$$|B(x_1)| = B_0 e^{\frac{\sigma_0}{c}x_1} \leq B_0 e^{\frac{\sigma_0}{c}x_2} = |B(x_2)|, \quad \forall x_1 \leq x_2. \quad (3.51)$$

In order to study the reflection coefficient at the interface  $x = 0$ , suppose that the perfectly matched layer has length  $L$ . We apply the homogeneous Dirichlet boundary condition at  $x = L$  so that

$$v(L) = A(L) + B(L) = 0. \quad (3.52)$$

From (3.52) and (3.51) we obtain

$$B_0 = -A_0 e^{-2ikL} e^{-\frac{2\sigma_0}{c}L}.$$

The theoretical reflection coefficient  $R$  at the interface is equal to  $|B(0)/A(0)| = |B_0/A_0|$ . Thus

$$R_0 = e^{-\frac{2\sigma_0}{c}L}. \quad (3.53)$$

The value of the damping parameter derived from (3.53) reads

$$\sigma_0 = \frac{c \ln \frac{1}{R_0}}{2L}. \quad (3.54)$$

It follows from (3.54) that the thinner the PML is, the larger  $\sigma_0$  must be taken to keep the same reflection coefficient. However, very large  $\sigma_0$  or, the same, very small theoretical reflection coefficient  $R_0$  can cause numerical reflections if the PML layer is too thin [35]. It is suggested in [35] to choose  $R_0 = 10^{-3}$ . If  $\sigma_x(x)$  is chosen in a polynomial form

$$\sigma_x(x) = \sigma_0 \left( \frac{x}{L} \right)^{n_1}, \quad (3.55)$$

one can find that

$$\sigma_0 = \frac{(n_1 + 1) c \ln \frac{1}{R_0}}{2L}. \quad (3.56)$$

For a quadratic or cubic  $\sigma_x(x)$  Johnson [94] suggests that the width of the PML should be set about  $0.5 \div 1$  of the wavelength.

The CFS metric is generally utilised with  $\sigma$  defined according to (3.55) and  $\alpha$  and  $\nu$  having the following forms

$$\alpha(x) = \alpha_0 \left( 1 - \frac{x}{L} \right)^{n_2}, \quad (3.57)$$

$$\nu(x) = 1 + \nu_0 \left( \frac{x}{L} \right)^{n_3}. \quad (3.58)$$

The form of  $\alpha$  is chosen differently from that of  $\sigma$  and  $\nu$  to reduce reflection errors of evanescent waves and absorb pure propagating waves at low frequencies [95, 96]. Setting  $\alpha = \pi f'$ , we can reach an appropriate attenuation rate for propagating and evanescent waves at the frequencies  $f > f'$  and  $f < f'$ , respectively [86, 93, 97]. As we have mentioned above, it is reasonable to take  $f' = f_B = v_B/\lambda$  in our case.

One should be careful choosing the value of  $\nu_0$ , for its choice is in fact according to a rule of thumb. Since it clearly makes pure evanescent waves (with pure imaginary wavenumber) decay faster, it may take any value  $\nu_0 \geq 1$ . However, if the wavenumber contains a real part, reflections can be caused by a discretization of the PML domain used to solve the problem numerically. Since  $\nu$  increases the wavenumber (and hence decreases the wavelength) of the waves (see (3.48)), the choice of  $\nu_0$  must be consistent with the length of the PML and the size of mesh elements. The relation between the order  $q$  of FE basis functions, the mesh size  $h$ , and the wavenumber  $\tilde{k}$  mentioned in [35] reads

$$q + \frac{1}{2} > \frac{\tilde{k}h}{2} + C (\tilde{k}h)^{1/3},$$

where  $C$  is a constant usually chosen equal to 1. In practice we recommend to take  $h \approx$

$\tilde{\lambda}/20$ , where  $\tilde{\lambda}$  is the maximal wavelength of the waves radiating into the substrate. It can be determined for a certain frequency according to slowness curves.

The value of  $\sigma_0$  containing the wave velocity  $c$  is modified in the problems of elastic waves propagation in the following way. Since there can be three partial waves with different velocities, we use the velocity  $v_{\text{LW}}$  of the fastest one – quasi-longitudinal wave – for  $c$  in (3.56). The degrees of the polynomials in (3.55), (3.57), and (3.58) are from now on taken as  $n_1 = 2$ ,  $n_2 = 1$ , and  $n_3 = 2$ .

Now, we address the FEM routine in a PML domain in order to see how it is influenced by the complex coordinate stretching. Consider a 3D homogeneous Helmholtz partial differential equation

$$\nabla \cdot [\mathbf{a}] \nabla \xi + \omega^2 \rho \xi = 0.$$

Its expanded form reads

$$\frac{\partial}{\partial x} a_x \frac{\partial \xi}{\partial x} + \frac{\partial}{\partial y} a_y \frac{\partial \xi}{\partial y} + \frac{\partial}{\partial z} a_z \frac{\partial \xi}{\partial z} + \omega^2 \rho \xi = 0. \quad (3.59)$$

The application of the complex coordinate stretching (3.59) yields

$$\frac{1}{s_x} \frac{\partial}{\partial x} a_x \frac{\partial \xi}{\partial x} + \frac{1}{s_y} \frac{\partial}{\partial y} a_y \frac{\partial \xi}{\partial y} + \frac{1}{s_z} \frac{\partial}{\partial z} a_z \frac{\partial \xi}{\partial z} + \omega^2 \rho \xi = 0. \quad (3.60)$$

We multiply (3.60) by  $s_x s_y s_z$  and a test function  $\xi'$  and integrate the resulting expression over a domain  $\Omega'$ , which results in

$$\int_{\Omega'} \left( s_y s_z \frac{\partial}{\partial x} a_x \frac{\partial \xi}{\partial x} + s_x s_z \frac{\partial}{\partial y} a_y \frac{\partial \xi}{\partial y} + s_x s_y \frac{\partial}{\partial z} a_z \frac{\partial \xi}{\partial z} \right) \xi' d\Omega + \omega^2 \int_{\Omega'} s_x s_y s_z \rho \xi \xi' d\Omega = 0.$$

Since  $s_x$ ,  $s_y$ , and  $s_z$  are functions of only  $x$ ,  $y$ , and  $z$  respectively, we can integrate the last equation by parts such that

$$- \int_{\Omega'} \left( s_y s_z \frac{\partial \xi'}{\partial x} a_x \frac{\partial \xi}{\partial x} + s_x s_z \frac{\partial \xi'}{\partial y} a_y \frac{\partial \xi}{\partial y} + s_x s_y \frac{\partial \xi'}{\partial z} a_z \frac{\partial \xi}{\partial z} \right) d\Omega + \omega^2 \int_{\Omega'} s_x s_y s_z \rho \xi \xi' d\Omega = 0,$$

which further yields

$$- \int_{\Omega'} \left( \frac{1}{s_x} \frac{\partial \xi'}{\partial x} s_x s_y s_z a_x \frac{1}{s_x} \frac{\partial \xi}{\partial x} + \frac{1}{s_y} \frac{\partial \xi'}{\partial y} s_x s_y s_z a_y \frac{1}{s_y} \frac{\partial \xi}{\partial y} + \frac{1}{s_z} \frac{\partial \xi'}{\partial z} s_x s_y s_z a_z \frac{1}{s_z} \frac{\partial \xi}{\partial z} \right) d\Omega + \omega^2 \int_{\Omega'} s_x s_y s_z \rho \xi \xi' d\Omega = 0.$$

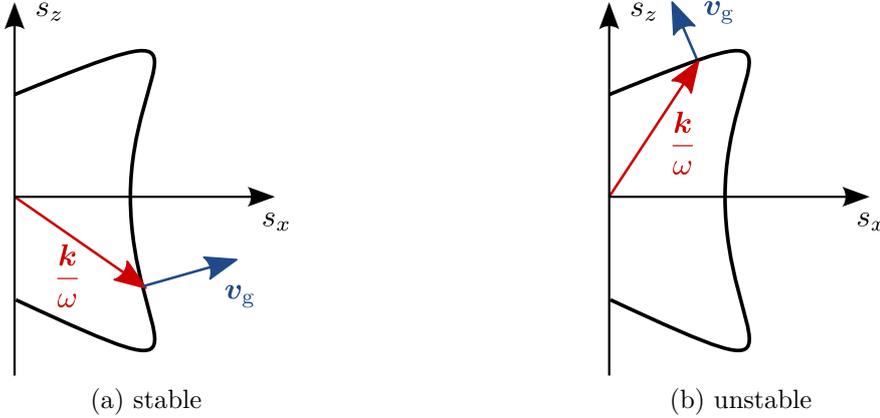


Figure 3.11: To the geometric interpretation of the necessary stability condition

Denoting  $[\tilde{\mathbf{a}}] = s_x s_y s_z [\mathbf{a}]$ ,  $\tilde{\varrho} = s_x s_y s_z \varrho$ , and  $\tilde{\nabla} = \left( \frac{1}{s_x} \frac{\partial}{\partial x}, \frac{1}{s_y} \frac{\partial}{\partial y}, \frac{1}{s_z} \frac{\partial}{\partial z} \right)$ , we arrive at

$$- \int_{\Omega'} \tilde{\nabla} \xi' \cdot [\tilde{\mathbf{a}}] \tilde{\nabla} \xi d\Omega + \omega^2 \int_{\Omega'} \tilde{\varrho} \xi' \xi d\Omega = 0. \quad (3.61)$$

If  $s_x = s_y = s_z = 1$ , (3.61) will become the weak form of the initial equation. This means that the weak form of PDE does not change its pattern in a PML domain. Its only the differential operators and the material data that must be modified according to the metric of the PML. The same is valid for the FEM model (3.11), (3.12). In the PML domain we should substitute  $\tilde{\mathcal{B}}$  and  $\tilde{\nabla}$  for the differential operators and modify the material data multiplying them by  $s_{\Pi} = s_x s_y s_z$ . We recall that in our case the PML is applied to truncate the computational domain in  $z$ -direction. Therefore, the stretching is only used with respect to the  $z$ -coordinate such that  $s_x = s_y = 1$ ,  $s_{\Pi} = s_z$ , and  $\frac{\partial}{\partial z} \rightarrow \frac{1}{s_z} \frac{\partial}{\partial z}$ .

We should also refer to the stability issues of the PML technique for elastodynamics. Instabilities caused by a PML can occur solving the elastodynamic PDEs in time domain for some anisotropic materials. In [98] the authors suggested a necessary condition of high frequency stability of the PML. The condition asserts that if a PML applied in  $x$ -direction is stable, the corresponding components of the wave vector  $\mathbf{k}$  and the group velocity vector  $\mathbf{v}_g$  have the same sign, i.e.  $(v_g)_x k_x \geq 0$ . A geometric interpretation of this condition is shown in fig. 3.11 for a PML applied in  $x$ -direction.

A technique called multiaxial PML (M-PML) was proposed by Mesa-Fajardo and Pagageorgiou in [99]. They suggested the damping profiles to be specified not only in the direction orthogonal to the interface, but also in other directions. It provides a long time stability in anisotropic media. Actually, this method has been proven not to be perfectly matched, yet the reflections from the interface are very small [100]. Another issue is that M-PML does not conform with the complex coordinate stretching technique.

Therefore, one cannot obtain a numerical model of the form (3.11), (3.12) in the PML domain. The stress-velocity formulation of the equation of motion should be used there instead.

We certainly await instabilities in our problem for the anisotropic materials that behave as shown in fig. 3.11, (b). However, we stick to the approach based on CFS-PML, since it satisfies our demands. Indeed, the situation depicted in fig. 3.11, (b) does not correspond to any surface wave solution. The solutions in the region of instabilities are bulk waves (see section 2.3), which makes this region of no interest for us.

### 3.4 Periodic boundary conditions handling

In this section we proceed to the last open question of the developed numerical model: How do we have to treat the periodic boundary conditions. The procedure that we describe here is more or less similar to that for non-conforming interfaces [35]. After we have introduced the PML and therefore truncated the computational domain, we should integrate the constraints (3.9), (3.10) to the numerical model (3.11), (3.12). The computational domain now looks as shown in fig. 3.12. From now on we understand by  $\Omega$  the area bounded by the surface  $\Gamma_a \cup \Gamma_l \cup \Gamma_r \cup \Gamma_0$  which comprises the areas of the electrode  $\Omega_{\text{ele}}$ , the substrate  $\Omega_{\text{sub}}$ , the PML  $\Omega_{\text{PML}}$ , and the surrounding air  $\Omega_{\text{air}}$ .

We assume that the surfaces  $\Gamma_l$  and  $\Gamma_r$  have the same shape and area. Let  $\mathcal{P}$  be a one-to-one (bijective) map that associates a point  $\mathbf{x}_l \in \Gamma_l$  with a point  $\mathbf{x}_r \in \Gamma_r$  with respect to the periodicity of the structure. Let also  $\mathcal{P}$  preserve the length, i.e.

$$d\mathbf{x}_r = \frac{\partial \mathcal{P}}{\partial \mathbf{x}_l} d\mathbf{x}_l: (d\mathbf{x}_r)^2 = (d\mathbf{x}_l)^2.$$

Then it follows that  $\frac{\partial \mathcal{P}}{\partial \mathbf{x}_l} = [\mathbf{I}]$ , and  $\det \frac{\partial \mathcal{P}}{\partial \mathbf{x}_l} = \det [\mathbf{I}] = 1$ , and an integral over  $\Gamma_r$  is transformed to a corresponding integral over  $\Gamma_l$  such that

$$\int_{\Gamma_r} \xi(\mathbf{x}_r) d\Gamma_r = \int_{\Gamma_l} \xi(\mathcal{P}\mathbf{x}_l) d\Gamma_l. \quad (3.62)$$

The structures we consider here are supposed to have a translational periodicity [101], where the surfaces  $\Gamma_l$  and  $\Gamma_r$  are moved from one another with respect to a vector  $\mathbf{t}$ . Therefore we can write

$$\mathbf{x}_r = \mathcal{P}\mathbf{x}_l = \mathbf{x}_l + \mathbf{t}, \quad \mathbf{x}_l = \mathcal{P}^{-1}\mathbf{x}_r = \mathbf{x}_r - \mathbf{t}.$$

Now, we refer to the model (3.13) implying that the derivatives and the material data in the PML domain are defined in accordance with the considerations from section 3.3. We deal with discretized domains within the FEM routine. If the surfaces  $\Gamma_l$  and  $\Gamma_r$  are discretized in a conforming way, meaning that every node  $\mathbf{M}_l^{(k)}$  on  $\Gamma_l$  has a node  $\mathbf{M}_r^{(k)} = \mathcal{P}\mathbf{M}_l^{(k)}$  on  $\Gamma_r$ , we can split the unknown  $\mathbf{w}$  into three parts  $\mathbf{w}_i$ ;  $\mathbf{w}_l$ ; and  $\mathbf{w}_r$ . These parts

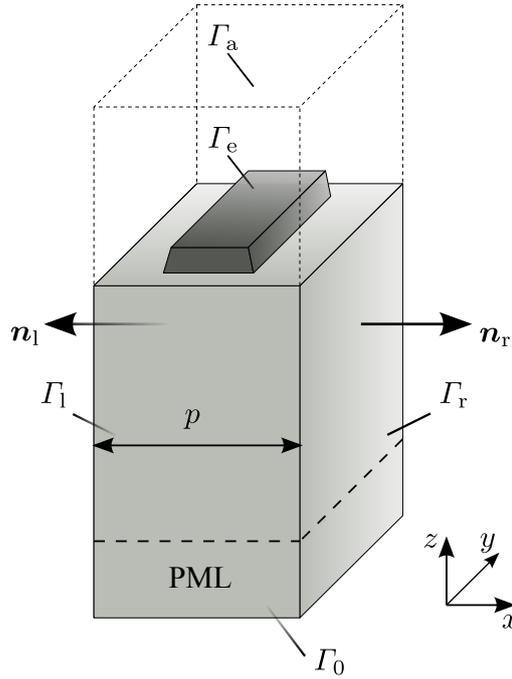


Figure 3.12: A unit cell truncated using a PML

correspond to the solution in the interior area and on the surfaces  $\Gamma_l$ ,  $\Gamma_r$  respectively. In this case, it is possible to reduce the equation (3.13) to a linear system for  $\mathbf{w}_i$  and  $\mathbf{w}_l$  as described in [102]. Therefore, the boundary conditions (3.14) are incorporated in their strong form.

However, it is likely, especially in 3D, that  $\Gamma_l$  and  $\Gamma_r$  are discretized in an arbitrary way. In this case we integrate the periodic boundary conditions into the numerical model in a weak form. The easiest approach is to use mortar FEM [35] with the Lagrange multipliers technique [103]. We denote the Lagrange multiplier as  $\boldsymbol{\lambda} = \mathbf{T}|_{\Gamma_l}$ . After that we change the variable in the integral over  $\Gamma_r$  according to (3.62) and obtain

$$\int_{\Omega} (\mathcal{D}\mathbf{w}')^T [\mathbf{C}] \mathcal{D}\mathbf{w} d\Omega - \omega^2 \int_{\Omega} (\mathbf{w}')^T [\boldsymbol{\rho}] \mathbf{w} d\Omega - \int_{\Gamma_l} (\mathbf{w}'(\mathbf{x}_l) - \vartheta \mathbf{w}'(\mathcal{P}\mathbf{x}_l))^T \boldsymbol{\lambda} d\Gamma = 0. \quad (3.63)$$

The weak form of the first boundary condition from (3.14) reads

$$\int_{\Gamma_l} (\boldsymbol{\lambda}')^T (\mathbf{w}(\mathcal{P}\mathbf{x}_l) - \vartheta \mathbf{w}(\mathbf{x}_l)) d\Gamma = 0. \quad (3.64)$$

Following the FEM procedure we write the FE-approximation (3.15) for  $\mathbf{w}$  and for  $\boldsymbol{\lambda}$ .

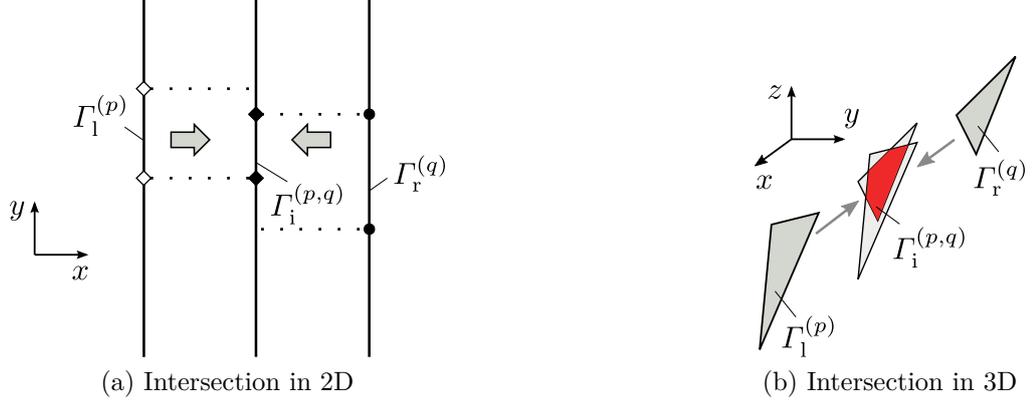


Figure 3.13: To the intersection of meshes

This yields

$$\sum_{k=1}^{n_n} \mathbf{w}_k \left( \int_{\Omega} (\mathcal{D}\mathbf{N}_j)^T [\mathbf{C}] \mathcal{D}\mathbf{N}_k d\Omega - \omega^2 \int_{\Omega} (\mathbf{N}_j)^T [\boldsymbol{\rho}] \mathbf{N}_k d\Omega \right) - \sum_{k=1}^{n_l} \boldsymbol{\lambda}_k \int_{\Gamma_1} (\bar{\mathbf{N}}_j(\mathbf{x}_1) - \vartheta \bar{\mathbf{N}}_j(\mathcal{P}\mathbf{x}_1))^T \bar{\mathbf{N}}_k(\mathbf{x}_1) d\Gamma = 0, \quad j = \overline{1, n_n}; \quad (3.65)$$

$$\sum_{k=1}^{n_n} \mathbf{w}_k \int_{\Gamma_1} (\bar{\mathbf{N}}_j(\mathbf{x}_1))^T (\bar{\mathbf{N}}_k(\mathcal{P}\mathbf{x}_1) d\Gamma - \vartheta \bar{\mathbf{N}}_k(\mathbf{x}_1)) d\Gamma = 0, \quad j = \overline{1, n_l}. \quad (3.66)$$

The bar in (3.65), (3.66) indicates the traces of corresponding quantities on  $\Gamma_1$ , i.e.  $\bar{\xi} = \text{Tr}_{\Gamma_1}(\xi)$ , and  $n_l$  means the number of nodes on  $\Gamma_1$ .

In matrix form, the system (3.65), (3.66) reads

$$\begin{pmatrix} \underset{\approx}{K} - \omega^2 \underset{\approx}{M} & -\underset{\approx}{L}^T + \vartheta \underset{\approx}{R}^T \\ -\vartheta \underset{\approx}{L} + \underset{\approx}{R} & 0 \end{pmatrix} \begin{pmatrix} \underset{\approx}{w} \\ \underset{\approx}{\lambda} \end{pmatrix} = \begin{pmatrix} \underset{\approx}{f} \\ 0 \end{pmatrix}. \quad (3.67)$$

The elements of the matrices  $\underset{\approx}{K}$  and  $\underset{\approx}{M}$  are calculated according to the formulae (3.17) and (3.18), respectively. The matrices  $\underset{\approx}{L}$ ,  $\underset{\approx}{R}$  are defined according to the surface integrals

$$\{L\}_{j,k} = \int_{\Gamma_1} (\bar{\mathbf{N}}_j(\mathbf{x}_1))^T \bar{\mathbf{N}}_k(\mathbf{x}_1) d\Gamma = \sum_{i=1}^{n_l} \int_{\Gamma_1^{(i)}} (\bar{\mathbf{N}}_j(\mathbf{x}_1))^T \bar{\mathbf{N}}_k(\mathbf{x}_1) d\Gamma \quad (3.68)$$

$$\{R\}_{j,k} = \int_{\Gamma_1} (\bar{\mathbf{N}}_j(\mathbf{x}_1))^T \bar{\mathbf{N}}_k(\mathcal{P}\mathbf{x}_1) d\Gamma = \sum_{i=1}^{n_l} \int_{\Gamma_1^{(i)}} (\bar{\mathbf{N}}_j(\mathbf{x}_1))^T \bar{\mathbf{N}}_k(\mathcal{P}\mathbf{x}_1) d\Gamma. \quad (3.69)$$

The functions  $N_j$ ,  $N_k$  in (3.68) belong to the same domain. Therefore the integrals are evaluated in the way we discussed in section 3.1. At the same time, it is not the case for the integrals in (3.69), because the basis functions are defined on different domains.

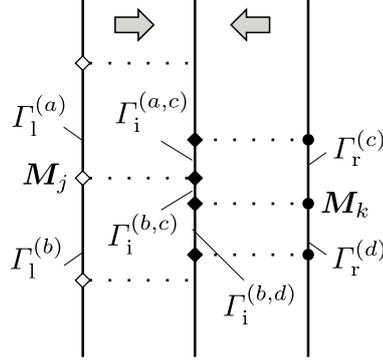


Figure 3.14: Intersection of FE basis functions supports

In this case the integration is done with respect to a mesh built through the intersection of those for  $\Gamma_1$  and  $\Gamma_r$  (see fig. 3.13). Let the FE basis functions  $\bar{N}_j$  and  $\bar{N}_k$  have their supports  $\Gamma_1^{(a)} \cup \Gamma_1^{(b)}$  and  $\Gamma_r^{(c)} \cup \Gamma_r^{(d)}$  as shown in fig. 3.14. We create an intersection of the supports as follows (see fig. 3.14)

$$\Gamma_i = \Gamma_i^{(a,c)} \cup \Gamma_i^{(b,c)} \cup \Gamma_i^{(b,d)} = \left( \Gamma_1^{(a)} \cup \Gamma_1^{(b)} \right) \cap \mathcal{P}^{-1} \left( \Gamma_r^{(c)} \cup \Gamma_r^{(d)} \right).$$

Then (3.69) reads

$$\begin{aligned} \int_{\Gamma_1} \left( \bar{N}_j(\mathbf{x}_1) \right)^T \bar{N}_k(\mathcal{P}\mathbf{x}_1) d\Gamma &= \int_{\Gamma_i^{(a,c)}} \left( \bar{N}_j^{(a)}(\mathbf{x}_1) \right)^T \bar{N}_k^{(c)}(\mathcal{P}\mathbf{x}_1) d\Gamma \\ &+ \int_{\Gamma_i^{(b,c)}} \left( \bar{N}_j^{(b)}(\mathbf{x}_1) \right)^T \bar{N}_k^{(c)}(\mathcal{P}\mathbf{x}_1) d\Gamma + \int_{\Gamma_i^{(b,d)}} \left( \bar{N}_j^{(b)}(\mathbf{x}_1) \right)^T \bar{N}_k^{(d)}(\mathcal{P}\mathbf{x}_1) d\Gamma. \end{aligned}$$

One should bear in mind that it can be not enough to apply the transformation  $\mathcal{P}^{-1}$  to the elements from  $\Gamma_r$  to get an intersection of two grids. If  $\Gamma_1$  and  $\Gamma_r$  are curved surfaces, the elements  $\Gamma_1^{(p)}$  and  $\mathcal{P}^{-1}\Gamma_r^{(q)}$  have to lie on the same plane. Otherwise, an orthogonal projection onto a common plane is required (see [35]).

The system (3.67) is a saddle point problem and reportedly requires a special treatment for solving [103]. The way of regularisation suggested in [103] is to use the double Lagrange multipliers approach which leads to a system with a dense matrix. However, the sparse direct solver PARDISO [104] seems to have no difficulties in precision and in running time for both the single and the double Lagrange multipliers approaches, and hence the numerical scheme can be kept in the form (3.67).

Numerical instabilities can still arise here. Namely, the Lagrange multiplier  $\boldsymbol{\lambda}$  contains the mechanical  $\boldsymbol{\lambda}_m$  and the electrostatic  $\lambda_e$  parts. Writing the equation (3.63) in the extended form we obtain

$$\int_{\Omega} (\mathcal{B}\mathbf{u}')^T [\mathbf{c}^E] \mathcal{B}\mathbf{u} d\Omega + \int_{\Omega} (\mathcal{B}\mathbf{u}')^T [\mathbf{e}]^T \nabla \varphi d\Omega$$

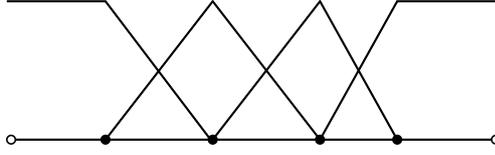


Figure 3.15: Lagrange multiplier FE space

$$\begin{aligned}
 & -\omega^2 \int_{\Omega} \rho (\mathbf{u}')^T \mathbf{u} d\Omega - \int_{\Gamma_1} (\mathbf{u}'(\mathbf{x}_1) - \vartheta \mathbf{u}'(\mathcal{P}\mathbf{x}_1))^T \boldsymbol{\lambda}_m d\Gamma = 0, \\
 & \int_{\Omega} (\nabla \varphi')^T [\mathbf{e}] \mathcal{B} \mathbf{u} d\Omega - \int_{\Omega} (\nabla \varphi')^T [\boldsymbol{\varepsilon}^S] \nabla \varphi d\Omega - \int_{\Gamma_1} (\varphi'(\mathbf{x}_1) - \vartheta \varphi'(\mathcal{P}\mathbf{x}_1))^T \lambda_e d\Gamma = 0.
 \end{aligned}$$

Let us have a look at the entries corresponding to the mechanical and the electrostatic parts. One can see that the integrals

$$\int_{\Omega} (\mathcal{B} \mathbf{u}')^T [\mathbf{c}^E] \mathcal{B} \mathbf{u} d\Omega \quad \text{and} \quad \int_{\Omega} (\nabla \varphi')^T [\boldsymbol{\varepsilon}^S] \nabla \varphi d\Omega$$

yield the results of a strongly different order of magnitude. This is due to the fact that  $[\boldsymbol{\varepsilon}^S]$  is usually about 20 orders of magnitude smaller than  $[\mathbf{c}^E]$ . But at the same time, the surface integrals containing  $\boldsymbol{\lambda}_m$  and  $\lambda_e$  coincide in their order of magnitude. This leads to ill posed linear systems. As a way out of the situation one can suggest to take the material data into account while determining the Lagrange multipliers. Namely, to use  $\|[\mathbf{c}^E]\| \boldsymbol{\lambda}_m$  and  $\|[\boldsymbol{\varepsilon}^S]\| \lambda_e$  instead of  $\boldsymbol{\lambda}_m$  and  $\lambda_e$ . Here,  $\|\cdot\|$  denotes the Euclidean norm. Another issue typical to the Lagrange multiplier technique is the handling of cross points. In our case they are the nodes on  $\Gamma_1$  where the Dirichlet boundary conditions are imposed, and therefore the solution is already known. A special treatment is required in this case, so as not to come to an overdetermined system of equations. Namely, the number  $N_{\text{LM}}$  of nodal FE basis functions for the Lagrange multipliers is related to the number of elements on  $\Gamma_1$   $N_e$  as  $N_{\text{LM}} = N_e - 1$  [35, 105] (see fig. 3.15).

Another approach introduced by Hansbo *et al.* for composite grids [106] springs from the technique suggested by Nitsche in [107]. It can also be adopted for periodic boundary conditions. In contrast to the Lagrange multipliers method, Nitsche's one does not lead to a saddle point problem. It also keeps the convergence rate of the underlying FEM model [35]. The scheme of Nitsche's method goes on as follows:

- we proceed with the equation (3.13) as before but retain  $\mathbf{T}$  on  $\Gamma_1$ , which yields

$$\int_{\Omega} (\mathcal{D} \mathbf{w}')^T [\mathbf{C}] \mathcal{D} \mathbf{w} d\Omega - \omega^2 \int_{\Omega} (\mathbf{w}')^T [\boldsymbol{\rho}] \mathbf{w} d\Omega - \int_{\Gamma_1} (\mathbf{w}'|_{\Gamma_1} - \vartheta \mathbf{w}'|_{\Gamma_r})^T \mathbf{T}|_{\Gamma_1} d\Gamma = 0; \quad (3.70)$$

- we add the periodic boundary condition (allowed since  $\vartheta \mathbf{w}|_{\Gamma_1} - \mathbf{w}|_{\Gamma_r} = 0$ )

$$- \int_{\Gamma_1} (\mathbf{T}'|_{\Gamma_1})^T (\vartheta \mathbf{w}|_{\Gamma_1} - \mathbf{w}|_{\Gamma_r}) d\Gamma = 0; \quad (3.71)$$

- we add the penalisation term

$$\beta \|\mathbf{C}\| \sum_{E(\Gamma_1)} \frac{1}{h_E} \int_{\Gamma_E} (\mathbf{w}'|_{\Gamma_1} - \vartheta \mathbf{w}'|_{\Gamma_r})^T (\vartheta \mathbf{w}|_{\Gamma_1} - \mathbf{w}|_{\Gamma_r}) d\Gamma = 0. \quad (3.72)$$

In (3.72),  $\beta$  is a constant,  $E(\Gamma_1)$  is a mesh on  $\Gamma_1$ , and  $h_E$  is the diameter of the element  $\Gamma_E \in E(\Gamma_1)$ . The vectors  $\mathbf{T}|_{\Gamma_1}$  and  $\mathbf{T}'|_{\Gamma_1}$  are defined as follows

$$\mathbf{T}|_{\Gamma_1} = \begin{pmatrix} [\boldsymbol{\sigma}] \mathbf{n}_1|_{\Gamma_1} \\ \mathbf{D} \mathbf{n}_1|_{\Gamma_1} \end{pmatrix} = \begin{pmatrix} ([\mathbf{c}^E] \mathcal{B} \mathbf{u} + [\mathbf{e}]^T \nabla \varphi) \mathbf{n}_1|_{\Gamma_1} \\ ([\mathbf{e}] \mathcal{B} \mathbf{u} - [\boldsymbol{\varepsilon}^S] \nabla \varphi) \mathbf{n}_1|_{\Gamma_1} \end{pmatrix}, \quad (3.73)$$

$$\mathbf{T}'|_{\Gamma_1} = \begin{pmatrix} [\boldsymbol{\sigma}'] \mathbf{n}_1|_{\Gamma_1} \\ \mathbf{D}' \mathbf{n}_1|_{\Gamma_1} \end{pmatrix} = \begin{pmatrix} ([\mathbf{c}^E] \mathcal{B} \mathbf{u}' + [\mathbf{e}]^T \nabla \varphi') \mathbf{n}_1|_{\Gamma_1} \\ ([\mathbf{e}] \mathcal{B} \mathbf{u}' - [\boldsymbol{\varepsilon}^S] \nabla \varphi') \mathbf{n}_1|_{\Gamma_1} \end{pmatrix} \quad (3.74)$$

Summing the equations (3.70), (3.71), and (3.72), we come to the following model

$$\begin{aligned} & \int_{\Omega} (\mathcal{D} \mathbf{w}')^T [\mathbf{C}] \mathcal{D} \mathbf{w} d\Omega - \omega^2 \int_{\Omega} (\mathbf{w}')^T [\boldsymbol{\rho}] \mathbf{w} d\Omega \\ & - \int_{\Gamma_1} (\mathbf{w}'|_{\Gamma_1} - \vartheta \mathbf{w}'|_{\Gamma_r})^T \mathbf{T}|_{\Gamma_1} d\Gamma - \int_{\Gamma_1} (\mathbf{T}'|_{\Gamma_1})^T (\vartheta \mathbf{w}|_{\Gamma_1} - \mathbf{w}|_{\Gamma_r}) d\Gamma \\ & + \beta \|\mathbf{C}\| \sum_{E(\Gamma_1)} \frac{1}{h_E} \int_{\Gamma_E} (\mathbf{w}'|_{\Gamma_1} - \vartheta \mathbf{w}'|_{\Gamma_r})^T (\vartheta \mathbf{w}|_{\Gamma_1} - \mathbf{w}|_{\Gamma_r}) d\Gamma = 0. \end{aligned} \quad (3.75)$$

The substitution of (3.15) for  $\mathbf{w}$  in (3.75) yields

$$\left( \underset{\approx}{K} - \omega^2 \underset{\approx}{M} - \underset{\approx}{G} \right) \underset{\approx}{w} = \underset{\approx}{f}, \quad (3.76)$$

where the matrix  $\underset{\approx}{G}$  is defined through the surface integrals in (3.75). The observations on the evaluation of surface integrals that we have made before in this section also remain valid here.

The parameter  $\beta$  should not be too small so that the boundary condition  $\mathbf{w}_r = \vartheta \mathbf{w}_1$  is fulfilled, nor should it be too large so as not to worsen the condition number of the linear system [35]. It is suggested in [35] to take  $\beta = 100$ . The main advantage of Nitsche's method is that it does not introduce additional variables. Nor does it have the cross points issue. The model explicitly takes the material data into account through (3.73), (3.74); therefore, the instabilities as those of the Lagrange multipliers approach do not emerge.

At the same time, Nitsche's method requires more computational efforts. Namely, we need the information about the volume elements adjacent to  $\Gamma_1$  to be able to evaluate the derivatives in (3.73), (3.74) numerically. If such a volume element belongs to the PML domain, the corresponding coordinate stretching is to be applied. These difficulties though do not exceed the advantages of Nitsche's approach. Therefore from now on Nitsche's method is supposed to be used for the incorporation of periodic boundary conditions into the FEM model.

Note that in case of an arbitrary factor of periodicity  $\vartheta$  both Lagrange multipliers and Nitsche's approaches lead to non-symmetric linear systems (3.67) and (3.76). Their symmetry is achievable for a pure periodic boundary conditions  $\vartheta = 1$ . In this case the numerical model coincides with that for non-matching grids [35].

---

## Numerical aspects and model validation

---

### 4.1 Periodic boundary conditions and perfectly matched layer

The numerical model developed in chapter 3 has been implemented within the FE software tool CFS++ (Coupled Field Simulation in C++) [108]. Before we proceed to its application to certain problems, it is necessary to study how the techniques we have brought into the model affect the numerical solution. In the first instance we dwell on Nitsche's method that has been used to incorporate the periodic boundary conditions. In order to validate the numerical solution we can turn to a test problem which admits an exact solution.

Let the system of piezoelectric equations (2.22), (2.23) be given in an infinite 2D strip of the width  $a$ . Let the process be independent of time ( $\partial/\partial t = 0$ ) and no electrical loads be applied ( $\varphi = 0$ ). For the sake of simplicity we choose the elastic stiffness tensor of the following form

$$[\mathbf{c}^E] = \{c^E\}_{i,j} = \begin{cases} 1, & i = j, \\ 0, & i \neq j. \end{cases}$$

Then we arrive at the system of partial differential equations for  $u_x(x, y)$  and  $u_y(x, y)$ ,  $(x, y) \in (-\infty, +\infty) \times (0, a)$

$$\frac{\partial^2 u_x}{\partial x^2} + \frac{\partial^2 u_x}{\partial y^2} + \frac{\partial^2 u_y}{\partial x \partial y} = 0, \quad (4.1)$$

$$\frac{\partial^2 u_x}{\partial x \partial y} + \frac{\partial^2 u_y}{\partial x^2} + \frac{\partial^2 u_y}{\partial y^2} = 0. \quad (4.2)$$

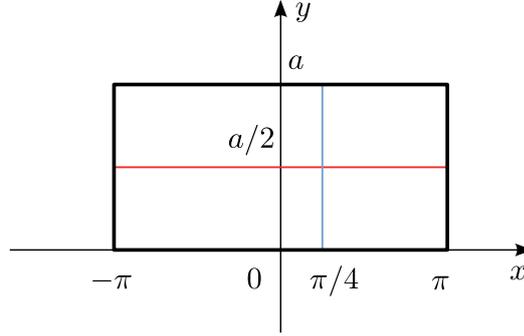


Figure 4.1: To the validation of periodic boundary conditions implementation

Let  $u_x$  and  $u_y$  satisfy the following boundary conditions

$$u_x(x, 0) = u_x(x, a) = 0, \quad (4.3)$$

$$u_y(x, 0) = 0, \quad u_y(x, a) = \sin x. \quad (4.4)$$

This means that  $u_x, u_y$  are periodic with respect to  $x$  with the period  $p = 2\pi$ . We can therefore seek for a numerical solution of the problem in the rectangular domain  $(x, y) \in (-\pi, \pi) \times (0, a)$  (see fig. 4.1) imposing the periodic boundary conditions on its left and right sides with the factor  $\vartheta = 1$ .

In order to find an exact solution we apply the Fourier transform (3.26) in (4.1), (4.2). This yields

$$\begin{aligned} -k^2 u_x + u_x'' - i k u_y' &= 0, \\ -i k u_x - k^2 u_y + u_y'' &= 0. \end{aligned}$$

Introducing  $u_x' = v_x$  and  $u_y' = v_y$  we obtain the system of first order ODEs

$$\begin{pmatrix} u_x' \\ u_y' \\ v_x' \\ v_y' \end{pmatrix} = \begin{pmatrix} 0 & 0 & 1 & 0 \\ 0 & 0 & 0 & 1 \\ k^2 & 0 & 0 & i k \\ 0 & k^2 & i k & 0 \end{pmatrix} \begin{pmatrix} u_x \\ u_y \\ v_x \\ v_y \end{pmatrix} \iff \underline{u}' = \underline{A} \underline{u}.$$

The characteristic equation of the last system reads

$$\det(\underline{A} - \kappa \underline{I}) = \kappa^4 - \kappa^2 k^2 + k^4 = 0.$$

In order to be consistent with the boundary condition  $u_y(x, 0) = \sin x$ , we set  $k^2 = 1$ . Then the roots of the characteristic equation are  $\kappa = \pm (\sqrt{3} \pm i)/2$ . According to the

matrix exponential approach [109], the solution of the problem can be written as follows

$$\underline{u}(y) = \underline{H} e^{\text{diag}(\kappa)y} \underline{H}^{-1} \underline{u}(0).$$

In the equation above  $\underline{u} = (u_x \ u_y \ v_x \ v_y)^T$  and  $\underline{H}$  is the matrix composed of the eigenvectors of  $A$ .

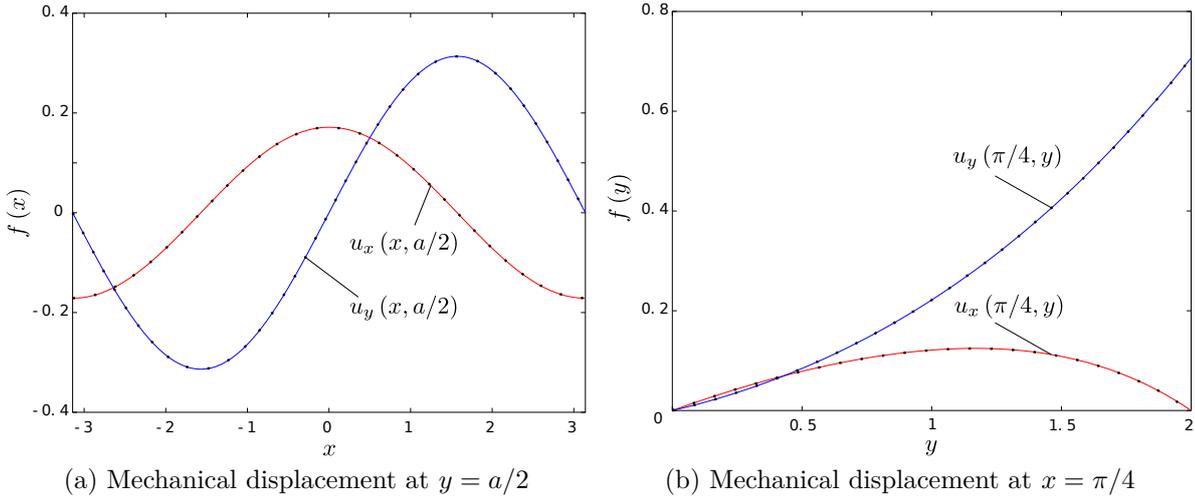


Figure 4.2: To the validation of numerical results

Fig. 4.2 (a) and (b) show the distribution of  $u_x$  and  $u_y$  along the lines  $y = a/2$  and  $x = \pi/4$  (red and blue lines in fig. 4.1) respectively. The solid red and blue curves correspond to the analytical solution for the infinite strip; the dotted ones, to the numerical solution of the problem with the periodic boundary conditions. The mesh used for the numerical computation consisted of triangles with average area about 0.03% of that of the rectangle. The first-order FE basis functions were applied for the approximation of the numerical solution. The difference between the exact and the numerical solution is hardly visible, which proves a well competence of Nitsche's method for periodic boundary conditions. We also note that the results have no apparent difference whether a conforming or a slightly non-conforming mesh is used. This is proven by plots in fig. 4.3 (a) and (b). The dotted red curves are calculated for a conforming mesh on  $\Gamma_l$  and  $\Gamma_r$ . The dashed green and the solid blue curves correspond to meshes with elements on  $\Gamma_l$  twice and four times larger than those on  $\Gamma_r$ , respectively. One can see that the accuracy increases with the regularity of meshes: the green curves are closer to the red ones than the blue curves. At the same time, the difference between the results for conforming and non-conforming meshes is almost insignificant even for the first-order FE approximation.

Another point we shall give attention to is the choice of the PML parameters. We have already discussed the strategy how to select the values  $\sigma_0$  and  $\alpha_0$  of the shifted metric (3.46) in section 3.3. Here we shall study the behaviour of the classic and the

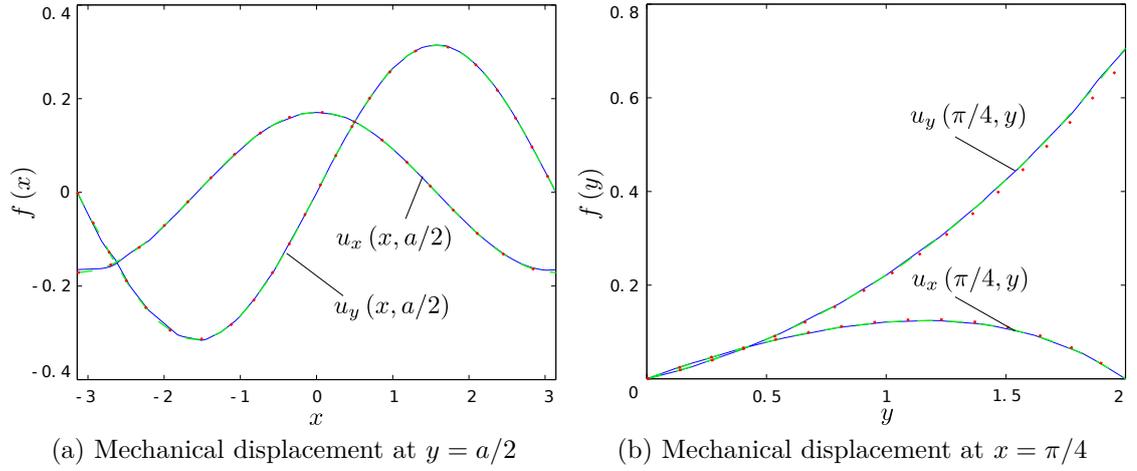


Figure 4.3: Comparison of numerical results for conforming and non-conforming meshes

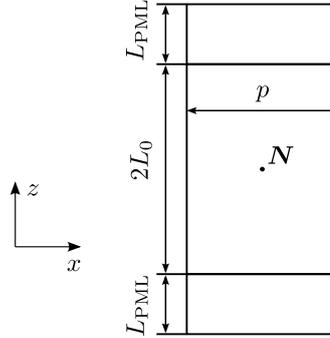


Figure 4.4: Test structure to the study of wave propagation

frequency shifted PML metrics towards the propagation of different types of waves in various media. Our goal is to truncate the computational domain using a PML. Therefore the question is to make the PML as thin as possible lest it disturb the numerical solution.

The structure we use for test simulations is depicted in fig. 4.4. We impose periodic boundary conditions with the factor  $\vartheta = -1$  on its left and right sides. An external force of amplitude  $\mathbf{f} = f_x \mathbf{e}_x$  is applied at point  $\mathbf{N}$ . Two PML layers are added to absorb the waves travelling in  $z$ -direction. We investigate the propagation of waves for two types of materials:

I isotropic with  $c_{11} = 83.29$ ,  $c_{12} = 45.26$ , and  $c_{44} = 19.015$  GPa;

II cubic with  $c_{11} = 83.29$ ,  $c_{12} = 45.26$ , and  $c_{44} = 39.59$  GPa.

For both materials we choose a mass density  $\rho$  of  $5680 \text{ kg/m}^3$ . For the sake of simplicity we solve the problem in 2D for pure mechanical field. The PML parameters  $\sigma_0$ ,  $\alpha_0$  are

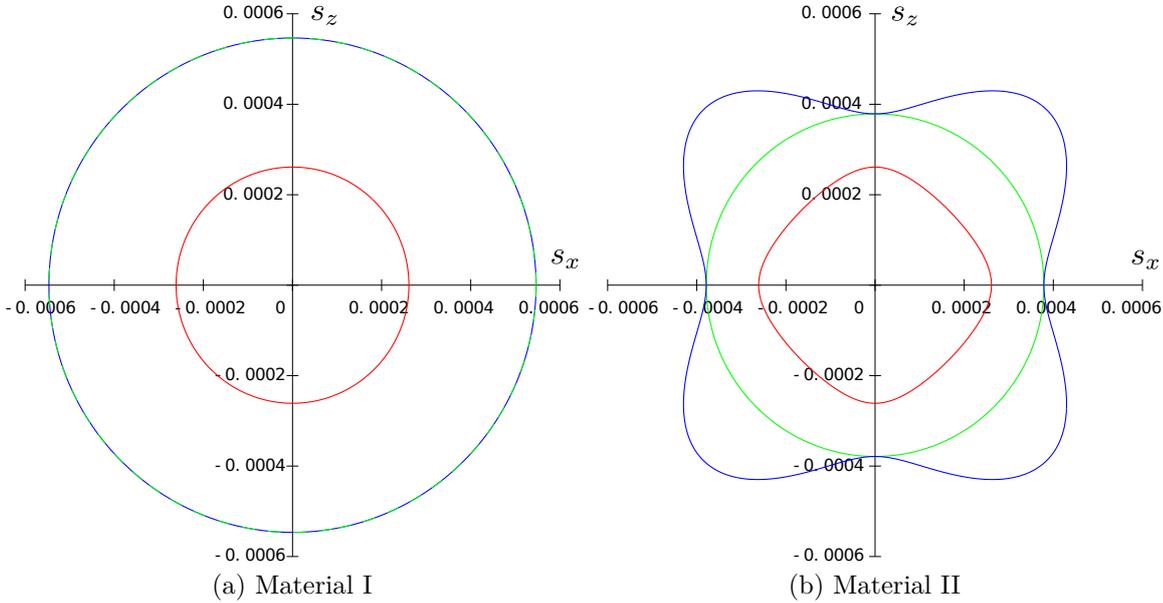


Figure 4.5: Slowness curves for the materials I and II

taken as suggested in section 3.3, and  $\nu_0 = 3$ . Second order basis functions defined on a triangular mesh are used within the FEM computation.

The slowness curves for materials I and II are shown in fig. 4.5 (a) and (b) respectively. One can see that the PML applied in  $z$ -direction is not absolutely stable for material II. The necessary stability condition discussed in section 3.3 is violated for the slownesses  $3.8 \cdot 10^{-4} < |s_x| < 4.3 \cdot 10^{-4}$  s/m.

First, we investigate material I at the slownesses  $s_x^{(1)} = 6 \cdot 10^{-4}$  s/m and  $s_x^{(2)} = 4 \cdot 10^{-4}$  s/m. The first one corresponds to waves that attenuate as  $z \rightarrow \pm\infty$ ; the second one, to waves radiating in  $z$ -direction. The propagation domain is chosen with  $L_0 = 1.25p$ , and the thickness of the PML is  $L_{\text{PML}} = 0.1p$  and  $0.5p$ . Figures 4.6 and 4.7 show the distribution of the  $x$ -component of the mechanical displacement vector along the vertical line  $x = x_N, z \geq z_N$  at the slownesses  $s_x^{(1)}$  and  $s_x^{(2)}$ , respectively. The red curves correspond to the classic PML:  $L_{\text{PML}} = 0.1p$  for the solid ones and  $L_{\text{PML}} = 0.5p$  for the dotted ones. The blue curves in the same manner relate to the frequency shifted PML.

The difference between the solutions obtained using the classic and the shifted PML techniques is hardly remarkable in the domain of propagation. We should have expected such a behaviour towards radiating waves, because the shifted metric gets closer to the classic one as the frequency increases (or the slowness decreases). On the other hand, the classic PML can surprisingly be effective in the damping of attenuating waves. We can suggest an explanation of this fact in the following way. The wave propagates in  $z$ -direction with not a pure imaginary wavenumber  $k_z$ , which is seen from fig. 4.6. Therefore the initial damping factor gets increased owing to the transformation (3.45). Another

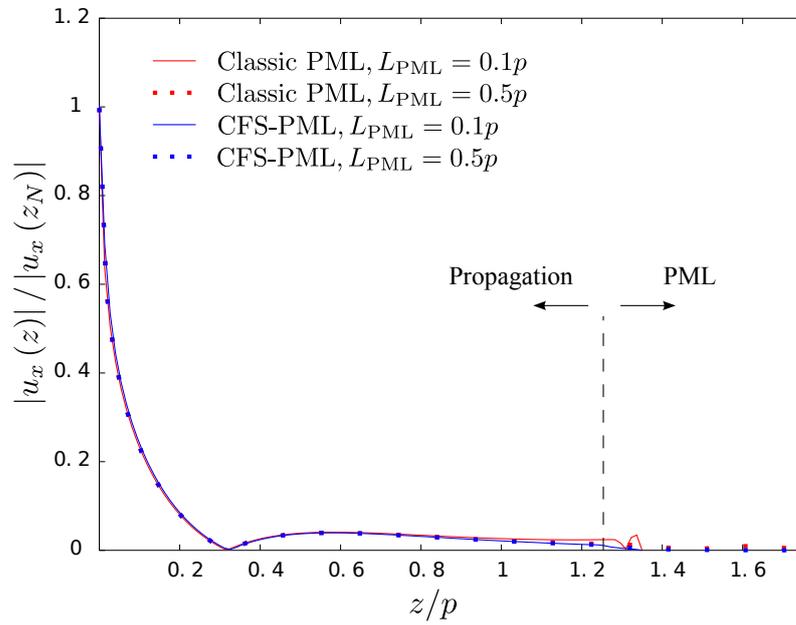


Figure 4.6: Propagation of evanescent waves in material I at  $s_x = 6 \cdot 10^{-4}$  s/m

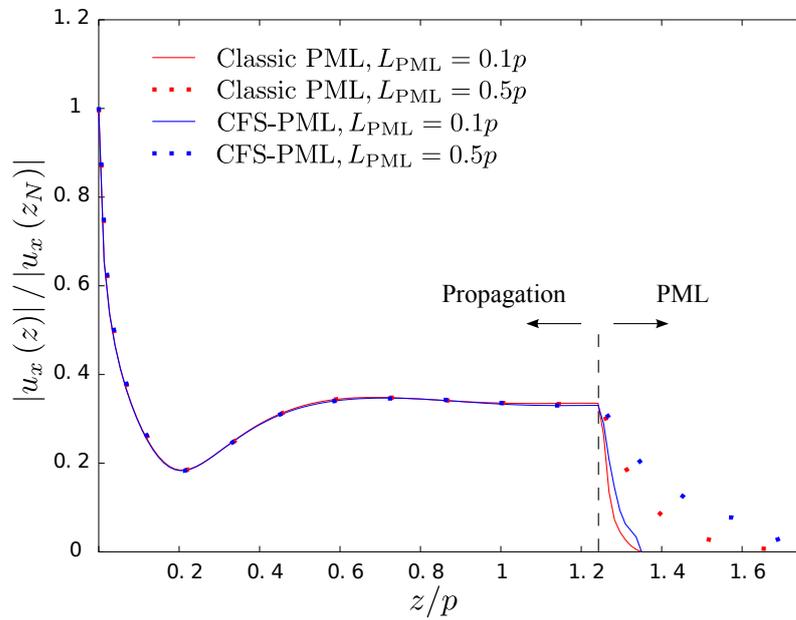


Figure 4.7: Propagation of radiating waves in material I at  $s_x = 4 \cdot 10^{-4}$  s/m

point is that the homogeneous Dirichlet boundary conditions imposed to truncate the solution cause a reflecting wave. Being interacted with the incident wave it can lead to a reduction of the resulting amplitude. However, this interaction can only be significant if the waves impinge upon the interface between the propagation and the PML domains at right angle.

The situation changes considerably if the material is anisotropic. The distributions of  $u_x$  along the same vertical line for material II are depicted in fig. 4.8 and 4.9. Fig. 4.8 corresponds to the slowness  $s_x = 6 \cdot 10^{-4}$  s/m<sup>3</sup> when, as in the previous example, the waves attenuate as  $z \rightarrow \pm\infty$ . Now, the classic PML is unable to give an adequate numerical solution in the domain of propagation. Note that increasing of PML thickness from  $0.1p$  to  $0.5p$  does not improve the accuracy of the solution. Conversely, the shifted PML leads to feasible results regardless of the layer thickness. The propagation of radiating waves is well affected by both approaches: there is no important difference in the solution shown in fig. 4.9 for  $s_x = 3 \cdot 10^{-3}$  s/m. These two examples demonstrate the advantages of the frequency shifted PML technique over the classic one. Though we remind that both procedures remain valid as long as the necessary stability condition holds.

Previously we mainly discussed how the type of PML formulation affects the solution in the domain of propagation. But we did not dwell on the choice of the layer thickness. From the examples above it seems that the thickness of the PML has a little influence on the solution. Unfortunately, it is not always the case. Let us refer to material II and solve the problem for the slowness  $s_x = 4.35 \cdot 10^{-4}$  s/m. This value is quite close to those where the stability condition is violated. The calculated profiles of  $u_x$  are shown in fig. 4.10. The curves correspond to different thicknesses of the PML:  $L_{\text{PML}} = 0.1p$  (red),  $0.5p$  (green),  $1.25p$  (blue),  $2.0p$  (cyan). It is clear that the thinnest PML does not provide a satisfactory accuracy of the solution. If the classic PML formulation is used, the results become even worse than those at  $s_x = 6 \cdot 10^{-4}$  s/m, though there certainly is a radiating part in the solution (see fig. 4.10) which should ensure the damping in the PML domain.

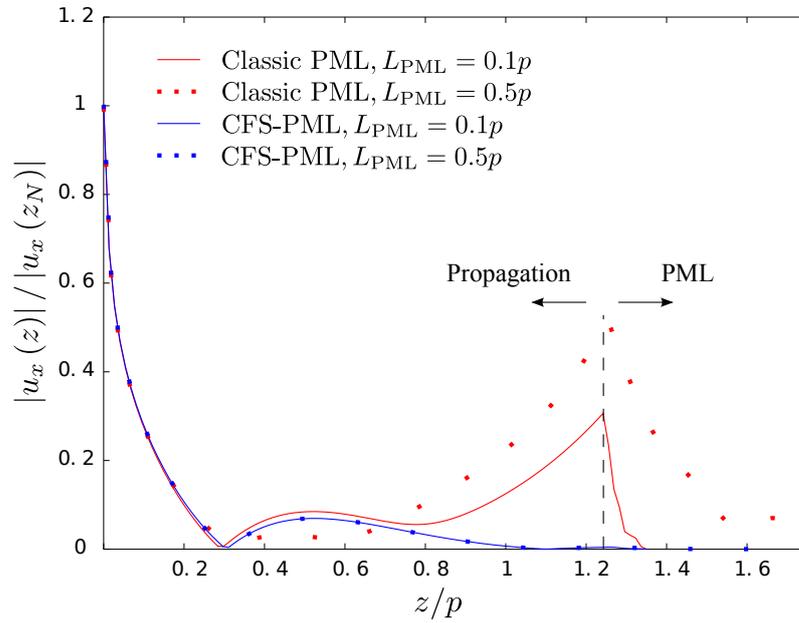


Figure 4.8: Propagation of evanescent waves in material II at  $s_x = 6 \cdot 10^{-4}$  s/m

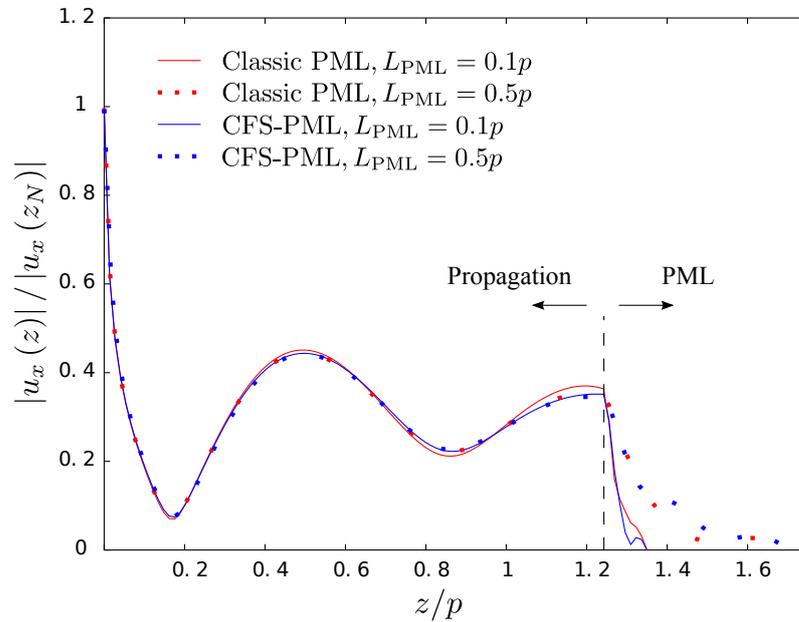


Figure 4.9: Propagation of radiating waves in material II at  $s_x = 3 \cdot 10^{-4}$  s/m

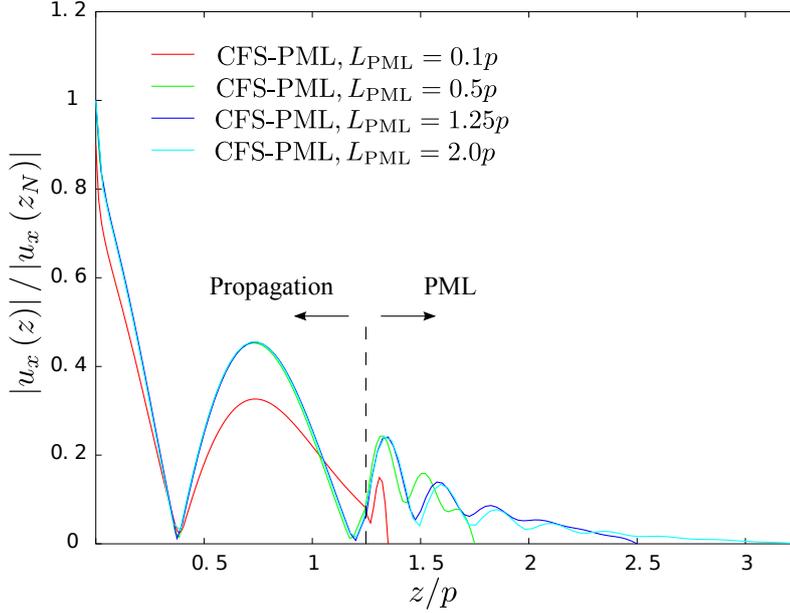


Figure 4.10: Evanescent wave in material II vs. different thickness of PML at  $s_x = 4.35 \cdot 10^{-4}$  s/m

## 4.2 Surface acoustic waves in piezoelectric substrates under periodic electrode gratings

In this section, we shall study the propagation of waves in infinitely long periodic piezoelectric structures. We utilize the model for a unit cell that has been developed in the previous chapter. Once a proper reduction of the computational domain has been applied, we are able to solve the system (3.75) for the mechanical displacement  $\mathbf{u}$  and the electric potential  $\varphi$ . After that, we compute the total electric charge  $q_e$  distributed over the electrode surface  $\Gamma_e$

$$q_e = \int_{\Gamma_e} D_n d\Gamma = \int_{\Gamma_e} ([\mathbf{e}]\mathcal{B}\mathbf{u} - [\boldsymbol{\varepsilon}^S]\nabla\varphi) \cdot \mathbf{n} d\Gamma$$

and thereby obtain the harmonic admittance of the device (1.33) in the following form

$$Y(f, \delta) = \frac{i\omega}{V} \int_{\Gamma_e} D_n(f, \delta) d\Gamma. \quad (4.5)$$

Here, we focus on the validation of the developed model. All the simulations will be performed for a 2D unit cell. We use triangular mesh with 2<sup>nd</sup> order FE basis functions. The unknowns are the full mechanical displacement vector  $\mathbf{u}(x, z) = (u_x, u_y, u_z)$  and the electric potential  $\varphi(x, z)$ , which corresponds to the so called 2.5D formulation. The unit cell is supposed to have one electrode with the metallisation ratio  $\eta = 0.5$  and the

periodicity factor  $\vartheta = -1$ . Such a structure models an infinitely long single electrode IDT with the wavelength  $\lambda = 2p$ .

In our first example we consider the propagation of waves in  $YZ$ -LiNbO<sub>3</sub><sup>1</sup> substrate under an aluminium periodic electrode grating with various relative thickness of the electrodes. This cut exhibits Rayleigh wave solutions; therefore, the mechanical displacements and the electric potential attenuate with the depth of the substrate. We regard  $\dim_z(\cdot)$  as the size of the corresponding domain with respect to the  $z$ -coordinate, which is further referred to as the thickness, and perform the simulations for the following cases:

A.  $\dim_z(\Omega_{\text{PML}}) = 0.5\lambda$ ;

B.  $\dim_z(\Omega_{\text{PML}}) = 1\lambda$ ;

C.  $\dim_z(\Omega_{\text{PML}}) = 2\lambda$

with  $\dim_z(\Omega_{\text{sub}}) = 1.5\lambda$  and  $h/\lambda = 1.75\%$ . The admittance curves are depicted in fig. 4.11, where  $v_f = 3487.3$  m/s is the velocity of SAW on the free surface [29]. The red, green, and blue curves correspond to cases A, B, and C respectively. Since we observe the propagation of surface waves, it is possible to talk about a reference solution here. The last is computed for a sufficiently large computational domain without a PML. The black curve in fig. 4.11 gives the admittance obtained from the reference solution for  $\dim_z(\Omega_{\text{sub}}) = 5\lambda$ . It is seen that the coloured curves are close not only to one another but also to the black one, which indicates a high accuracy of the developed FEM/PML approach. Fig. 4.12 (a), (b) show the distribution of  $\mathbf{u}$  and  $\varphi$  along the sagittal line of the unit cell within the depth of  $1.5\lambda$  in cases A and B respectively (red curves). The curves are put side by side with the blue ones that correspond to the reference solution. One can see a quite good agreement of the red curves with the reference solution, especially within the region near the interface between the electrode and the substrate.

In order to demonstrate the effectiveness of the model for simulation of multi-layered structures, we take the example considered in [111]. A single electrode IDT contains an electrode grating of 80 nm thick and 200 nm wide gold electrodes and a double-layered GaN/Silicon substrate. The GaN layer is 1.2  $\mu\text{m}$  thick. The electric period of the grating  $\lambda = 0.8$   $\mu\text{m}$ . The harmonic admittance curve calculated for this configuration is shown in fig. 4.13 in blue colour. The red curve used as a reference has been obtained for the same structure exploiting a proprietary FEM/BEM tool DESMA © developed by IMTEK (Freiburg, Germany) and CTR AG. The resonant peaks of both curves are at the same places, which again confirms a high precision of the developed model. The profiles of the mechanical displacement amplitude at the resonances are to be seen in fig. 4.14. Interestingly, the admittance curve obtained in [111] using the FE package COMSOL Multiphysics ® differs from those depicted in fig. 4.13. Although the right resonant peak calculated in [111] equals 5.804 GHz, which is close to our 5.785 GHz, the

---

<sup>1</sup>The material parameters are taken from [110]

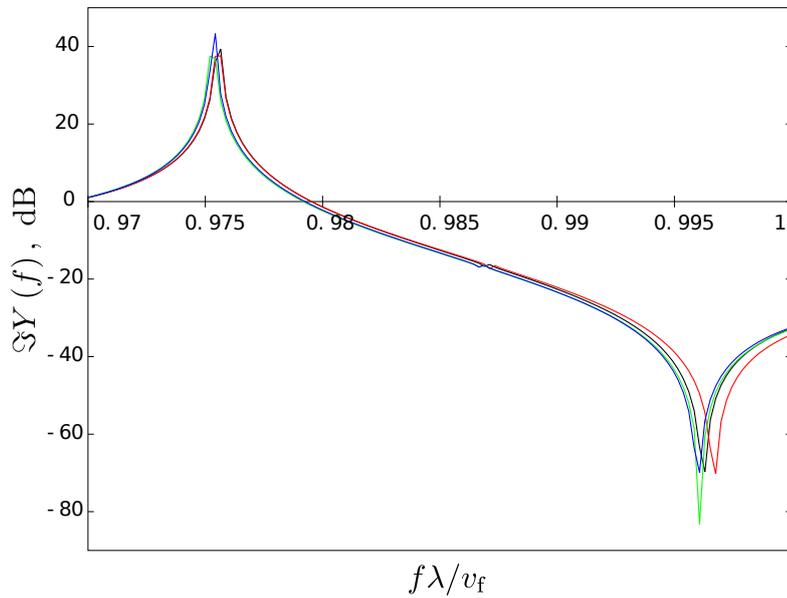


Figure 4.11: Admittance of an infinite periodic transducer on  $YZ$ -LiNbO<sub>3</sub> substrate for cases A (red), B (green), C (blue), and the reference case (black)

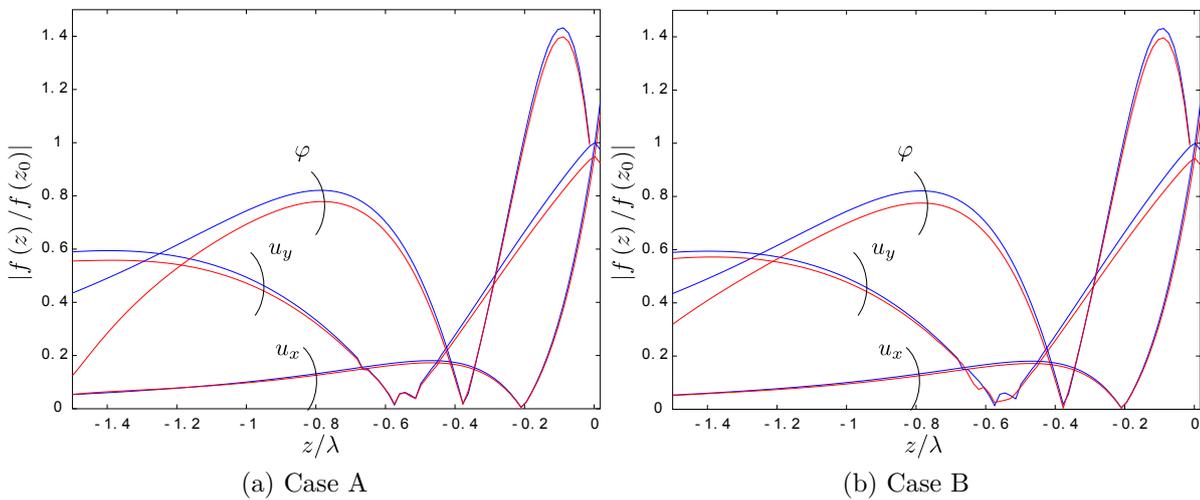


Figure 4.12: The distribution of the mechanical displacement and the electric potential in  $YZ$ -LiNbO<sub>3</sub> substrate along the middle line. The quantities are normalised to the corresponding values of the reference solution at the interface (meant as  $z = z_0$ )

4.2 Surface acoustic waves in piezoelectric substrates under periodic electrode gratings

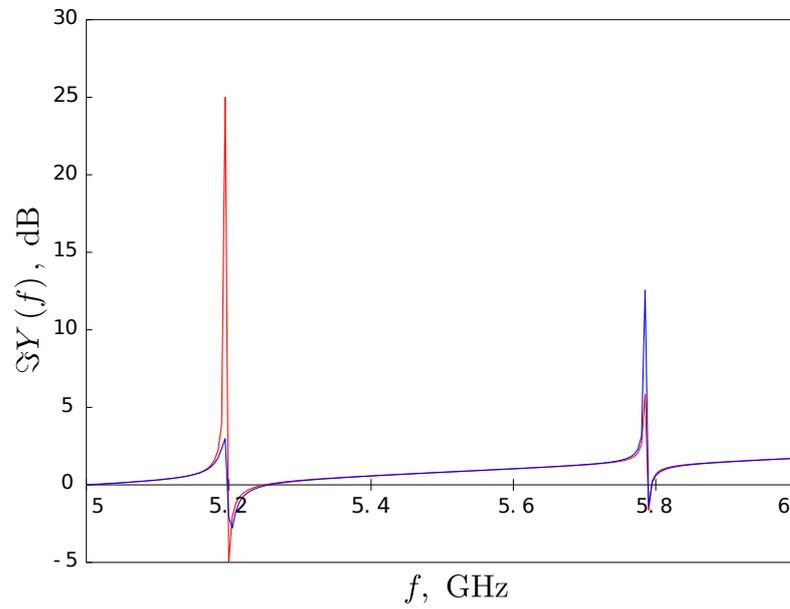


Figure 4.13: Admittance calculated for the gold electrode IDT placed on GaN/Silicon substrate using FEM/PML (blue) and FEM/BEM (red) approaches

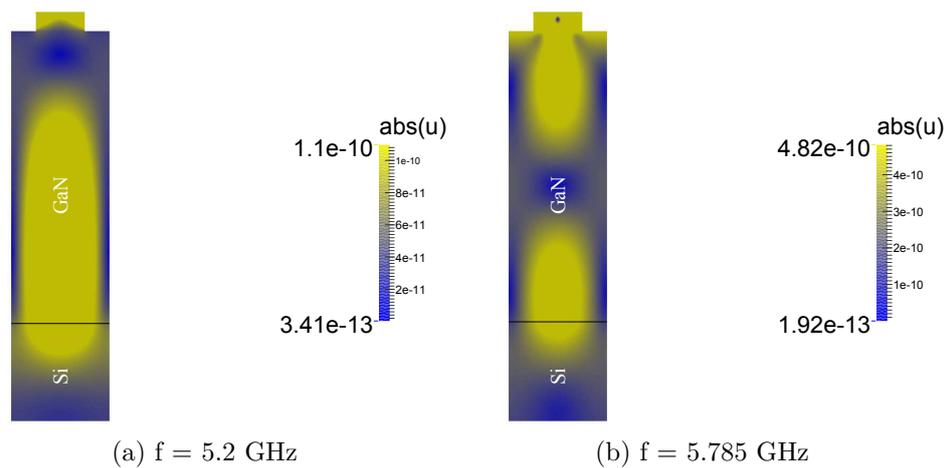


Figure 4.14: Admittance calculated for the gold electrode IDT placed on GaN/Silicon substrate using FEM/PML (blue) and FEM/BEM (red) approaches

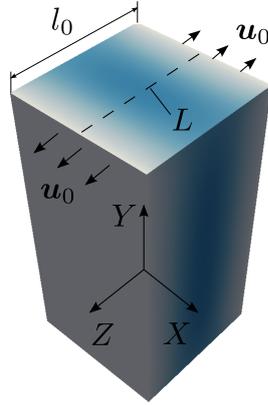


Figure 4.15:  $YZ$ -LiNbO<sub>3</sub> crystal subjected to a static uniform deformation  $\mathbf{u}_0$

left one is located at 5.47 GHz. Still we can not conclude that the results in [111] were undoubtedly wrong, because not all the material data used for simulations were given in the paper.

Finally, we turn to the simulation of waves in piezoelectric media subjected to preliminary deformations. Mechanical strains applied to a SAW device causes a variation of the velocity of SAW. This effect has been used as the working principle of SAW strain sensors and has been well studied both experimentally and numerically for many piezoelectric crystals. The dependence of SAW velocity on strains can be expressed as follows [112]

$$v(S) = v_0(1 + \gamma S), \quad (4.6)$$

where  $v_0$  is SAW velocity in a reference device that operates without external mechanical loads. The strain coefficient of the velocity  $\gamma$  can be then derived from the fractional velocity change  $\gamma S = \Delta v/v_0$ . The last is obtainable through simulations done for a unit cell with material data modified according to the applied mechanical deformation. Experimental studies of strain effects are usually based on measurements of the phase difference between the input and the output signals [47]

$$\frac{\Delta\psi}{\psi_0} = S_1 - \frac{\Delta v}{v_0} \quad (4.7)$$

or the variation of the oscillator frequency [113, 114]

$$\frac{\Delta f}{f_0} = \frac{\Delta v}{v_0} - S_1$$

caused by the elongation  $S_1 = \Delta l/l_0$  of the effective resonator length in the direction of wave propagation.

We shall study the effect of preliminary deformations on the propagation of SAW

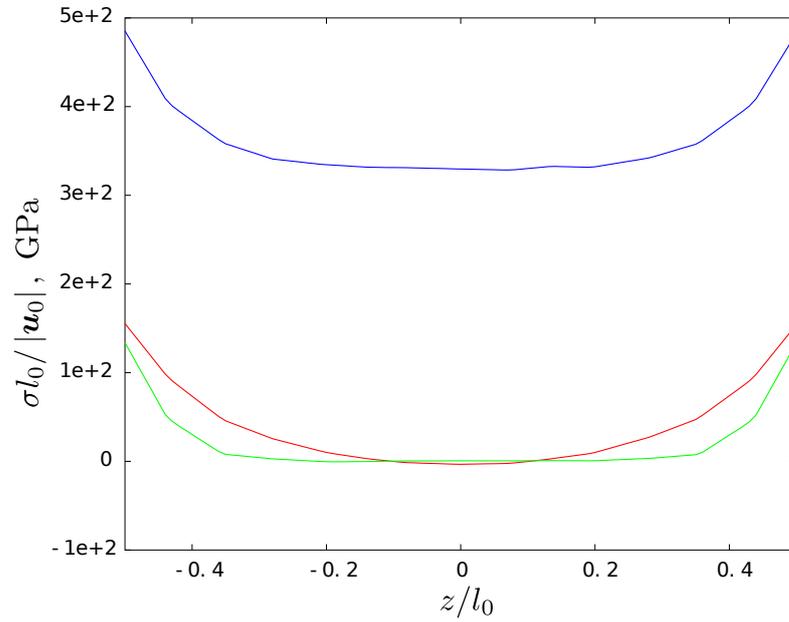


Figure 4.16: Stress distribution on the top of the hexahedral  $YZ$ - $\text{LiNbO}_3$  crystal along the line  $L$

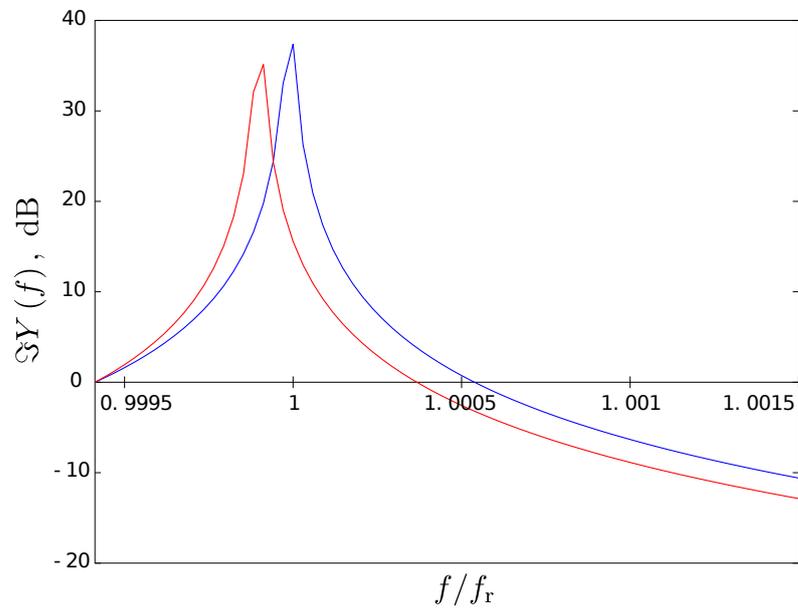


Figure 4.17: Shift in the resonant frequency of prestressed (red) and reference (blue)  $YZ$ - $\text{LiNbO}_3$  crystals in case  $S_1 = 400$

in  $YZ$ -LiNbO<sub>3</sub> crystal utilising the two-step model developed in section 2.4. First, we consider a uniform static deformation applied in  $z$ -direction to the opposite sides of a hexahedral structure made of  $YZ$ -LiNbO<sub>3</sub> as shown in fig. 4.15. The distributions of mechanical stress along the line  $L$  gained from the static analysis are depicted in fig. 4.16. This stress will be used at the second step of the model as  $[\sigma_1]$  in (2.45). Neglecting the edge effects and assuming that  $[\sigma_1]$  is uniform in  $z$ -direction, we apply the unit cell approach in order to derive the strain coefficient of velocity. Fig. 4.17 shows the shift of the resonant frequency of an IDT for a preliminary deformation  $\mathbf{u}_0$  that causes the elongation  $S_1 = 400 \text{ } \mu\text{m/m}$  in  $z$ -direction.

The second order elastic constants for LiNbO<sub>3</sub> used to define the tensor of effective elastic moduli have been taken from [56]. The value of the strain coefficient of velocity obtained from simulations is  $\gamma_z = -0.2922$ . The value extracted by measurements and mentioned in [113] was  $\gamma_z = -0.28$ , which is quite close to that we have gained. Moreover, according to (4.7) we have

$$\frac{\Delta\psi}{\psi_0} = S_1(1 - \gamma_z) = 1.2922S_1.$$

At the same time, the phase shift measured in [47] was  $\Delta\psi/\psi_0 \approx 1.28S_1$ . These results show that the developed two-step approach is adequate for simulations of waves in prestressed piezoelectric crystals.

### 5.1 Dispersion curves and stop-band analysis

In the previous section we have touched upon the derivation of the harmonic admittance from FE simulations in order to validate our approach. In this section we keep on with the harmonic admittance (HA) analysis of periodic transducers. It is applied here to establish the edges of the stop-bands of a SAW transducer for short-circuited (SC) and open-grating (OG) operating modes. Hence, we gain the frequencies  $f_r$ ,  $f_a$ , and  $f_c$  and thereby extract the desired COM parameters following the way described in chapter 1.

Still we should note that the dispersion curves and therefore the COM parameters are sometimes not directly obtainable from fitting techniques. One could already identify from fig. 4.11 and 4.13 the resonant and the anti-resonant frequencies for the corresponding structures. Those frequencies are clearly visible as the points where the harmonic admittance has its singularities and roots respectively. As we have mentioned in section 2.1, each one determines an edge of the stop-band for the corresponding mode. However, the dispersion relation requires the knowledge of two stop-band edges. The third characteristic frequency  $f_c$  which determines the second edge of the stop-bands is not discernible on the curves in fig. 4.11 and 4.13.

A way out of this situation can be found in the shifted voltage model proposed in [30]. The essence of the model is to use the voltage in the form (1.29) setting a small non-zero  $\delta \neq 0$ . This leads to a detuning of the periodicity of the structure. Namely, instead of  $\vartheta = -1$  we shall have  $\vartheta = -e^{i2\pi\delta}$ . Solving the problem with such a factor, we find the third characteristic frequency  $f_c$ .

We simulate the propagation of SAW on the surface of  $YZ\text{-LiNbO}_3$  substrate under a periodic Al single electrode grating with the same  $h/\lambda$  as in section 4.2. The admittance curves calculated for  $h/\lambda = 0\%$  with and without a detuning are depicted in 5.1. The

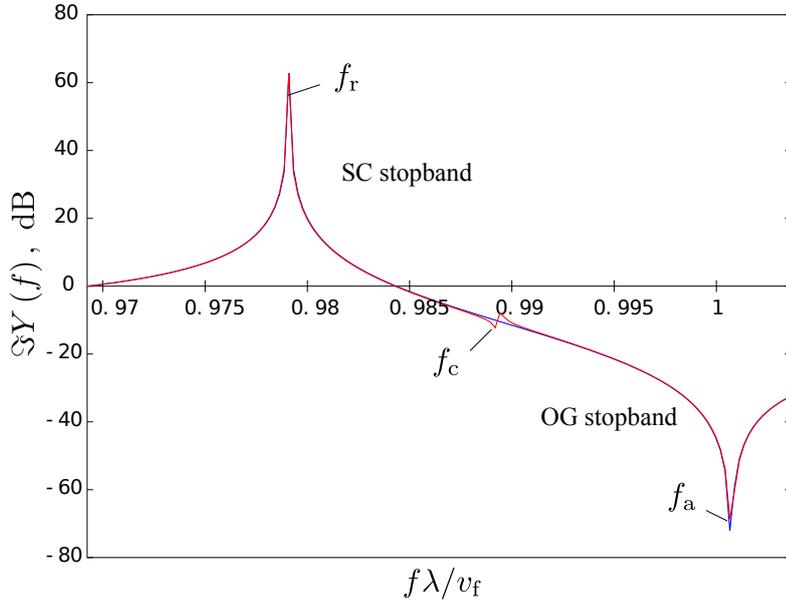


Figure 5.1: Admittance curves calculated for  $\delta = 0$  (blue) and  $\delta = 2.5 \cdot 10^{-4}$  (red) with the relative electrode height  $h/\lambda = 0\%$

Table 5.1: COM parameters obtained for YZ-LiNbO<sub>3</sub> at  $h/\lambda = 0\%$

Parameter	$v_{\text{SAW}}$ , m/s	$ \kappa_p $ , %	$\zeta_n^2/C_n$ , m/s
Our approach	3432	3.29	730
[30]	3432	3.23	700

frequency  $f_c$  is visible on the red curve where a non-zero detuning has been applied. As seen in fig. 5.1, it is unable to locate it on the blue curve obtained for the pure periodic structure. It is clear from fig. 5.1 that the stop-bands are located in the manner shown in fig. 1.1, (b) in this case.

The dispersion curves for the short-circuited mode  $\Delta^{\text{SC}}$  derived from the FEM/PML model are depicted in fig. 5.2. The red, green, and blue curves correspond to the electrodes with relative height  $h/\lambda = 0\%$ ,  $1\%$ , and  $2.5\%$  respectively. The dispersion curves obtained in [30] using the FEM/BEM approach are shown fig. 5.3. Comparing both sets of curves, one can see a good agreement between FEM and FEM/BEM. This is also confirmed by the COM parameters which we extract through the harmonic admittance analysis (4.5) and fitting techniques. In case  $h/\lambda = 0\%$  the velocity of SAW  $v_{\text{SAW}}$  (1.24) and the reflection coefficient  $|\kappa_p|$  (1.25) differ very slightly from those obtained in [30] (see table 5.1). However, the ratios between the normalised transduction parameter  $\zeta_n$  and the normalised capacitance  $C_n$ <sup>1</sup> calculated according to (1.26) show some disparity.

<sup>1</sup>The normalised parameters are calculated according to [25]

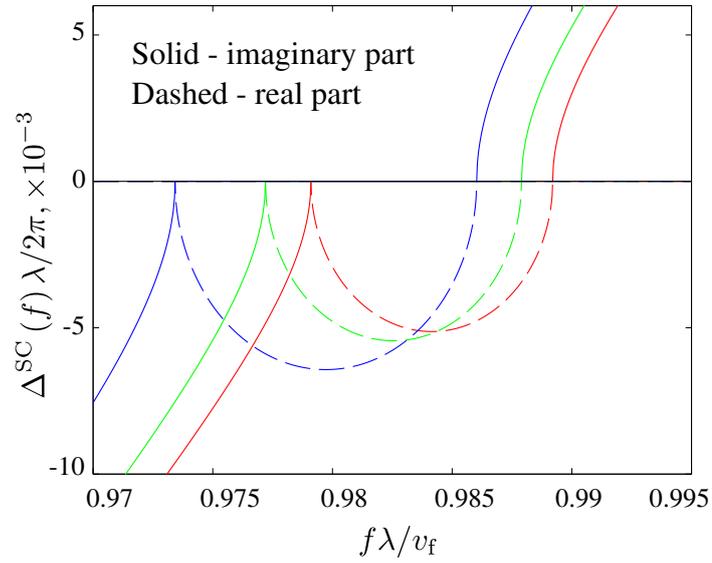


Figure 5.2: Dispersion curves of an infinite periodic transducer on  $YZ$ - $\text{LiNbO}_3$  substrate with the relative thickness of the electrodes  $h/\lambda = 0\%$  (red),  $1\%$  (green), and  $2.5\%$  (blue)

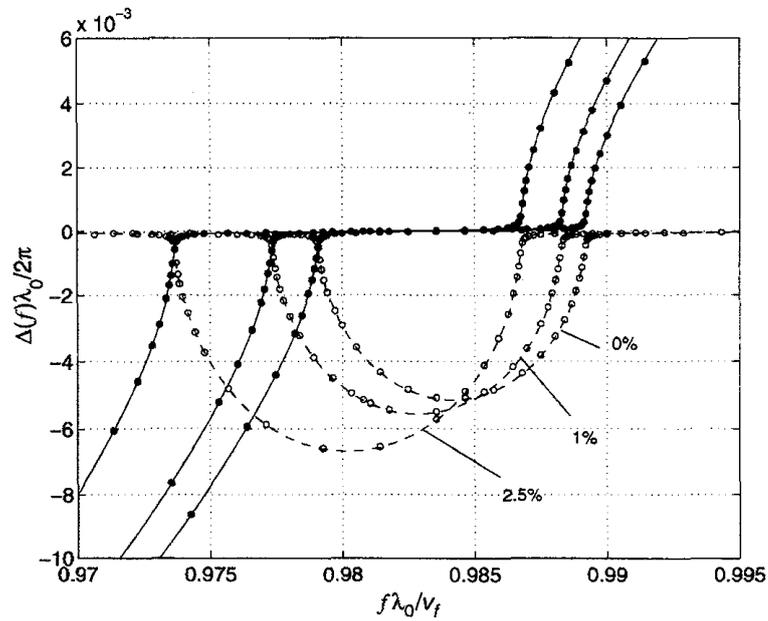


Figure 5.3: Dispersion curves obtained in [30] for an infinite periodic electrode grating (Al) on  $YZ$ - $\text{LiNbO}_3$  with the same relative thickness of the electrodes as in fig. 5.2

Table 5.2: Resonant frequency vs. temperature shift

Temperature $\Delta\tau$ , °C	0	1	2.5	5	10
Relative frequency change $\Delta f_r/f_r^0$ , ppm	0	-8.781	-23.416	-46.832	-90.736
TCF, ppm/°C	—	-87.809	-93.663	-93.663	-90.736

## 5.2 Determination of temperature coefficient of frequency

In section 2.4 we have mentioned that temperature effects on the propagation of SAW can be taken into account through the temperature coefficients for material constants. Temperature coefficients TCF and TCD are known for a large number of piezoelectric materials and therefore can be used as reference values in order to validate the simulation results. We consider here  $YZ$ -LiNbO<sub>3</sub>-substrate with the material data and the thermal expansion coefficients as reported in [43, 45]. We restrict ourselves to zero- and first-order parameters with respect to temperature with the first ones given at the reference temperature  $\tau_0 = 25$  °C. The SAW is generated by a single-electrode periodic with massless electrodes ( $h/\lambda = 0$ ). The metallisation ratio is  $\eta = 0.5$ .

We make simulations for  $\Delta\tau = \tau - \tau_0 = 0, 1, 2.5, 5,$  and  $10$  °C and estimate the shift in the resonant frequency. The calculated values of relative resonant frequency change  $(f_r - f_r^0)/f_r^0 = \Delta f_r/f_r^0$  versus  $\Delta\tau$  are listed in table 5.2 and shown graphically in fig. 5.4. The frequency  $f_r^0$  corresponds to that obtained for the reference temperature. The red dots in fig. 5.4 correspond to the values extracted from simulations. The blue line gives their linear regression in the form

$$\frac{\Delta f_r}{f_r^0}(\Delta\tau) = -9.1021 \cdot 10^{-5} \Delta\tau.$$

Comparing the values of TCF from table 5.2 with the reference  $\text{TCF}_{\text{ref}} = -94$  ppm/°C reported in [1, 43], one can find the best agreement for  $\Delta\tau = 2.5$  and  $5$  °C. At the same time, the linear regression gives the result not far from  $\text{TCF}_{\text{ref}}$ : the relative error between them does not exceed 3.2 %. The disparity can be due to material parameters of lithium niobate: the zero-order constants reported in [45] give the velocity of SAW propagating on a free surface of  $YZ$ -cut equal 3501.2 m/s, whereas the same velocity mentioned in section 5.1 was equal to 3487.3. Therefore, we can conclude that the simulations yield feasible results for TCF.

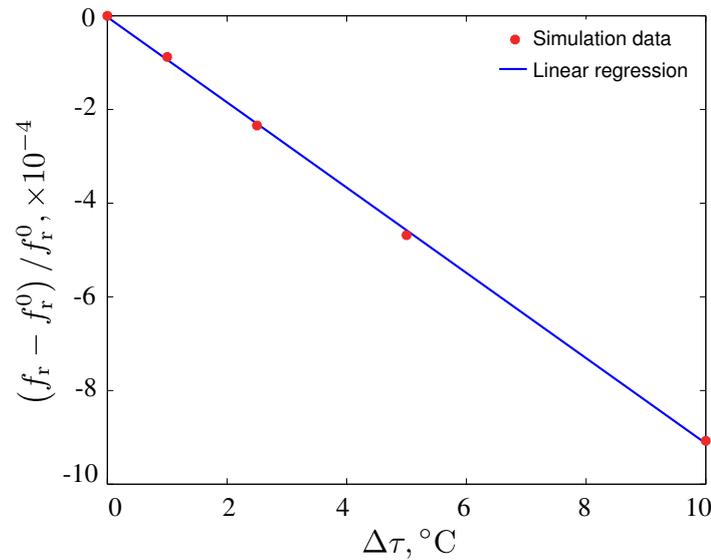


Figure 5.4: Dependence of relative resonant frequency on temperature for  $YZ$ -LiNbO<sub>3</sub>

### 5.3 Lithium niobate crystal on steel blade subjected to longitudinal strain

Finally, we shall investigate the strain sensitivity of a  $YZ$ -cut of a lithium niobate crystal glued to a stainless steel blade. The blade is in its turn subjected to a longitudinal deformation. The crystal can be glued to the blade in an arbitrary way such that the direction of SAW propagation and the deformation applied to the blade make up an angle  $\alpha$  (see fig. 5.5, (a)). The last can obviously lie within the range  $[0^\circ, 90^\circ]$ . The experimental analysis of this setup done at CTR AG had the goal to study how the orientation of the crystal with respect to the deformation direction affects the propagation of SAW. The role of the developed numerical model is to help validate the experimental results.

The experimental setup is depicted in fig. 5.5, (b). The crystal (in green) is located in the middle of the blade. The dimensions of the blade and the crystal are  $140 \text{ mm} \times 15 \text{ mm} \times 1 \text{ mm}$  and  $8 \text{ mm} \times 1.6 \text{ mm} \times 0.5 \text{ mm}$  respectively. An IDT and a reflective delay line are applied to the crystal, and the phase difference between the incident and the reflected waves is measured. The results of measurements are displayed in fig. 5.6 for different orientations of the crystal. It is remarkable that the slope of the sensitivity curves changes its sign from positive to negative as the angle  $\alpha$  rises from  $0^\circ$  to  $90^\circ$ . This ensures the existence of a strain-insensible position which, according to the measurements, corresponds to the angle about  $60^\circ$ . A possible practical application based on this phenomenon is the use of such a setup for temperature sensing. Indeed, heating leads to volume extensions and therefore to strains in the bodies. The strain-insensible positions of the crystal allow us to deliver the results from the extraneous influence of the strain and to concentrate on temperature effects only. It is therefore of

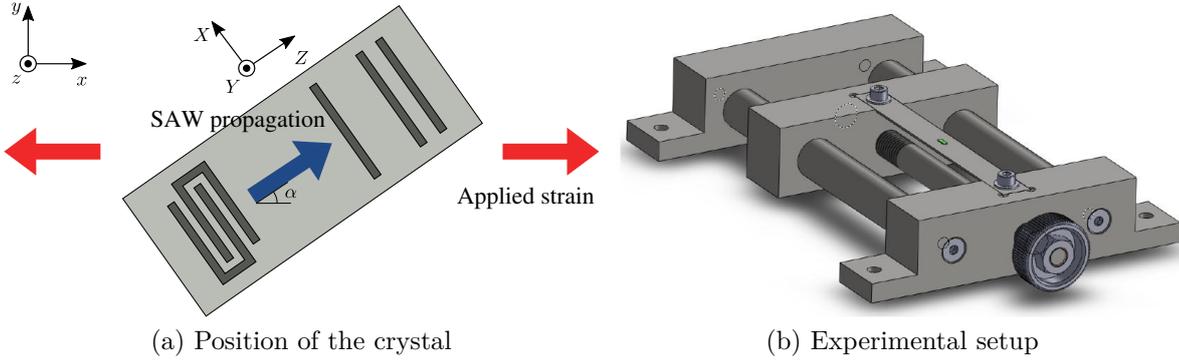


Figure 5.5: Experimental setup

a high importance to compare the results of the experiments with those obtained from simulations.

We make simulations considering the smallest (I) and the largest (II) possible values of  $\alpha$  and perform the two-step analysis from section 2.4. First, we consider the static deformation of the structure caused by the longitudinal strain. The Cartesian coordinate systems depicted in fig. 5.5 (a) are associated with the blade (lower-case) and with the crystal principal axes (upper-case). The longitudinal strain therefore corresponds to  $S_x$ . The glue used to stick the crystal to the blade is neglected during the simulations. The deformation profile and the mechanical displacement distribution near the crystal at  $S_x = 10^{-3}$  m/m are shown in fig. 5.7 for case I. The stress distributions along the middle line parallel to the SAW propagation on the crystal's top are shown in fig. 5.8 (a) and (b) for cases I and II respectively. For the second step we use the extracted values of the stress neglecting the edge effects. Namely, the stress distribution is taken uniform over the whole crystal with the same value as that at the centre point of the crystal's top surface. The values of SAW velocity  $v_{\text{SAW}}$  according to (1.24) are listed in Table 5.3. In addition, the values of the strain  $S_Z^2$  in the direction of SAW propagation are provided.

Table 5.3: SAW velocities extracted from simulations

State	Non-deformed	Setup I	Setup II
SAW velocity $v_{\text{SAW}}$ , m/s	3422.1	3421.5	3422.3
Strain $S_Z$ , m/m	0	$6.0371 \cdot 10^{-4}$	$-2.0402 \cdot 10^{-4}$

The relative velocities for the setups I and II are

$$\left. \frac{\Delta v}{v} \right|_{\text{I}} = -1.7533 \cdot 10^{-4}, \quad \left. \frac{\Delta v}{v} \right|_{\text{II}} = 5.8444 \cdot 10^{-5}.$$

<sup>2</sup>Also calculated at the centre point on the crystal's top.

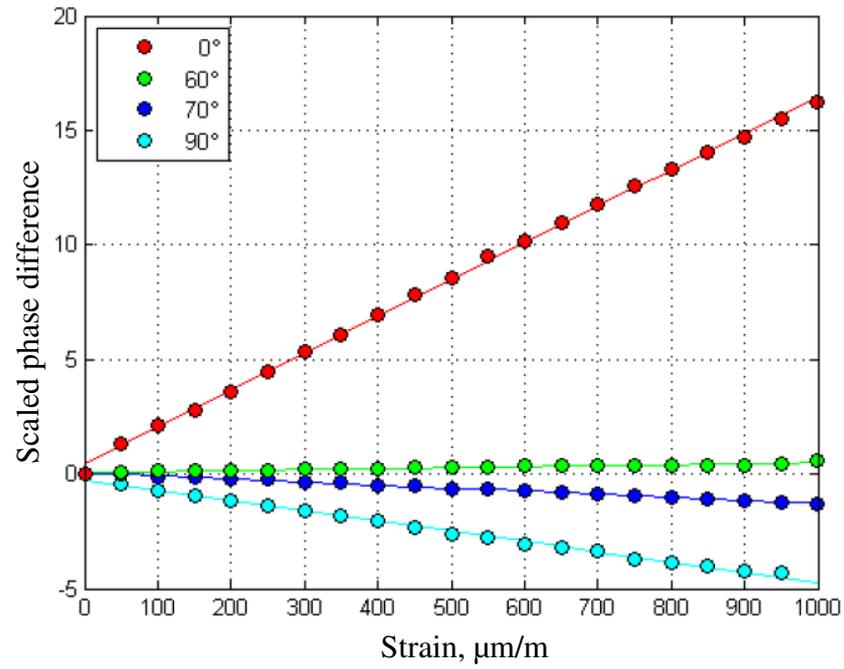


Figure 5.6: Results of the measurements done for different orientations of the crystal [115]

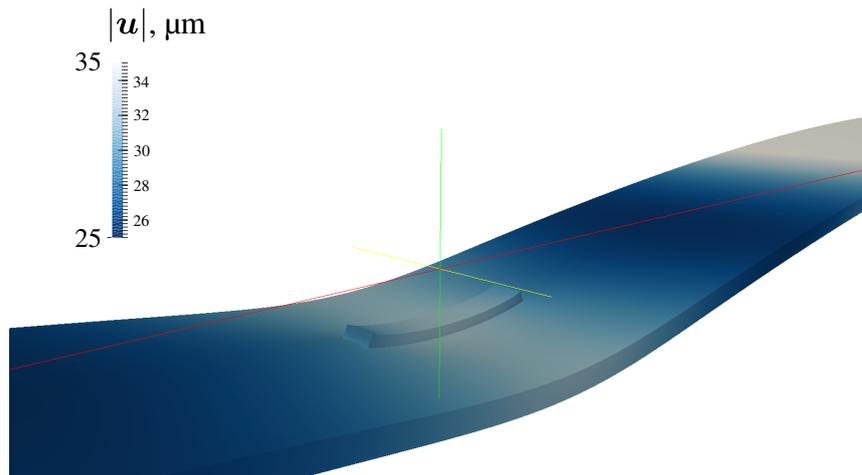


Figure 5.7: Static deformation of the structure in case I

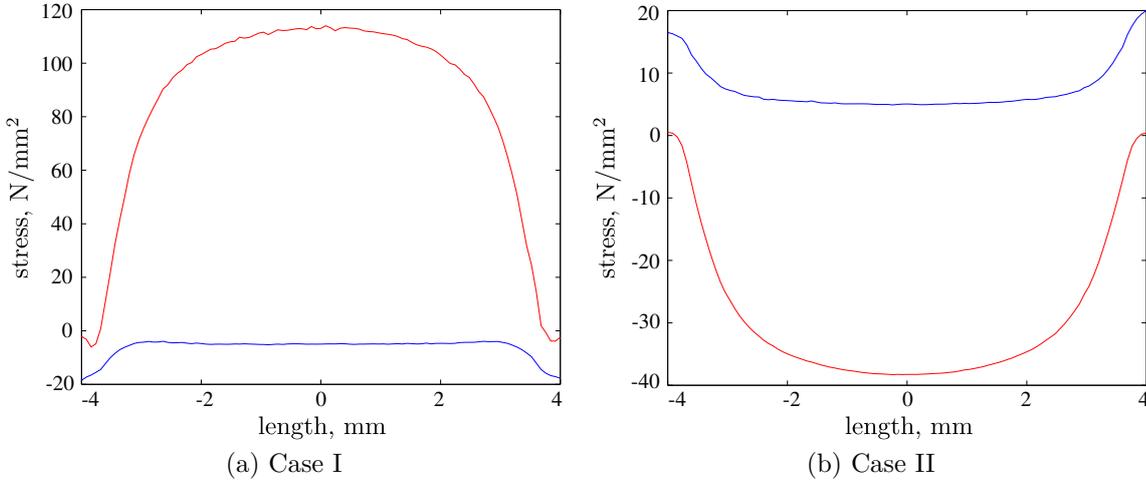


Figure 5.8: Stress distributions on the crystal's top along the SAW propagation direction:  $\sigma_Z$  (red) and  $\sigma_X$  (blue)

The relative phase shift between the incident and the reflected signal is calculated according to (4.7) and equals

$$\delta\psi_I = \left. \frac{\Delta\psi}{\psi} \right|_I = 7.7904 \cdot 10^{-4}, \quad \delta\psi_{II} = \left. \frac{\Delta\psi}{\psi} \right|_{II} = -2.6164 \cdot 10^{-4}.$$

Then we can find the ratio between the phase shifts in cases I and II:

$$\frac{\delta\psi_{II}}{\delta\psi_I} \approx -0.336.$$

According to fig. 5.6, the ratio between the slopes of the red and the cyan curves, which correspond to setups I and II, is approximately equal to  $-0.3$ . This shows that the results obtained from the measurements and the simulations are in a good agreement with one another considering the assumptions we have made during the modelling.

In this PhD thesis we have developed a numerical model to describe the propagating of waves in periodic piezoelectric structures with the aim of its application to simulations of SAW devices. The suggested model is based on FEM which, along with FEM/BEM and FEM/SDA, has been one of the most extensively used numerical techniques in SAW research area. FEM has been chosen for its robustness, reliability, and straightforward implementation scheme. Moreover, the ability of FEM to handle material and geometrical inhomogeneities has made it even more attractive when modelling of multi-layered structures and/or consideration of second-order effects – such as temperature and pre-stressing – are required. The device behaviour can be described using phenomenological models whose parameters are obtainable from FEM analysis by means of the harmonic admittance technique.

Our numerical scheme implies the use of two main assumptions. The first one is the conventional approach where a real SAW IDT is modelled by an IDT with an infinite periodic electrode grating. It has been used within the model in order to reduce its complexity considering instead of the whole structure its unit cell with periodic boundary conditions. The last have been incorporated by means of Nitsche's method, which, in contrast to the Lagrange multiplier approach, does not lead to a saddle point linear system. Therefore, it proves to be more convenient in terms of numerical stability. The second assumption is to consider the piezoelectric substrate to be infinite in depth, which is also common for numerical models of SAW devices. The open domain problem is then treated using the PML technique. Here, we have applied the PML formulation based on a complex frequency shifted metric. It has been extensively used by many authors in geophysics for surface waves modelling, and it proves to be appropriate in our case. We have discussed that such a PML increases the attenuation of the waves that radiate downward into the substrate and the waves that attenuate with the depth. It is thus possible to truncate the computational domain in case of both surface and leaky wave solutions.

We have validated the FE model comparing the simulation results with the results reported in the literature and those obtained from FEM/BEM simulations. Some examples of practical applications of the developed approach have been demonstrated and, again, compared with the experiments and the literature. It has also been demonstrated how to use the results of FE computations and HA technique to extract the parameters required for SAW phenomenological models.

In this PhD thesis we have restricted ourselves to the simulations in 2D space; investigating the second-order effects, we have assumed uniform distributions of temperature and mechanical stress and strain fields. However, this is not due to the limitations of the model. If needed, it can be used for 3D computations (i.e. the structures having a finite aperture) and/or non-uniform temperature or prestressing effects, provided that the pattern of periodicity is not violated. The case of non-periodic SAW structures can be considered as a future development of the model. Indeed, FEM remains attractive for simulations of complex structures, and CFS-PML can be used for the same purpose as within the scheme with periodic boundary conditions.

### Used Hilbert spaces

Consider a domain  $\Omega \subset \mathbb{R}^n$  with a piecewise smooth Lipschitz boundary  $\partial\Omega$ . Let  $\xi(\mathbf{x})$  be a complex valued function on  $\Omega$ , i.e.  $\xi: \Omega \rightarrow \mathbb{C}$ . The Lebesgue space  $L_2(\Omega)$  is defined as the space of squared Lebesgue integrable functions

$$L_2(\Omega) = \left\{ \xi: \int_{\Omega} |\xi|^2 d\Omega < \infty \right\}.$$

The inner product and the norm in  $L_2$  are defined as follows

$$\langle \xi, \eta \rangle_{L_2} = \int_{\Omega} \xi \bar{\eta} d\Omega, \quad \|\xi\| = \langle \xi, \xi \rangle_{L_2}^{1/2}. \quad (\text{A.1})$$

The space  $L_2$  is obviously a Hilbert space. It is built as a closure of continuous in  $\Omega$  functions with respect to the norm (A.1).

The Sobolev space  $H^p(\Omega)$  is defined as the space of functions which Sobolev derivatives up to  $p^{\text{th}}$ -order belong to  $L_2(\Omega)$ , i.e.  $H^p(\Omega) = \{ \xi \in L_2(\Omega) : D^\alpha \xi \in L_2(\Omega), 0 \leq \alpha \leq p \}$ . The space  $H^p(\Omega)$  is a Hilbert space. The inner product and the norm read

$$\langle \xi, \eta \rangle_{H^p} = \sum_{0 \leq \alpha \leq p} \int_{\Omega} \partial^\alpha \xi \partial^\alpha \bar{\eta} d\Omega, \quad \|\xi\| = \langle \xi, \xi \rangle_{H^p}^{1/2}. \quad (\text{A.2})$$

In case  $p = 1$  (A.2) turns to

$$\langle \xi, \eta \rangle_{H^1} = \int_{\Omega} (\nabla \xi \cdot \nabla \bar{\eta} + \xi \bar{\eta}) d\Omega, \quad \|\xi\| = \langle \xi, \xi \rangle_{H^1}^{1/2}. \quad (\text{A.3})$$

It is then obvious that the solution  $\mathbf{w}$  of the boundary value problem (3.13) belongs to the space  $H^1$ .

A trace operator  $\text{tr}: H^1(\Omega) \rightarrow L_2(\partial\Omega)$  defines a space  $H^{1/2}(\partial\Omega)$  as follows

$$H^{1/2}(\partial\Omega) = \left\{ \zeta \in L_2(\partial\Omega) : \exists \xi \in H^1(\Omega), \zeta = \text{tr}\xi \text{ on } \partial\Omega \right\}.$$

The space  $H^{-1/2}$  is dual of  $H^{1/2}$ , and the duality pairing reads

$$\forall \zeta \in H^{1/2}(\partial\Omega), \psi \in H^{-1/2}(\partial\Omega) : \langle \zeta, \psi \rangle_{H^{1/2} \times H^{-1/2}} = \int_{\partial\Omega} \zeta \bar{\psi} d\Gamma. \quad (\text{A.4})$$

It follows from (A.4) and the trace operator definition that the normal stress  $\mathbf{T}$  in (3.13) (and obviously the Lagrange multiplier in (3.63), (3.64)) is a function of  $H^{-1/2}$ .

---

## Bibliography

---

- [1] D. Morgan. *Surface acoustic wave filters with applications to electronic communications and signal processing*. Elsevier Ltd., 2nd edition, 2007. ISBN 978-0-1237-2537-0.
- [2] C. Campbell. *Surface acoustic wave devices and their signal processing applications*. Academic Press, Inc., San Diego, 1989. ISBN 0-12-157345-1.
- [3] A. V. Mamishev, K. Sundara-Rajan, F. Yang, Y. Du, and M. Zahn. Interdigital sensors and transducers. *Proc. of the IEEE*, 92(5):808–845, 2004.
- [4] L. Rayleigh. On waves propagated along the plane surface of an elastic solid. *Proc. London Math. Soc.*, s1-17:4–11, 1885.
- [5] P. Dineva, D. Gross, R. Müller, and T. Rangelov. *Dynamic fracture of piezoelectric materials: Solution of time-harmonic problems via BIEM*. Springer, 2014. ISBN 978-3-319-03961-9.
- [6] W. Voigt. *Lehrbuch der Kristallphysik*. Teubner, Berlin, 1910.
- [7] R. H. Tancrell and M. G. Holland. Acoustic surface wave filters. *Proc. IEEE*, 59:393–409, 1971.
- [8] D. P. Morgan. A history of surface acoustic wave devices. *Int. J. Hi. Spe. Ele. Syst.*, 10(3):553–601, 2000.
- [9] W. R. Smith, H. M. Gerard, J. H. Collins, T. M. Reeder, and H. J. Shaw. Analysis of interdigital surface wave transducers by use of an equivalent circuit model. *IEEE Trans.*, MTT-17:856–864, 1969.

- [10] Y. Suzuki, H. Shimizu, M. Takeuchi, K. Nakamura, and A. Yamada. Some studies of SAW resonators and multiple-mode filters. In *IEEE Ultrason. Symp.*, pages 279–302, 1976.
- [11] G. Tobolka. Mixed matrix representation of SAW transducers. *IEEE Trans. Sonics Ultrason.*, SU-26(6):426–428, 1979.
- [12] R. F. Milsom, N. H. C. Reilly, and M. Redwood. Analysis of generation and detection of surface and bulk acoustic waves by Interdigital transducers. *IEEE Trans. Sonics Ultrason.*, SU-24(3):147–166, 1977.
- [13] K. Hashimoto and M. Yamaguchi. Analysis of excitation and propagation of acoustic waves under periodic-metallic grating structure for SAW device modeling. In *IEEE Ultrason. Symp.*, pages 143–148, 1993.
- [14] K. Hasegawa and M. Koshiba. Finite element solution of Rayleigh-wave scattering from reflective gratings on piezoelectric substrate. *IEEE Trans. UFFC*, 37(2):99–105, 1990.
- [15] Z. H. Chen, M. Takeuchi, and K. Yamanouchi. Analysis of the film thickness dependence of a single-phase unidirectional transducer using the coupling-of-modes theory and the finite-element method. *IEEE Trans. UFFC*, 39(1):82–94, 1992.
- [16] H. P. Reichinger and A. R. Baghai-Wadji. Dynamic 2D analysis of SAW-devices including massloading. In *IEEE Ultrason. Symp.*, pages 7–10, 1992.
- [17] P. Ventura, J. Desbois, and L. Boyer. A mixed FEM/analytical model of the electrode mechanical perturbation for SAW and PSAW propagation. In *IEEE Ultrason. Symp.*, pages 205–208, 1993.
- [18] P. Ventura, J. M. Hode, and M. Solal. A new efficient combined FEM and periodic Green’s function formalism for the analysis of periodic SAW structures. In *IEEE Ultrason. Symp.*, volume 1, pages 263–268, 1995.
- [19] G. Endoh, K. Hashimoto, and M. Yamaguchi. Surface acoustic wave propagation characterisation by finite-element method and spectral domain analysis. *Jap. J. Appl. Phys.*, 34:2638–2641, 1995.
- [20] P. Bauerschmidt, R. Lerch, J. Machui, W. Ruile, and G. Visintini. Reflection and transmission coefficients of SAW in a periodic grating computed by finite element analysis. In *IEEE Ultrason. Symp.*, pages 421–423, 1990.
- [21] M. Buchner, W. Ruile, A. Dietz, and R. Dill. FEM analysis of the reflection coefficient of SAWs in an infinite periodic array. In *IEEE Ultrason. Symp.*, pages 371–375, 1991.

- 
- [22] A. W. Snyder. Coupled-mode theory for optical fibers. *J. Opt. Soc. Am.*, 62(11):1267–1277, 1972.
- [23] A. Yariv. Coupled-mode theory for guided-wave optics. *IEEE J. Quantum Electron.*, QE-9(9):919–933, 1973.
- [24] C. S. Hartmann, P. V. Wricjht, R. J. Kansy, and E. M. Garber. An analysis of SAW interdigitl transducer with internal reflections and the applications to the design of single-phase unidirectional transducers. In *IEEE Ultrason. Symp.*, pages 40–45, 1982.
- [25] V. Plessky and J. Koskela. *Advances in surface acoustic wave technology, systems and applications*, volume 2, chapter “Coupling-of-modes analysis of SAW devices”, pages 1–82. World Scientific Publ., 2001.
- [26] K.-Y. Hashimoto. *Surface acoustic wave devices in telecommunications*. Springer, Berlin, 2000. ISBN 978-3-662-04223-6.
- [27] D.-P. Chen and H. A. Haus. Analysis of metal-strip SAW gratings and transducers. *IEEE Trans. Sonics Ultrason.*, 32(3):395–408, 1985.
- [28] W. H. Bragg and W. L. Bragg. The reflection of X-rays by crystals. *Proc R. Soc. Lond.*, 88(605):428–438, 1913.
- [29] J. Koskela. *Modeling SAW devices including mass-loading effects*. PhD thesis, Helsinki University of Technology, 1998.
- [30] J. Koskela, V. P. Plessky, and M. M. Salomaa. SAW/LSAW COM parameter extraction from computer experiments with harmonic admittance of a periodic array of electrodes. *IEEE Trans. UFFC*, 46(4):806–816, 1999.
- [31] K. Bløtekjær, K. A. Ingebrigtsen, and H. Skeie. A method for analyzing waves in structures consisting of metal strips on dispersive media. *IEEE Trans. Electron Devices*, 20(8):1133–1138, 1973.
- [32] Y. Zhang, J. Desbois, and L. Boyer. Characteristic parameters of surface acoustic waves in a periodic metal grating on a piezoelectric substrate. *IEEE Trans. UFFC*, 40(3):183–192, 1993.
- [33] V. P. Plessky, S. V. Biryukov, and J. Koskela. Harmonic admittance and dispersion equations – the theorem. In *IEEE Ultrason. Symp.*, pages 159–162, 2000.
- [34] Ph. G. Ciarlet. *Mathematical elasticity: Three-dimensional elasticity*, volume 1. Elsevier Science Ltd, 1988. ISBN 0-444-70259-8.

- [35] M. Kaltenbacher. *Numerical simulation of mechatronic sensors and actuators*. Springer, Berlin, 3. edition, 2015. ISBN 978-3-642-40170-1.
- [36] Y. B. Fu and R. W. Ogden, editors. *Nonlinear elasticity: Theory and applications*. Cambridge University Press, Cambridge, 2001. ISBN 0-521-79695-4.
- [37] T. Belytschko, W. K. Lie, and B. Moran. *Nonlinear finite elements for continua and structures*. John Wiley & Sons Ltd, 2001. ISBN 0-471-98773-5.
- [38] B. A. Auld. *Acoustic fields and waves in solids*, volume 1. John Wiley & Sons Ltd, New York, 1973. ISBN 0-471-03700-1.
- [39] M. Conry. Notes on wave propagation in anisotropic elastic solids, 2002.
- [40] I. A. Viktorov. *Rayleigh and Lamb waves: Physical theory and applications*. Springer, New York, 2013. ISBN 978-1-4899-5683-5.
- [41] B. D. Zaitsev, I. E. Kuznetsova, S. G. Joshi, and A. S. Kuznetsova. New method of change in temperature coefficient delay of acoustic waves in thin piezoelectric plates. *IEEE Trans. UFFC*, 53(11):2113–2120, 2006.
- [42] A. Kahan. Elastic constants for quartz and their temperature coefficients. In *36th Annual Frequency Control Symposium*, pages 159–169, 1982.
- [43] K. K. Wong. *Properties of lithium niobate*. The Institution of Engineering and Technology, London, 2002. ISBN 978-0-852-96799-7.
- [44] P. M. Davulis and M. Pereira da Cunha. High-temperature langatate elastic constants and experimental validation up to 900 °C. *IEEE Trans. UFFC*, 57(1):59–65, 2010.
- [45] R. T. Smith and F. S. Welsh. Temperature dependence of the elastic, piezoelectric, and dielectric constants of lithium tantalate and lithium niobate. *J. Appl. Phys.*, 42(6):2219–2230, 1971.
- [46] J. Bonet and R. D. Wood. *Nonlinear continuum mechanics for finite element analysis*. Cambridge University Press, Cambridge, 2nd edition, 2008. ISBN 978-0-521-83870-2.
- [47] A. L. Nalamwar and M. Epstein. Surface acoustic waves in strained media. *J. Appl. Phys.*, 47(1):43–48, 1976.
- [48] P. C. Y. Lee and M. S. H. Tang. Thickness vibrations of doubly rotated crystal plates under initial deformations. *IEEE Trans. UFFC*, 34(6):659–666, 1987.
- [49] H. Liu, Z. B. Kuang, and Z. M. Cai. Propagation of Bluestein-Gulyaev waves in a prestressed layered piezoelectric structure. *Ultrasonics*, 41:397–405, 2003.

- 
- [50] H. Liu, Z. B. Kuang, and Z. M. Cai. Propagation of surface acoustic waves in prestressed anisotropic layered piezoelectric structures. *Acta Mech. Solida Sin.*, 16:16–23, 2003.
- [51] M. Lematre, G. Feuillard, Th. Delaunay, and M. Lethiecq. Modeling of ultrasonic wave propagation in integrated piezoelectric structures under residual stress. *IEEE Trans. UFFC*, 53(4):685–696, 2006.
- [52] M. Domenjoud, M. Lematre, L.-P. Tran-Huu-Hue, and G. Feuillard. Integrated piezoelectric structures under external mechanical stress: Theory and experiments. In *IEEE Ultrason. Symp.*, pages 2080–2082, 2010.
- [53] M. Domenjoud, M. Lematre, M. Gratton, M. Lethiecq, and L.-P. Tran-Huu-Hue. Theoretical and experimental study of the electroacoustic behavior of lithium niobate under an initial mechanical stress. *IEEE Trans. UFFC*, 60(10):2219–2224, 2013.
- [54] G. R. Barsch. Relation between third-order elastic constants of single crystals and polycrystals. *J. Appl. Phys.*, 39(8):3780–3793, 1968.
- [55] R. N. Thurston, H. J. McSkimin, and P. Anderatch, Jr. Third-order elastic coefficients of quartz. *J. Appl. Phys.*, 37(1):267–275, 1966.
- [56] Y. Nakagawa, K. Yamanouchi, and K. Shibayama. Third-order elastic constants of lithium niobate. *J. Appl. Phys.*, 44(9):3969–3974, 1973.
- [57] W. R. Smith. Circuit-model analysis and design of interdigital transducers for surface acoustic wave devices. In *Physical acoustic*, volume 15, chapter 2, pages 100–190. Academic Press, Inc., New York, 1981. ISBN 0-12-477915-8.
- [58] M. S. P. Eastham. *The spectral theory of periodic differential equations*. Scottish Academic Press, Edinburgh, 1973. ISBN 7011-1936-5.
- [59] P. A. Kouchment. Floquet theory for partial differential equations. *Russ. Math. Surv.*, 37(1):1–60, 1982.
- [60] Ph. J. Davis and Ph. Rabinowitz. *Methods of numerical integration*. Academic Press, San Diego, 1984. ISBN 1-48-323796-6.
- [61] T. Myint-U and L. Debnath. *Linear partial differential equations for scientists and engineers*. Birkhäuser, Boston, 4. edition, 2007. ISBN 0-8176-4393-1.
- [62] A. N. Tikhonov and A. A. Samarskii. *Equations of mathematical physics*. Dover publications, Inc., New York, 1990. ISBN 0-486-66422-8.

- [63] A. I. Borisenko and I. E. Tarapov. *Vector and tensor analysis with applications*. Dover publications, Inc., New York, 1979. ISBN 0-486-63833-2.
- [64] R. C. Peach. A general green function analysis for SAW devices. In *IEEE Ultrason. Symp.*, volume 1, pages 221–225, 1995.
- [65] L. E. Tsyrlin. *Selected problems of electric and magnetic fields computation [In Russian]*. Sov. Radio, Moscow, 1977.
- [66] J. Koskela, V. P. Plessky, and M. M. Salomaa. Suppression of the leaky SAW attenuation with heavy mechanical loading. *IEEE Trans. UFFC*, 45(2):439–449, 1998.
- [67] P. Ventura and J. Gratier. FEM/BEM analysis of infinite periodic grating covered with an SiO<sub>2</sub> overlay. In *IEEE Ultrason. Symp.*, pages 815–819, 2008.
- [68] W. Luo, Q. Y. Fu, J. L. Wang, H. Liu, and D. X. Zhou. Accurate FEM/BEM simulation of wireless passive surface acoustic wave sensors. *Key Engineering Materials*, 368–372:198–201, 2008.
- [69] P. M. Smith. Dyadic Green’s functions for multi-layer SAW substrates. *IEEE Trans. UFFC*, 48(1):171–179, 2001.
- [70] V. Laude, C. F. Jerez-Hanckes, and S. Ballandras. Surface Green’s function of a piezoelectric half-space. *IEEE Trans. UFFC*, 53(2):420–428, 2006.
- [71] P. Ventura, F. Hecht, and P. Dufilie. Single electrode periodic buried IDT analysis using an original FEM/BEM numerical model. In *IEEE Ultrason. Symp.*, pages 645–649, 2010.
- [72] P. Dufilie, P. Ventura, and F. Hecht. COM parameters for thick metal and partially buried electrodes extracted from a mixed FEM/BEM numerical model. In *IEEE Ultrason. Symp.*, pages 807–810, 2012.
- [73] K. Hashimoto, G. Q. Zheng, and M. Yamaguchi. Fast analysis of SAW propagation under multi-electrode-type gratings with finite thickness. In *IEEE Ultrason. Symp.*, pages 279–284, 1997.
- [74] K. Hashimoto, T. Omori, and M. Yamaguchi. Characterization of surface acoustic wave propagation in multi-layered structures using extended FEM/SDA software. *IEEE Trans. UFFC*, 56(11):2559–2564, 2009.
- [75] N. F. Naumenko. A universal technique for analysis of acoustic waves in periodic grating sandwiched between multi-layered structures and its application to different types of waves. In *IEEE Ultrason. Symp.*, pages 1673–1676, 2010.

- 
- [76] N. F. Naumenko. Advanced numerical technique for analysis of surface and bulk acoustic waves in resonators using periodic metal gratings. *J. Appl. Phys.*, 116:104503–1–10, 2014.
- [77] M. J. Grote and J. B. Keller. Exact nonreflecting boundary condition for elastic waves. *SIAM J. Appl. Math.*, 60(3):803–819, 1977.
- [78] B. Engquist and A. Majda. Absorbing boundary conditions for the numerical simulation of waves. *Mathematics of Computation*, 31(139):629–651, 1977.
- [79] M. Hofer. *Finite Elemente Berechnung von periodischen Oberflächenwellen Strukturen*. PhD thesis, Universität Erlangen-Nürnberg, 2003.
- [80] J. P. Berenger. A perfectly matched layer for the absorption of electromagnetic waves. *J. Comp. Phys.*, 114:185–200, 1994.
- [81] Z. S. Sacks, D. M. Kingsland, R. Lee, and J. F. Lee. A perfectly matched anisotropic absorber for use as an absorbing boundary condition. *IEEE Trans. Antennas and Propagation*, 43(12):1460–1463, 1995.
- [82] W. C. Chew and W. H. Weedon. A 3d perfectly matched medium from modified Maxwell’s equations with stretched coordinates. *Microwave Optical Tech. Letters*, 7(13):599–604, 1994.
- [83] W. C. Chew and Q. H. Liu. Perfectly matched layers for elastodynamics: A new absorbing boundary condition. *J. Comp. Acoust.*, 4(4):341–359, 1996.
- [84] F. D. Hastings, J. B. Schneider, and S. L. Broschat. Application of the perfectly matched layer (PML) absorbing boundary condition to elastic wave propagation. *J. Acoust. Soc. Amer.*, 100(5):3061–3069, 1996.
- [85] Y. F. Li and O. Bou Matar. Convolutional perfectly matched layer for elastic second-order wave equation. *J. Acoust. Soc. Amer.*, 127(3):1318–1326, 2010.
- [86] R. Shi, S. Wang, and J. Zhao. An unsplit complex-frequency-shifted PML based on matched Z-transform for FDTD modelling of seismic wave equations. *J. Geophys. Eng.*, 9(2):218–229, 2012.
- [87] R. Matzen. An efficient finite element time-domain formulation for the elastic second-order wave equation: A non-split complex frequency shifted convolutional PML. *Int. J. Numer. Meth. Engng.*, 88(10):951–973, 2011.
- [88] F. H. Drossaert and A. Giannopoulos. A nonsplit complex frequency-shifted PML based on recursive integration for FDTD modeling of elastic waves. *Geophysics*, 72(2):T9–T17, 2007.

- [89] M. Kuzuoglu and R. Mittra. Frequency dependence of the constitutive parameters of causal perfectly matched anisotropic absorbers. *IEEE Microwave Guided Wave Lett.*, 6(12):447–449, 1996.
- [90] D. Komatitsch and R. Martin. An unsplit convolutional perfectly matched layer improved at grazing incidence for the seismic wave equation. *Geophysics*, 72(5):SM155–SM167, 2007.
- [91] K. Shaposhnikov, M. Kaltenbacher, and P. Nicolay. Fast full-FEM computation of COM parameters. Application to multilayered SAW structures. In *IEEE Ultrason. Symp.*, pages 1501–1504, 2014.
- [92] R. Martin and D. Komatitsch. An unsplit convolutional perfectly matched layer technique improved at grazing incidence for the viscoelastic wave equation. *Geophys. J. Int.*, 179:333–344, 2009.
- [93] W. Zhang and Y. Shen. Unsplit complex frequency-shifted PML implementation using auxiliary differential for seismic wave modelling. *Geophysics*, 75(4):T141–T154, 2010.
- [94] S. G. Johnson. Notes on perfectly matched layers. Online MIT course notes, 2010.
- [95] J. A. Roden and S. D. Gedney. Convolution PML (CPML): An efficient FDTD implementation of the CFS-PML for arbitrary media. *Microwave Opt. Technol. Lett.*, 27(5):334–339, 2000.
- [96] I. Laakso, S. Ilvonen, and T. Uusitupa. Performance of convolutional PML absorbing boundary conditions in finite-difference time-domain SAR calculations. *Phys. Med. Biol.*, 52:7183–7192, 2007.
- [97] R. Martin, D. Komatitsch, and S. D. Gedney. A variational formulation of a stabilized unsplit convolutional perfectly matched layer for the isotropic or anisotropic seismic wave equation. *Comput. Model. Eng. Sci.*, 37(3):274–304, 2008.
- [98] E. Bécache, S. Fauqueux, and P. Joly. Stability of perfectly matched layers, group velocities and anisotropic waves. *J. Comp. Phys.*, 188:399–433, 2003.
- [99] K. C. Meza-Fajardo and A. S. Papageorgiou. A nonconvolutional, split-field, perfectly matched layer for wave propagation in isotropic and anisotropic elastic media: Stability analysis. *Bull. Seism. Soc. Am.*, 98(4):1811–1836, 2008.
- [100] A. Fathi, B. Poursartip, and L. F. Kallivokas. Time-domain hybrid formulations for wave simulations in three-dimensional PML-truncated heterogeneous media. *Int. J. Numer. Meth. Engng.*, 101:165–198, 2015.

- 
- [101] J. Blazek. *Computational fluid dynamics: Principles and applications*. Elsevier Science, Oxford, 2nd edition, 2005. ISBN 978-0-08-044506-9.
- [102] M. Hofer, N. Finger, G. Kovacs, J. Schöberl, S. Zaglmayr, U. Langer, and R. Lerch. Finite element simulation of wave propagation in periodic piezoelectric SAW structures. *IEEE Trans. UFFC*, 53(6):1192–1201, 2006.
- [103] M. Aubertin, T. Hennerson, F. Piriou, P. Guerin, and J.-C. Mipo. Periodic and anti-periodic boundary conditions with the lagrange multipliers in FEM. *IEEE Trans. Magn.*, 40(8):3417–3420, 2010.
- [104] O. Schenk, K. Gärtner, W. Fichtner, and A. Stricke. PARDISO: A high-performance serial and parallel sparse linear solver in semiconductor device simulation. *Future Generation Computer Systems*, 18(1):69–78, 2001.
- [105] B. I. Wohlmuth. A mortar finite element method using dual spaces for the lagrange multiplier. *SIAM J. Numer. Anal.: Math. Model. Numer. Anal.*, 38:989–1012, 2000.
- [106] A. Hansbo, P. Hansbo, and M. G. Larson. A finite element method on composite grids based on Nitsche’s method. *ESAIM: Math. Model. Numer. Anal.*, 37:495–514, 2003.
- [107] J. Nitsche. Über ein Variationsprinzip zur Lösung von Dirichlet-Problemen bei Verwendung von Teilräumen, die keinen Randbedingungen unterworfen sind. *Abh. Math. Sem. Univ. Hamburg*, 36(1):9–15, 1971.
- [108] M. Kaltenbacher. Advanced simulation tool for the design of sensors and actuators. In *Procedia Engineering, Eurosensors XXIV*, volume 5, pages 597–600, Linz, Austria, 2010.
- [109] C. A. Tracy. Lectures on differential equations. University of California, 2015.
- [110] G. Kovacs, M. Anhorn, H. E. Engan, G. Visintini, and C. C. W. Ruppel. Improved material constants for  $\text{LiNbO}_3$  and  $\text{LiTaO}_3$ . In *IEEE Ultrason. Symp.*, pages 435–438, 1990.
- [111] A. Ștefănescu, D. Neculoiu, A. Müller, A. Dinescu, G. Konstantinidis, and A. Stavriniadis. Analysis of GaN based SAW resonators including FEM modeling. *Rom. J. Inf. Sci. Tech.*, 14(4):334–345, 2011.
- [112] D. E. Cullen and T. M. Reeder. Measurement of SAW velocity versus strain for YX and ST quartz. In *IEEE Ultrason. Symp.*, pages 519–522, 1975.
- [113] H. Takeuchi and H. Yamauchi. Strain effects on surface acoustic wave velocities in modified  $\text{PbTiO}_3$  ceramics. *J. Appl. Phys.*, 52(10):6147–6150, 1981.

- [114] W. Wilson and G. Atkinson. Characterisation of langasite SAW devices to determine the temperature and strain coefficients of velocity. *Sensors & Transducers*, 162(1):21–28, 2014.
- [115] B. Maier. *Design of a test procedure and characterization of the correlation between strain and SAW propagation time in single crystals*. Master thesis, FH-Kärnten, 2011.

# Curriculum Vitae

## Personal Data

Name: Kirill Shaposhnikov  
Date of Birth: September 15, 1984  
Place of Birth: Kamenolomni, USSR

## Education

09/1991 – 06/2001 School no. 6, Shakhty, Russia  
08/2001 – 07/2006 South-Russian State Technical University, Dep. of Appl. Math., Novochoerkassk, Russia  
Specialist diploma (mathematician engineer)  
10/2006 – 08/2010 South-Russian State Technical University, Dep. of Appl. Math., Novochoerkassk, Russia  
Candidate of Sciences (mathematical modelling, numerical mathematics and scientific computing)

## Professional Experiences

09/2006 – 12/2011 University assistant at Dep. of Appl. Math., South-Russian State Technical University, Novochoerkassk, Russia  
10/2006 – 12/2011 Junior research assistant at Lab of Electr. and Power Eng., Southern Scientific Centre of Russian Academy of Sciences, Novochoerkassk, Russia  
01/2012 – 03/2012 Project assistant at Dep. of Smart Systems Technologies, University of Klagenfurt, Klagenfurt, Austria  
04/2012 – 09/2015 Project assistant/PhD. student at Dep. of Measurement and Actuator, TU Wien, Vienna, Austria

December 15, 2015